The Thesis Committee for Sean Bryan O'Donnell
Certifies that this is the approved version of the following Thesis:

Interactions between Pyroclastic Density Currents: Insights from Analog Experiments

APPROVED BY

SUPERVISING COMMITTEE:

James E. Gardner, Supervisor

David Mohrig

James Buttles

Benjamin Andrews

Interactions between Pyroclastic Density Currents: Insights from Analog Experiments

by

Sean Bryan O'Donnell

THESIS

Presented to the Faculty of the Graduate School of

The University of Texas at Austin

in Partial Fulfillment

of the Requirements

for the Degree of

MASTER OF SCIENCE IN GEOLOGICAL SCIENCES

THE UNIVERSITY OF TEXAS AT AUSTIN

AUGUST 2018

To my family and friends

Acknowledgements

The author wishes to express sincere thanks to Dr. James Gardner for his support, guidance, and supervision in the preparation of this thesis over the past two years at UT, and also acknowledge Drs. David Mohrig, James Buttles, and Benjamin Andrews for being part of my thesis committee, and allowing me to use their laboratories and tanks to run experiments. I would like to give special thanks to Dr. James Buttles for being willing to spend countless hours going over data with me and thinking through multiple hypothesis on how to explain it. I would also like to thank Elizabeth Davis, an undergraduate student, for her help and support, as well as letting me help her on her honors project. And finally, I would like to thank my family and friends, whose support I greatly appreciate and encouraged me as I prepared this thesis.

Sean Bryan O'Donnell

The University of Texas at Austin

August 2018

Interactions between Pyroclastic Density Currents: Insights from Analog Experiments

Sean Bryan O'Donnell, M.S.GEO.SCI.

The University of Texas at Austin, 2018

Supervisor: James E. Gardner

During some explosive volcanic eruptions, multiple pyroclastic density currents have been produced within a short time span of each other and flowed through the same area. This creates the potential for the currents to interact, specifically in a way where a leading current is produced, and then a similar trailing current is produced a short time later and possibly flows into the leading current. The leading current, having changed the ambient surroundings from normal air, may then have an effect on the dynamics and behavior of the trailing current. To examine this effect, we designed scaled experiments to produce an analogue leading current and a trailing current that flows into it. The experiments took place in both an air medium and a water medium. The results of the experiments showed that the behavior of the trailing current may change as a result of interacting with the leading current. After certain intervals of time between currents, the trailing current had a longer final runout distance compared to the leading current it flowed through. This is caused by the presence of a plume created by the leading current when it reverses buoyancy. At intermediate heights above the bed, after moderate amounts of time between currents, the leading plume is less dense than the newly created trailing plume, and the trailing current cannot rise, and the momentum stays in the body of the trailing current. This accelerates the trailing current, which decreases sedimentation rate, and allows the current to runout to a greater distance before lifting off. At low heights and great heights above

the bed, the leading plume is denser than the trailing plume, and the trailing plume can then rise without impediment. In natural pyroclastic density currents, the magnitude by which the leading current affects the trailing current depends on the rise time of the leading plume.

Table of Contents

List of Tables

List of Figures

Introduction

Pyroclastic density currents (PDCs) are mixtures of volcano-produced particles and hot gas (Branney and Kokelaar, 2002; Druitt, 1998). They are hot, dense, fast moving currents, and are the most dangerous phenomenon of an explosive volcanic eruption (Baxter et al., 2017, 2005; Benage et al., 2016; Druitt, 1998). Three different causes of PDCs exist: eruption column collapse during a Plinian eruption, partial lava dome collapse, and lateral blast (Behncke et al., 2003; Branney and Kokelaar, 2002; Gorshkov, 1959; Gorshkov and Dubik, 1970; Hoblitt, 2000; Lipman and Mullineaux, 1980; Woods and Wohletz, 1991). PDCs are composed of two parts: a dense, ground-hugging undercurrent, and a dilute, upper surge, which sometimes may decouple into separate currents (Bourdier and Abdurachman, 2001; Burgisser and Bergantz, 2002; Druitt, 1998; Saucedo et al., 2002). PDCs typically have a finite runout distance from the volcano, at which point they become buoyant and lift-off, creating a co-ignimbrite column (also known as a phoenix cloud) that rises into the atmosphere, sometimes dozens of kilometers (Andrews and Manga, 2012, 2011; Branney and Kokelaar, 2002; Bursik and Woods, 1996; Hoblitt, 2000; Sparks et al., 1993; Sparks and Walker, 1977; Woods and Bursik, 1994; Woods and Wohletz, 1991). They become buoyant through sedimentation and air entrainment. As the current progresses, it deposits its particle load, decreasing its mass. At the same time, turbulent eddies on the outer margins of the current entrain cold, ambient air, which heats and expands, increasing volume of the current. The combination of sedimentation and entrainment eventually leads to the current becoming buoyant and lifting off, reaching a finite runout distance (Andrews, 2014; Calder et al., 1997; Sher and Woods, 2017; Sparks et al., 1993; Woods and Bursik, 1994).

During certain volcanic eruptions, evidence suggests that some PDCs erupt closely in time and space, such that there exists the possibility for one PDC to flow into another and interact with it (Table 1). During these eruptions, currents are generated within minutes of each other and flow along the same topography, such as the same valley, ghaut, or stream channel. For example, a leading current may flow down a valley, and a trailing current generated a few minutes later flows down the same valley, catching up to the leading current and flows into it. Most of these types of currents are relatively small, generated from dome-collapse or column-collapse events, and, with the possible exception of the lateral-blast generated PDCs of the May 18, 1980 eruption of Mt. St. Helens, have runout distances of less than 15 km. In such cases, the leading current propagates through the ambient atmosphere, but the trailing current propagates through a medium modified by the leading current, or through leading current itself. The effect the leading current has on the trailing current is not well understood. The change of the ambient conditions caused by the leading current could impact the trailing current and make its less predictable. It is the goal of this study to investigate experimentally the interaction between pyroclastic density currents.

Laboratory experiments are useful tools to examine the behavior PDCs, because trying to examine PDCs in nature is generally too dangerous. Experiments have been used to examine characteristics of PDCs, such as current initiation (Dellino et al., 2010; Dellino et al., 2014), sedimentation (Andrews and Manga, 2012; Choux et al., 2004; Choux and Druitt, 2002), entrainment (Andrews, 2014; Hallworth et al., 1993), velocity and flow structure (Breard et al., 2016; Breard and Lube, 2017; Nield and Woods, 2004), deposits (Dellino et al., 2010), and the effects of topography (Andrews and Manga, 2011; Woods et al., 1998). Experimental PDCs provide a valuable means for studying how two separate currents interact. The conditions are

controlled and monitored, and the experiments can be correctly scaled to match the dynamics of natural PDCs (Sulpizio et al., 2014). In previous experiments, currents have not flowed into modified ambient conditions, and behavior was not affected in any way.

Experimental Background

We performed experiments by creating pairs of analog density currents, first generating a leading current and then generating a trailing current which flowed behind the leading current. The experimental currents differed from previous studies in that they began as normal ground-hugging density currents, but at some distance from the start of the runout they reverse buoyancy and lift-off into a rising plume. The leading current in each experiment flowed into "normal" ambient fluid, and consequently changed the characteristics of the ambient fluid, such as temperature, density, and particle concentration. The trailing current then flowed into the modified ambient fluid.

Experiments were carried out in two different settings: in an open air tank and a pool of water. These two settings were chosen to analyze different aspects of the currents. The runout distance of PDCs is a function of current mass flux, density, pyroclast granulometry, temperature, topography, air entrainment and sedimentation (Branney and Kokelaar, 2002). In currents, mass flux is defined is mass per unit time per cross sectional area. To limit the number of variables in our experiments, particle granulometry and componentry was held constant, and currents traversed smooth topography. The factors contributing to lift-off then are sedimentation, entrainment, and the temperature difference between the current and the ambient fluid. The behavior of the analog PDCs, which are a type of gravity current similar to underwater turbidity currents and snow avalanches, is characterized in the same terms as those other currents (Hákonardóttir et al., 2003; Sparks et al., 1993). Different aspects of the currents

can be described through dimensionless numbers common to fluid mechanics. These are the Reynolds (Re), Froude (Fr), bulk Richardson (Ri_B), and Rouse (Pn) numbers. Re is the ratio of momentum forces to viscous forces in the current, and is used to determine whether the current is in a laminar or turbulent flow regime. Re is defined as:

$$Re = \frac{\rho_c u h}{\mu}$$

where ρ_c is the current density, u is the current velocity, h is the current height, and μ is the dynamic viscosity of the current. Turbulent flow sets in at Re ≈ 1000, where inertial effects begins to dominate over viscous effects (Kleiser and Zang, 1991). When the current is turbulent, eddies form along the edges of the currents, creating the necessary conditions for entrainment to occur. Ri_B determines the scale of entrainment of ambient fluid into the current. Ri_B is the ratio of buoyancy to the flow shear of the current. At lower Ri_B , the entrainment in the current is large, while at higher Ri_B numbers, $Ri_B = 0.3$ (Geyer and Smith, 1987) or $Ri_B = 1$ (Bursik and Woods, 1996), turbulence decreases and the current transitions from a supercritical flow with major entrainment to a subcritical flow with little to no entrainment. Ri_B is defined as:

$$Ri_B = \frac{gh(\rho_c - \rho_a)}{\rho_c u^2}$$

where ρ_a is the density of the ambient fluid and g is the acceleration due to gravity. Entrainment in a density current is function of the Ri_B number (Ellison and Turner, 1959; Parker et al., 1987; Turner, 1986) according to the equation:

$$E = \frac{0.00153}{0.0204 + Ri_B}$$

4

Entrainment is typically given as a coefficient applied to a currents characteristic velocity. Entrainment decreases as Ri_B becomes larger, which occurs when the current velocity decreases. When the Ri_B becomes large enough, entrainment becomes negligible, and sedimentation then becomes the major control on runout distance. Currents with negligible entrainment runout much farther than currents that do entrain ambient fluid, requiring more time to reverse buoyancy assuming all else is equal (Bursik and Woods, 1996). Fr is the ratio of inertia to the body forces of the current. Fr determines whether a disturbance at the head of the flow can travel upstream into the current body. At high $Fr > 1$, disturbances cannot travel upstream or even stand steady in the current. At $Fr < 1$, disturbances are able to travel upstream and affect the dynamics of the current body (Smith, 2015). Fr is defined as:

$$Fr = \frac{u}{\sqrt{gh}}$$

Pn is the ratio of fall velocity of the particles to the shear velocity of the current (Rouse, 1937; Valentine, 1987; Zagarola and Smith, 1998). Pn defines the sediment profile of the current. where the sediment concentration at the top of the current is 0 and the concentration at the bed of the current is 1 (Rouse, 1937). The value of Pn determines the particle concentration and suspended sediment profile at different heights above the bed. Pn is defined as:

$$Pn = \frac{w}{\kappa u^*}$$

where w is the fall velocity of the particles in the current, κ is the von Karman constant ($\kappa \approx 0.407$), and u^* is the shear velocity of the current. The buoyancy of PDCs is measured by the buoyancy constant γ, defined as

$$\gamma = \frac{\rho_a - \rho_i}{C(\rho_s - \rho_i)}$$

where ρ_i is the density of the interstitial fluid, ρ_s is the density of the suspended particles, and C is the volume concentration of particles in the current. γ is only applicable to particle-laden currents. A current with a value γ<1 is capable of becoming buoyant and lifting off (Hogg et al., 2000, 1999).

Sedimentation of particles from the current can be modeled using Hazen's sedimentation law (Bonnecaze et al., 1995, 1993; Bursik and Woods, 1996; Hazen, 1904; Woods and Bursik, 1994). Hazen's law predicts that sedimentation is dependent on current mass flux, current height and velocity, and particle settling rate. The sedimentation rate also changes with runout distance, because mass flux decreases due to sedimentation and the current decelerates (Sparks et al., 1993). Rapid decreases in velocity are known to cause a large amount of sedimentation and nearly immediate buoyancy reversal (Macias et al., 1998; Saucedo et al., 2004).

PDCs become buoyant and generate rising plumes through multiple mechanisms; all of these mechanisms require buoyancy reversal of at least some component of the current. One mechanism is fluidization of the current (Sparks et al., 1997). Currents may become partially fluidized through entrainment of ambient air and through continued exsolution of magmatic volatiles in the current (Sparks, 1978, 1976; Wilson, 1984). This may cause smaller particles in the current to be elutriated and rise up out of the current to form a plume (Walker, 1980; Wilson, 1984). Another mechanism is boundary shear mixing at the top of the current, where a shear layer forms at the upper boundary of the current and entrains hot particles and gas from the current (Denlinger, 1987). Non-linear mixing in the upper, more dilute part of the current may also create a rising plume, along with creating a more dense lower part of the surge (Fisher, 1979; Huppert et al., 1986; Woods and Bursik, 1994). The final way rising plumes are created

from PDCs is through buoyant lift-off, in which the entire current reverses buoyancy and lifts-off into a large, co-ignimbrite plume (Sparks, 1986; Sparks et al., 1993; Woods and Wohletz, 1991).

The behavior of co-ignimbrite plumes changes with height of the plume (Woods and Wohletz, 1991). The density of the plume decreases drastically over the first few kilometers above the ground, and then at greater heights, the density increases back toward the ambient air density due to entrainment of denser air and cooling of the plume. When the current stops flowing and lifts off, the plume rise velocity increases from an initial value of zero to a maximum at a moderate height, before decreasing at even greater heights. The radius of the plume starts out large but rapidly shrinks over a very short change in height, after which the plume begins to increase in radius through entrainment of ambient air (Woods and Wohletz, 1991). This behavior has also been observed in nature and in experimental plumes (Calder et al., 1997; Sparks et al., 1993; Woods and Kienle, 1994).

Volcano	Date of Eruption(s)	Time Between Currents	Type of Data	Reference(s)
Vesuvius, Italy	472	Entrapment of fine ash particles by closely spaced PDCs	Deposit	(Sulpizio et al., 2007)
Ngauruhoe, New Zealand	February 19, 1975	Multiple PDCs in a 45 minute period	Visual	(Nairn and Self, 1978)
Mount St. Helens, USA	May 18, 1980	Two PDCs generated by lateral blast	Visual	(Hoblitt, 2000)
Tungurahua, Ecuador	August 16-17, 2006	16 events spaced 8 to at most 20 minutes apart	Seismic	(Hall et al., 2013)
Merapi, Indonesia	November 22, 1994 October 26 – November 5, 2010	Multiple PDCs separated by seconds to minutes Multiple PDCs separated minutes apart	Seismic, Visual	(Iguchi et al., 2011; Jenkins et al., 2013; Kelfoun et al., 2000; Komorowski et al., 2013)
Soufrière Hills, Montserrat	June 25, 1997	3 flow pulses within a 10 minute period	Seismic, Visual	(S C Loughlin et al., 2002; S.C. Loughlin et al., 2002)
Etna, Italy	October 25, 1999 June 8, 2000	Nearly continual lava dome collapse in a 40 minute period Multiple PDCs generated from column collapse in a 6 minute period	Visual	(Behncke, 2009; Behncke et al., 2003)
Colima, Mexico	July 10, 2015	3 flow pulses in a 9 minute period 6 flow pulses in a 52 minute period	Seismic, Visual	(Capra et al., 2018; Zobin, 2018)

Table 1. Summary of volcanic eruptions where closely spaced PDCs may have interacted.

Methods

Experiments in Air

All experiments performed in air followed the methods of Andrews (2014). Talc powder (d_{50} = 20 μm, ρ = 2.5 g/cm^3) was used for particles, and was heated in an oven to either 121° C or 93° C for 45 minutes to 1 hour, or kept at ambient temperature. Each experiment consisted of 1000g of talc powder, split evenly into 500 g to form the leading and trailing currents. The talc powder was spread to an even thickness over a conveyor belt that moved at a constant velocity of 1 cm/s. The talc powder was dropped down a chute at the end of the belt into an 8 m × 6 m × 2.6 m open-air tank, creating a 10-30 cm thick density current that flowed away from the chute at 8-25 cm/s (Fig. 1).

Two sheets of powder were separated on the conveyor belt by a distance corresponding to the time gap between currents. When a heated current entered the tank, it began to flow away from the chute and spread laterally over a narrow area of the floor of the tank (Fig. 2). It also began to entrain and heat up ambient air in the head and the top of the current through Kelvin-Helmholtz billows, and its thickness began to increase. As the current moved, it deposited particles on the floor of the tank. All heated currents eventually reversed buoyancy at some distance from the chute, and lifted off into a plume that rose to ceiling of the tank and spread laterally. Trailing currents entered the tank and behaved in the same manner.

Ambient temperature currents did not heat any entrained air, did not reverse buoyancy to form a rising plume, and instead flowed to the far wall of the tank. The currents also spread laterally along the bed, eventually flowing over the majority of the surface area of the floor of the tank.

9

Experimental currents were illuminated with three planes of red (650 nm), blue (445 nm), and green (532 nm) light, each generated by a series of 250-mW lasers. The red and blue planes were oriented parallel with the tank floor and illuminated heights above of the floor 5 cm and 25 cm respectively. The green plane was oriented perpendicular to the floor and parallel to the current flow direction. The experiment was recorded by two different digital single-lens reflex (DLSR) video cameras at 30 Hz with complementary metal–oxide–semiconductor (CMOS) sensors, having photoreceptors grouped in 2×2 squares of 1 red, 1 blue, and 2 green sensors. The photoreceptors have peak sensitivities at wavelengths equal to those of the light sheets, allowing the cameras to record the current highlighted by all three light sheets simultaneously. One camera was positioned high up on the left side of the tank, recording the downstream cross-section of the current. The other camera was position up and to the left of the conveyor belt and chute, recording the current from behind and capturing the horizontal imaging planes.

Videos of each experiment were then segmented into individual frames. Density of the currents was estimated from the intensity of light reflectance, assuming that a greater intensity of color equals greater particle concentration (Andrews, 2014; Andrews and Manga, 2012). The reflectance of the red light sheet was used a proxy for density for the current, and reflectance of the green light sheet was used as a proxy for density of the plume. The CMOS sensors record intensity of color as a value between 0 and 1. After the leading current had been flowing for 20 seconds, the all the red pixel values were summed, and after subtracting out the background value, the overall intensity of red light reflectance in the current was determined. This process was repeated for the trailing current.

Twenty-nine thermocouples were used to record the temperature of the currents (Fig. 3). One thermocouple was hung at the bottom of the chute to record the initial temperature of the

current. Five others were hung from the ceiling at heights of 65, 100, and 150 cm above the floor on the centerline 150 cm and 250 cm downstream from the chute to record the temperature of the plume. The rest of the thermocouples were positioned along the floor of three rows, at heights of 5 cm and 30 cm. A line of thermocouples was positioned in line with the chute, and two other lines were positioned 50 cm to the right and left. The rows of thermocouples were positioned beginning at 1 m downstream from the chute, and then every 50 cm from there out to 350 cm from the chute. The thermocouples recorded temperature at a rate of 3 Hz, with a precision of a ± 0.01 °C.

Experiments in Water

Experiments performed in a water medium, used plastic pellets ($d_{50} = 186$ μm, $\rho = 1.15$ g/cm^3) as the particles for the current (Fig. 4), following the methods of Steel et. al (2017). A schematic of the experimental setup is in Fig. 5-6. A pool 8 m × 6 m × 2 m was filled with ambient temperature (≈ 22 °C) water, and a head tank was filled with heated water (≈ 28 °C) plus plastic particles to 1.5 vol%. The warm particle-slurry in the head tank was continuously mixed with an auger throughout the experiment. A valve was opened at the bottom of the head tank, and the warm water-plastic slurry was released into the pool creating a density current flowing downhill over a platform with a 5° slope. The resulting leading current was allowed to flow continuously for two minutes, at which point the valve on the head tank was closed. The requisite amount of time passed (10, 20, 30, 40, or 60 seconds), and then the valve on the head tank was opened again, releasing a trailing current. This current also flow for two minutes, and then the valve on the head tank was once again closed.

Video of each experiment was recorded (underwater) with a GoPro® Hero camera at 60 Hz. Some experiments were also recorded with digital cameras high above the water, at a rate of

1 Hz. A Vectrino® Acoustic Doppler Velocimeter (ADV) was used to record the velocity of the current, and was placed 12 cm downstream from where the current entered the pool and 7 cm above the floor. Velocity was recorded in three different directions: downstream (X), cross stream (Y), and vertically (Z). Eight thermistors were used to record temperature at a rate of 60 Hz. Four were placed 6 cm above the floor at distances of 31, 56, 83, and 107 cm from the pipe. The other four were positioned vertically 74 cm from the pipe at heights of 26, 51, 78, and 105 cm above the floor (Fig. 5-6). The underwater video camera, the ADV, and the thermistors were continuously active and recording data through the duration of the experiment.

Eight siphons were used to collect particles from the currents in every experiment. Four siphons were used for the leading current and four siphons were used for the trailing current, which collected the particles and water in plastic bottles outside of the pool. Three sets of two siphons were positioned 6 cm above the bed, at distances of 20, 55, and 75 cm downstream. A fourth set was position vertically at 75 cm downstream and 17 cm above the bed. After either the leading or trailing current had been flowing for 45 seconds, the set of four siphons was opened to collect particles and water, and then closed after 30 seconds. Mass concentration of particles was determined by separating the particles from the water using a vacuum filter funnel and an Erlenmeyer flask. Masses of particles were them summed, and mass concentration of particles was calculated.

In three separate experiments, after the two currents stopped flowing, a laser was used to map the topography of the resulting deposit. The laser scanned along the Y direction of the deposit, moving downstream 1 mm increments. A deposit thickness map was generated by differencing the scans. At the end, the water was drained from the pool and photographs were taken of the deposit from multiple angles.
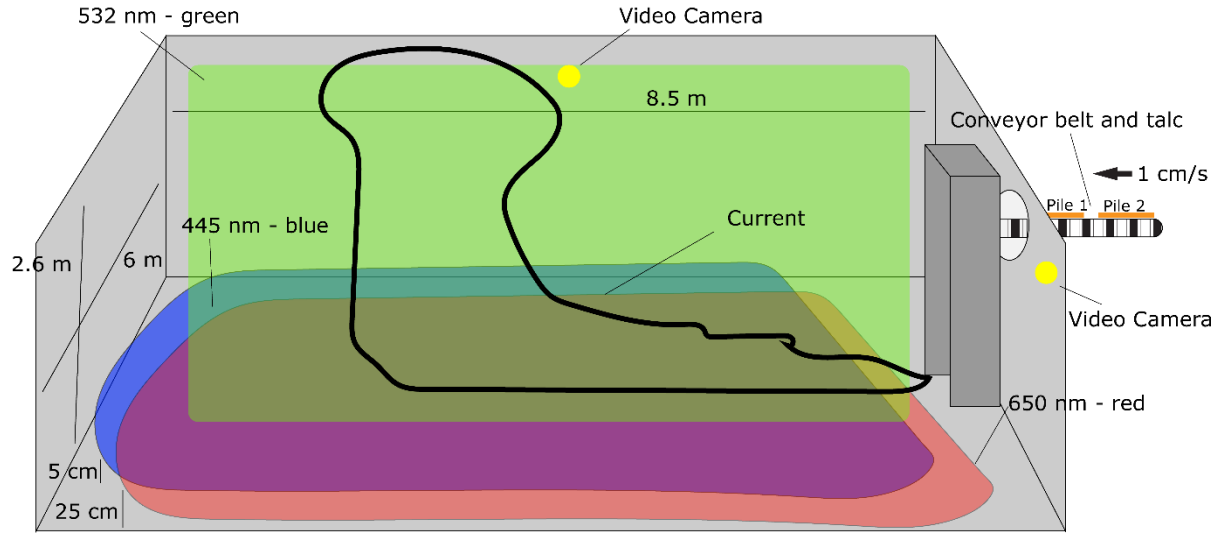
Fig. 1
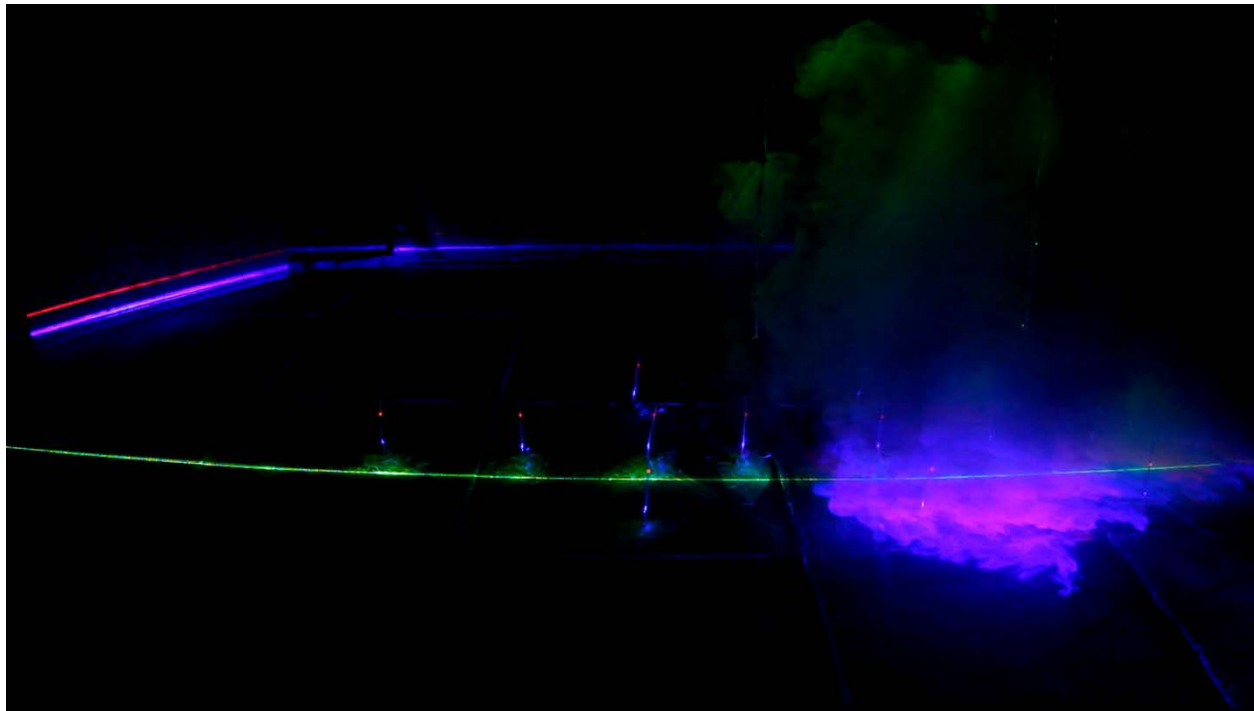
Fig. 2

Figs. 1-2. Diagram of the experimental setup in air. The three colored areas are the three light sheets, the green sheet illuminating the downstream plane, and the blue and red sheet illuminating the map-view plane at 5 and 25 cm above the floor respectively. The experiments are fed by the conveyor belt and the chute on the right of the diagram. And a photograph from experiment A4.

13
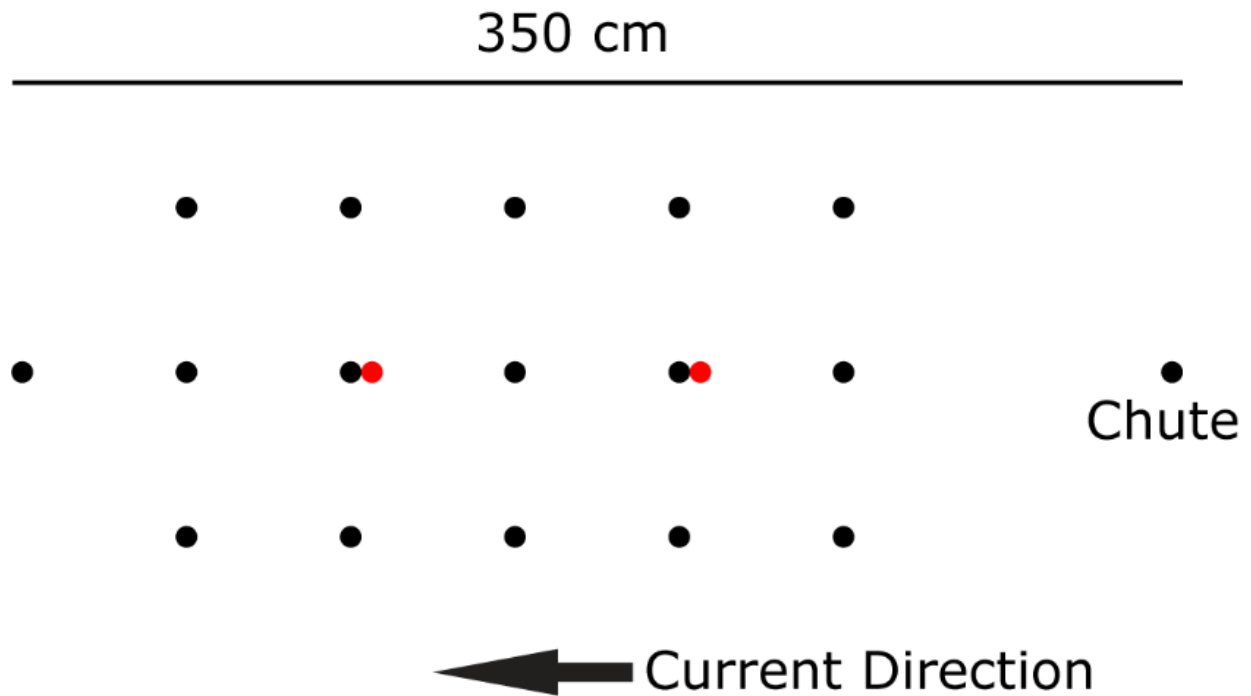
Fig. 3. Diagram of the thermocouple layout in the tank. The black dots are the locations of the thermocouples along the floor, at positioned at heights of 5 and 30 cm above the floor at all locations. The lone black dot on the right is at 0 cm, the chute, and the lone black dot on the left is at 350 cm. The red dots are where the thermocouples are positioned vertically, at 150 and 250 cm from the chute. Thermocouples are 65, 100, and 150 cm above the floor at these positions.
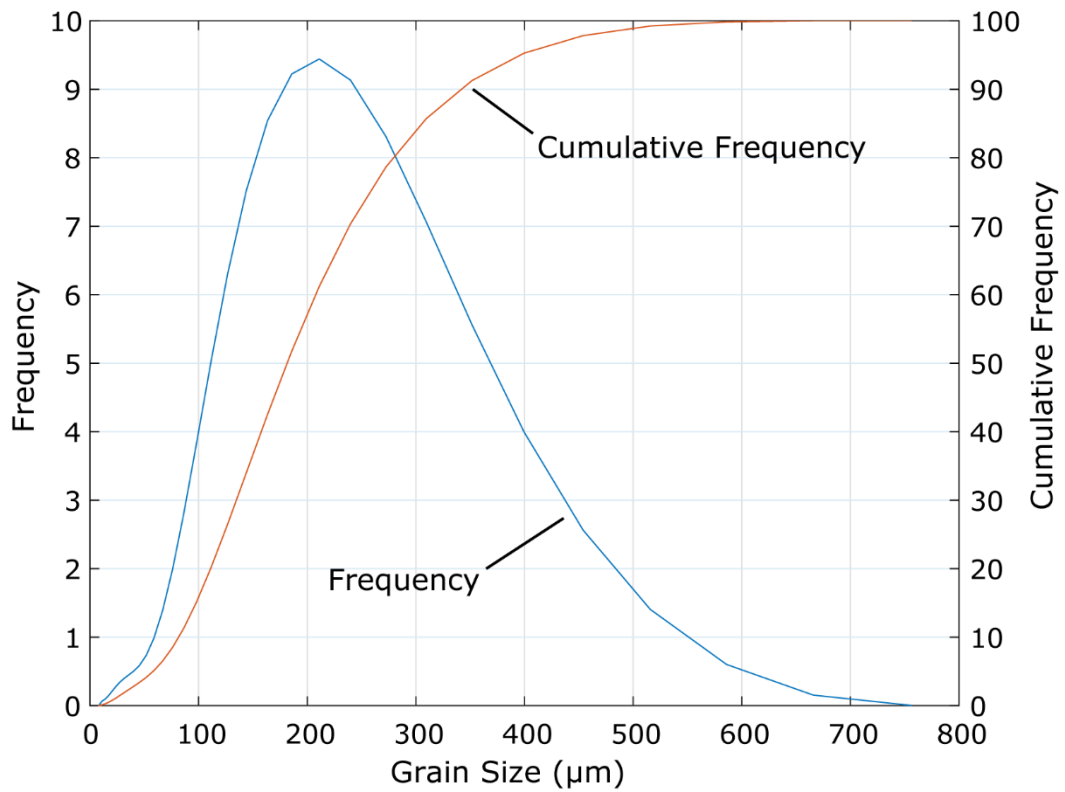
Fig. 4. Frequency and cumulative frequency of grain sizes of the plastic pellets used for the particles in the water experiments. The d_{50} grain size is 186 μm.
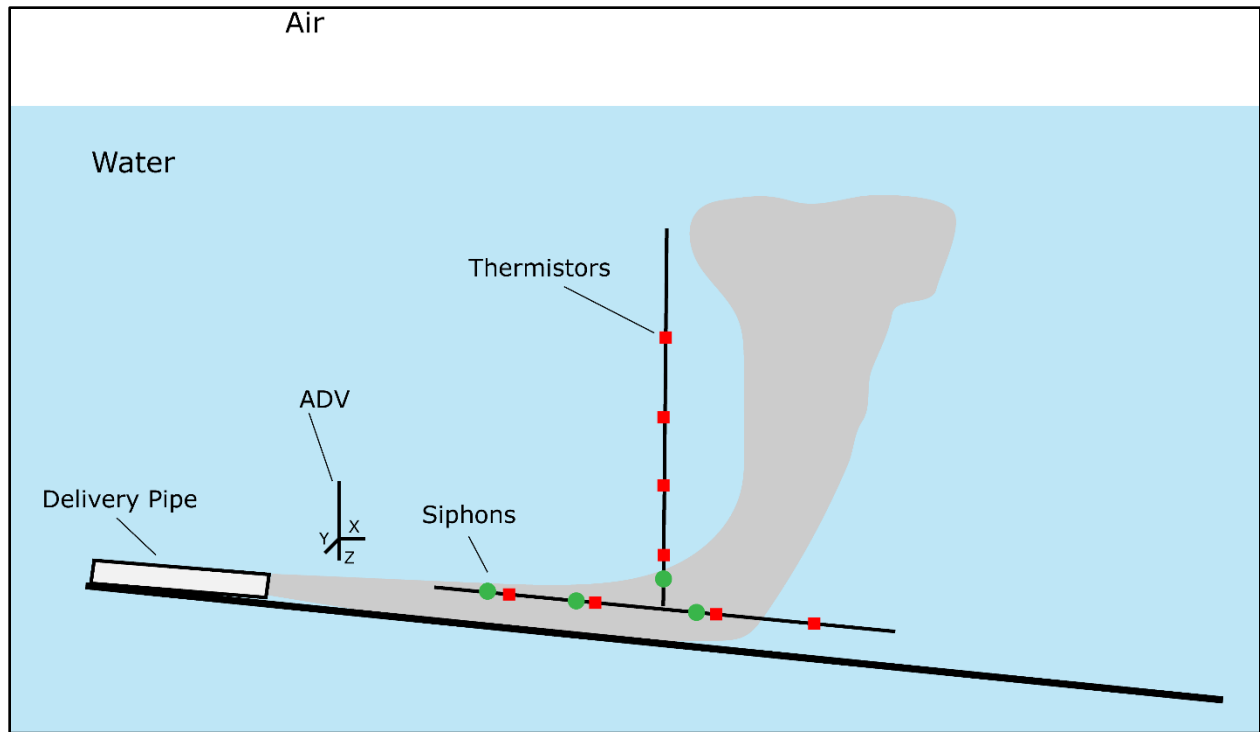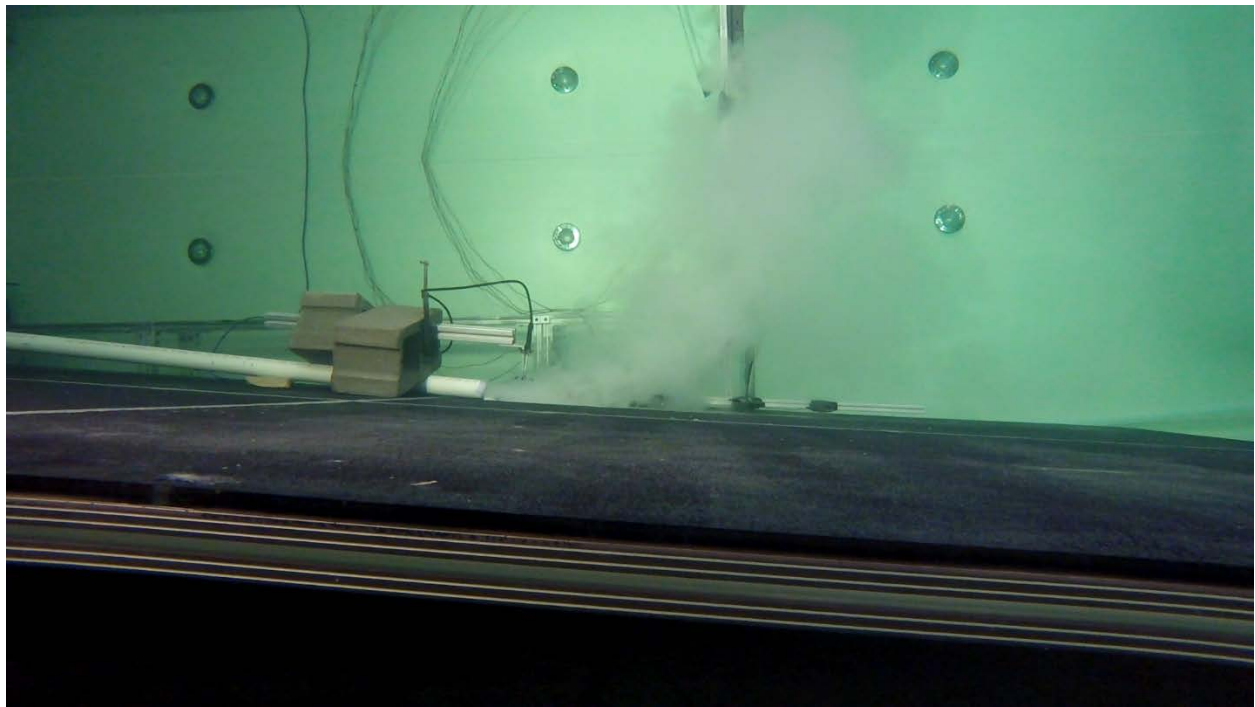
Fig. 5

Fig. 6

Fig. 5-6. Diagram and photograph of the experimental setup in water. The current enters the water from the 5 cm wide delivery pipe on the left. It flows down the platform and passed underneath the ADV, and then flow by the thermistors (red dots) and siphons (green dots). The current eventually lifts off, or in ground-hugs in the case of the turbidity current.

Results

Behavior of currents in air

A summary of the results of each experimental current is given in Table 2. Experiments in air were conducted with three different starting temperatures, 93 °C, 121 °C, and ambient temperature. Three experiments each were run at 93 °C and 121 °C with 5, 10, and 30 second time gaps, and a ambient temperature current with a 10 second time gap. The heated currents began flowing as ground-hugging currents which eventually reversed buoyancy. The heads, tops, and sides of the currents had turbulent eddies and billows, entraining ambient air. The trailing current entered the tank after the specified time gap for the experiments. All of the heated currents had a large length/width ratio (Fig. 7). The ambient temperature current did not lift off and ran out to the end of the tank.

The average velocity of the currents measured at 150 cm from the chute ranged from 10 – 25 cm/s, and the velocity of the currents generally decreased with distance from the chute (Fig. 8). Some currents had a pulsating nature as they exited the chute, causing the body of the current to propagate with a non-constant velocity. The 93 °C currents had an average velocity of 18.3 cm/s and the 121 °C currents had an average velocity of 11.7 cm/s. The *Re* of the currents were on the order 10^3, which is in the turbulent flow regime. *Ri$_B$* was less than 1, so entrainment of ambient fluid occurred. *Ri$_B$* for the ambient temperature currents were much higher than heated currents; *Ri$_B$* for one current was higher than 1, and therefore that current was not able to entrain ambient air. *Pn* of the currents ranged 1-5, so that the particles were moving in bed load or suspended load. *Fr* was less than 1 in all heated experiments, which allowed for any disturbances affecting the head of the current to propagate upstream into the body of the current.

And γ was between 0 and 1 for the heated currents, which were able to become buoyant, and 0 for the ambient temperature current, which did not become buoyant.

The trailing current average velocity was slower than the leading current, and because entrainment of ambient air depends on Ri_B, entrainment was greater in the leading current than in the trailing current in both the 93 °C and 121 °C experiments (Fig. 9). For the 121 °C currents, the temperature rises to a maximum of about 4.5 °C above ambient, and for the 93 °C temperature rises to a maximum of 3 °C above ambient (Fig. 10-11). After each current stopped being fed, the temperature began to decrease back toward ambient temperature. In experiments with shorter length time gaps, temperature did not decrease as much between currents as in experiments with longer time gaps.

The intensity of red light in the trailing currents was less than that in the leading currents. Assuming the intensity of red light is a proxy particle concentration in the currents, the difference in light intensity suggests that the particle concentration in the trailing currents was less than the leading currents in all experiments (Fig. 12). The height of the leading plume above the bed varied with time gap and with initial current temperature (Fig. 13). The leading plumes with 30 second time gaps rose to the ceiling of the tank and spread out, which took them completely out of the way of the trailing plumes. The leading plumes of the 10 second time gap experiments had also risen to the ceiling in the 121 °C experiments but did not rise all the way to the ceiling in the 93 °C experiments. For the 5 second time gaps, the 121 °C leading plume rose off the bed, but in the 93 °C experiment the leading plume was still forming and just beginning to rise when the trailing current reached it.

Runout distance was measured as the distance between the mouth of the chute and the position along floor where the current underwent buoyancy reversal. The position of buoyancy

reversal was defined as the point where the entire head of the current stopped flowing forward and began to flow upward. Overall, the 121 °C currents had shorter runout distances than the 93 °C currents. The hotter currents travelled an average of 2.06±0.1 m before lifting off, and the cooler currents travelled an average of 2.72±0.1 m before lifting off. The trailing currents, in all of the heated experiments, had shorter runout distances than leading currents (Fig. 14).

The ambient temperature currents travelled 8.5 m, the length of the tank. The ambient temperature currents were not hotter than the ambient air, so there was no buoyancy force acting on the current. The ambient temperature talc powder is much denser than air, and without a buoyancy force, the currents could not lift-off.

Behavior of currents in water

Lofting experiments in water were conducted with time gaps between the leading and trailing heated currents of 10, 20, 30, 40, and 60 seconds. Two other types of experiments were conducted: Non-buoyant, ambient temperature with a 20 second time gap and hot water-only currents with a 20 second time gap. The currents began well-mixed in a head tank, and when the valve on the head tank was opened, flowed down through the pipe carrying the current into the pool. The leading particle-laden, heated current entered the pool and flowed down the platform, acting as a ground-hugging current, and then reversed buoyancy and lifted off. The head and top of the current showed the presence of turbulent eddies and billows, and the current thickened as it flowed down the platform. After a requisite amount time passed, the valve on the head tank was opened again, and a well-mixed trailing current flowed into the pool. The general behavior of the trailing currents was the same as the leading currents, except that the trailing plume tended to rise into the leading plume. The currents remained narrow, and had a high length/width ratio

19

(Fig. 15). The ambient temperature current, being at the same temperature as the pool, was not

buoyant and did not lift off. The hot water current entered the pool and lifted off immediately.

The average downstream velocity of the currents ranged from 12-17 cm/s, and the trailing

currents flowed at a different velocity than the leading currents. *Re* of each current was on the

order of 10^3, thus the currents were fully turbulent. *Ri$_B$* <1 for each current so that they freely

entrain ambient fluid. *Pn* range from 4-6, so the particles were moving as bed load and

suspended load. *Fr* was less than 1 in all experiments, so disturbances at the head of the currents

could propagate upstream into the body. And γ was between 0 and 1 for all particle-laden,

heated currents indicating that all were capable of becoming buoyant and lifting off. The γ

values for the ambient temperature currents were 0, and thus unable to become buoyant. The

average velocity, of the trailing currents in the experiments with 20, 30, and 40 second time gaps

was faster than the leading currents, suggesting that entrainment in the trailing currents was

greater, based on *Ri$_B$*. In 10 and 60 second time gap experiments, the trailing current velocity

was the same or less than the leading current velocity, and entrainment was therefore less than

the leading currents (Fig. 16).

The downstream velocity of the currents decreased with distance from the pipe (Fig. 17).

Velocities were not the same at different depths in the currents (Fig. 18-24). In the experiment

with just hot water, the highest velocity in the X, Y, and Z directions is at the top of the current.

In the ambient temperature current, the highest velocity in downstream direction was in the

middle of the current (depth-wise), which is commonly seen in turbidity currents (Parker et al.,

1986). The highest vertical velocity in the turbidity current was near the bed. In the heated,

particle-laden currents, the velocity structure varied between experiments. The highest

downstream velocity was at the highest measured position above the floor for all currents and

time gaps. The highest vertical velocity varied with time gap. In the two time gap endmember experiments, 10 and 60 seconds, the highest vertical velocity was at the top of the current for both the leading and the trailing current. In the 20 and 30 second time gap, and somewhat in the 40 second time gap, the location of the highest vertical velocity in the leading current was at the top of the current, as in the other two experiments. In the trailing current in these experiments (20, 30 and 40 second time gaps), the vertical velocity at the top of the current is high when the current begins, but soon starts to slow to less than the vertical velocity near the bed. When this change occurred, the trailing current began lifting off at greater distances than the leading current.

The maximum temperature difference between the current and ambient water along the bed was 7 °C near where the current entered the pool, but decreased to 1 °C near where the current lifted-off. In the time gap between flowing currents, the temperature rapidly decreased toward ambient. The amount of temperature decrease varied with time gap between currents. In the 10 second time gap experiment, the temperature did not return back to ambient temperature but remained elevated by 0.7 °C. The trailing current flowed into a warmer ambient fluid than the leading current. In the 20 and 30 second time gap experiments, the water temperature did decrease to ambient, but did not stay at that temperature for an extended period of time because the trailing current flowed into the pool. The water temperature decreased to ambient temperature and stayed there for ≈43 seconds during the 60 second time gap experiment, and ≈32 seconds during the 40 second time gap experiment (Fig. 25).

Both the leading and trailing currents in water began flowing with the same particle concentrations because the head tank was well mixed through the duration of the experiment. Particle concentration in the currents decreased with distance from the pipe. The particle

concentration was used to calculate the density of the current at the position of the siphons. When both the leading and trailing currents began flowing, they were less dense than the surrounding water, and increased with distance as temperature and particle concentration decreased (Fig. 26). However, the currents did not lift-off immediately, because the downstream current velocity stayed fast enough for long enough for the downstream momentum to overcome the buoyancy forces. The currents could only lift-off after they slowed down enough such that buoyancy forces overcame forward momentum. The currents do not need to stop to lift off, when they do lift off they take on the shape of the letter "J." The mass concentration of particles also differed between the leading and trailing currents (Fig. 27). In the 20, 30, and 40 second time gap experiments, the trailing current particle concentration is greater than the leading current over the length of runout. In the 10 and 60 second experiments, the trailing current particle concentration exceeds that of the leading current near the pipe, but becomes less downstream.

In all lofting experiments, the head of the rising plume reached the top of the water column and spread laterally. The height above the floor of the tail of the leading currents correlates with a trend in density and time gap (Fig. 28). The trailing currents lifted off below the leading plumes, and created a density contrast between the tail of the leading plume and the head of the trailing plume. After the 10 second time gap, the tail of the leading plume was 8 cm above the floor and was also denser than the head of the trailing current when it lifted-off. In the experiments with 20, 30, and 40 second time gaps, the height above the floor of the tail of the leading plume became continually greater when the trailing current lifted off. The density of the leading plume was less than that of the incoming trailing plume in all three experiments. After the 60 second time gap, the leading plume was 60 cm above the bed, higher than after any

shorter length time gap, but its density was equal to that of the trailing plume. When the trailing current entered the pool, it began to lift-off at or near the same distance the leading current did. After the 10 and 60 second time gaps, when the trailing plume reached the height of the tail of the leading plume it kept rising through the remnants of the leading plume. In the 20, 30, and 40 second time gap experiments, when the trailing plume reached the height of the remnants of the leading plume, it stopped rising, but the current feeding it kept flowing downstream, changing the position of the trailing plume.

The hot water currents had the shortest runout distances of any currents, with an average runout distance of 0.33±0.1 m. The lack of particles meant the currents were never denser than the ambient fluid. The turbidity currents, not being hot and buoyant, ran out the entire length of the platform, and then flowed off the end of the platform, 2.31±0.1 m away.

The heated particle-laden currents had runout distances between that of the hot water currents and the turbidity currents, with an average distance of 0.69 m. At short and long time gaps, the runout distance of the trailing current does not change much from the leading current, and at moderate time gaps the runout distance of the trailing current changes drastically from the leading current (Fig. 29). After the 10 and 60 second time gaps, the trailing current had a runout distance nearly the same as that of the leading current. After the 20, 30, and 40 second time gaps, the trailing current had a much longer runout distance than the leading current.

Experiment	Time Gap (s)	Source Temperature (°C)	Ambient Temperature (°C)	Average Velocity (m/s)		Runout (m)		Re		Ri$_B$		Fr		Pn		γ	
				Leading	Trailing	Leading	Trailing	Leading	Trailing	Leading	Trailing	Leading	Trailing	Leading	Trailing	Leading	Trailing
Air Medium																	
A1	5	93	22	0.17	0.17	2.83	2.36	4458	4458	0.37	0.38	0.17	0.17	2.65	2.65	0.46	0.45
A2	10	93	22	0.17	0.17	2.59	2.27	4458	4458	0.35	0.40	0.17	0.17	2.65	2.65	0.50	0.43
A3	30	93	21	0.25	0.17	2.75	2.41	6555	4458	0.07	0.16	0.25	0.17	1.81	2.65	0.78	0.77
A4	5	121	22	0.13	0.10	1.79	1.59	3399	2614	0.42	0.81	0.13	0.10	3.48	4.52	0.65	0.60
A5	10	121	20	0.10	0.10	1.78	1.46	2614	2614	0.09	0.12	0.10	0.10	4.52	4.52	0.96	0.94
A6	30	121	20	0.17	0.10	2.62	2.45	4444	2614	0.02	0.19	0.17	0.10	2.66	4.52	0.97	0.91
A7*	10	22	22	0.15	0.13	8.50	8.50	3978	3447	0.89	1.18	0.15	0.13	2.99	3.45	0.00	0.00
Water Medium																	
W1†	20	29	19	0.14	0.13	0.35	0.31	6693	6216	-0.0156	-0.0155	0.2238	0.2078	-	-	-	-
W2	10	27	21	0.12	0.11	0.40	0.43	5547	5365	0.0221	0.0363	0.1853	0.1792	5.4937	5.6799	0.6646	0.4846
W3	20	28	21	0.11	0.14	0.52	0.90	5268	6680	0.0112	0.0080	0.176	0.2231	5.7891	4.5658	0.8461	0.8238
W4	30	29	23	0.13	0.16	0.96	1.23	6300	7525	0.0132	0.0094	0.2105	0.2514	4.844	4.0557	0.7417	0.7367
W5	40	28	21	0.12	0.13	0.44	0.66	5651	6364	0.0159	0.0127	0.1888	0.2126	5.397	4.7924	0.7503	0.7456
W6	60	28	21	0.12	0.12	0.53	0.61	5618	5847	0.0163	0.0151	0.1876	0.1953	5.4292	5.2159	0.7456	0.7456
W7*	20	21	22	0.13	0.13	2.31	2.31	5992	5992	0.0616	0.0594	0.1998	0.1998	5.0653	5.0653	-0.0994	-0.0591

Table 2. Results of experimental density currents. Source temperature is the temperature of current particles (and in water experiments, the interstitial fluid). Ambient temperature is the temperature of the fluid in the tank. Runout distance is the distance from the point where the current enters the tank to where it undergoes buoyancy reversal. The Reynolds number (Re) is the ratio of inertial forces to viscous forces. The bulk Richardson number (Ri$_B$) is ratio of buoyancy to flow shear. The Froude number (Fr) is the ratio of inertial forces to weight. The Rouse number (Pn) describes the mode of sediment transport. γ is the buoyancy constant of Hogg et al. (1999). †Hot water only. *Ambient temperature current.
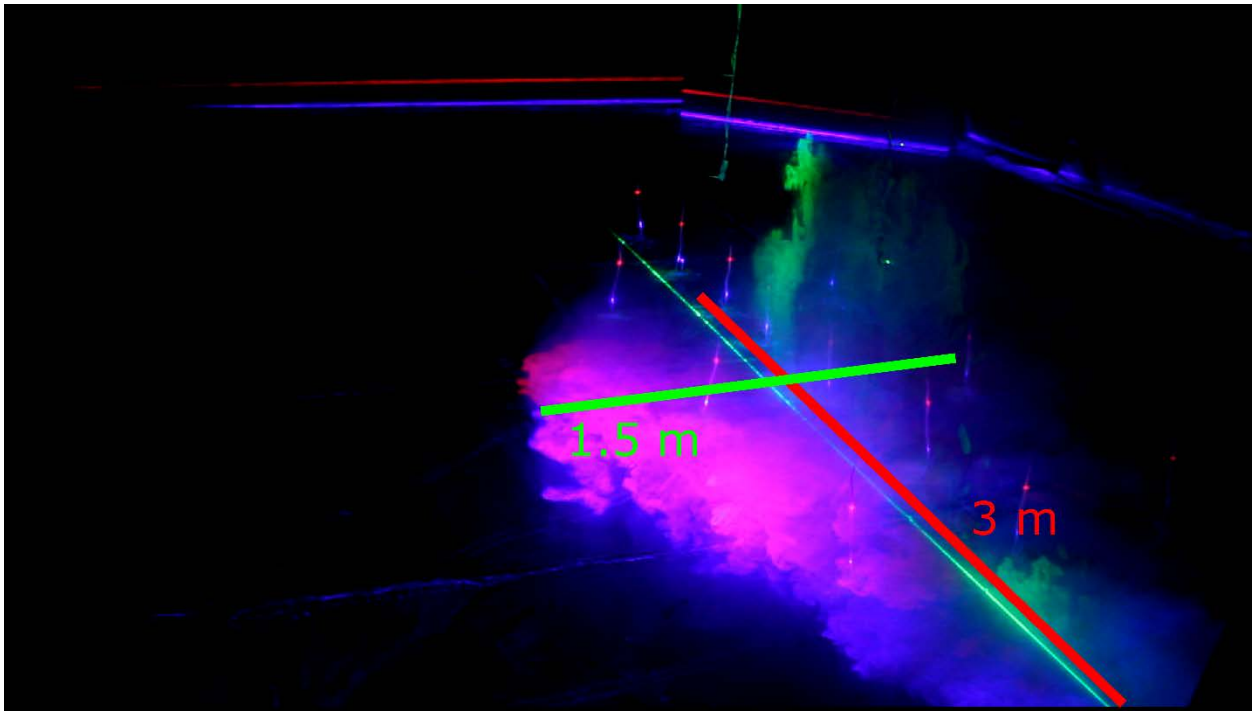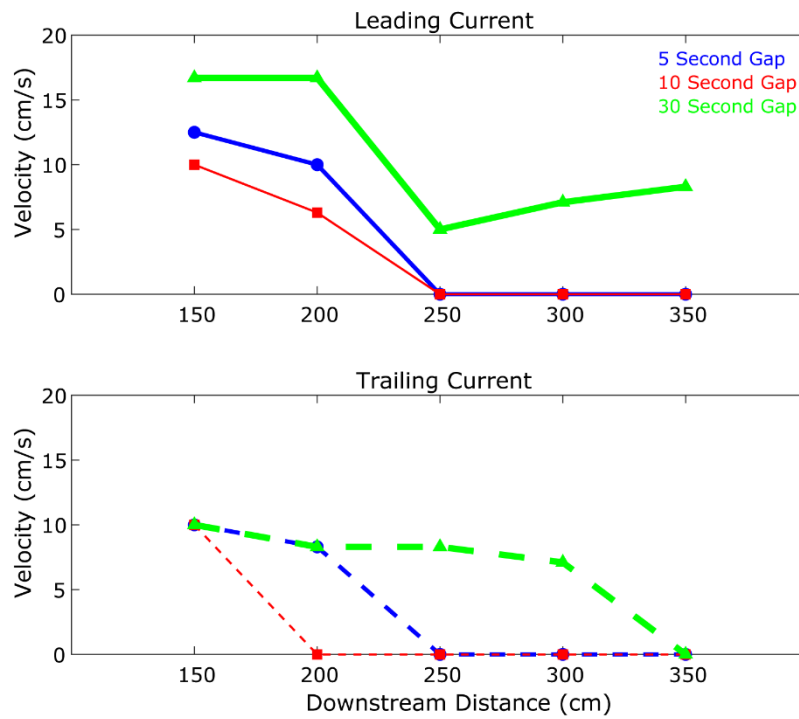
Fig. 7. Leading current of experiment A6. The length of the current is much longer than the width. Turbulent billows are visible on the top and edges of the current.
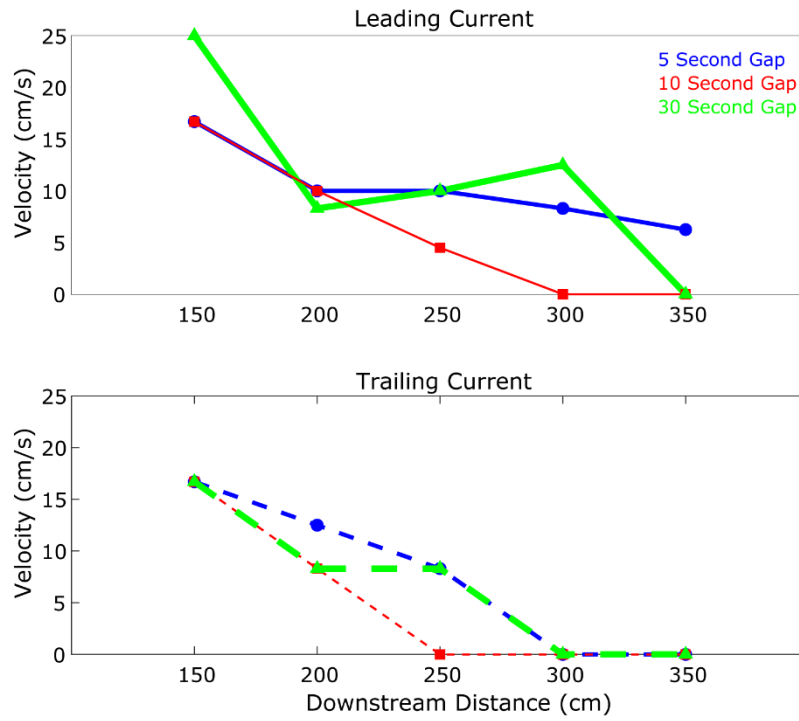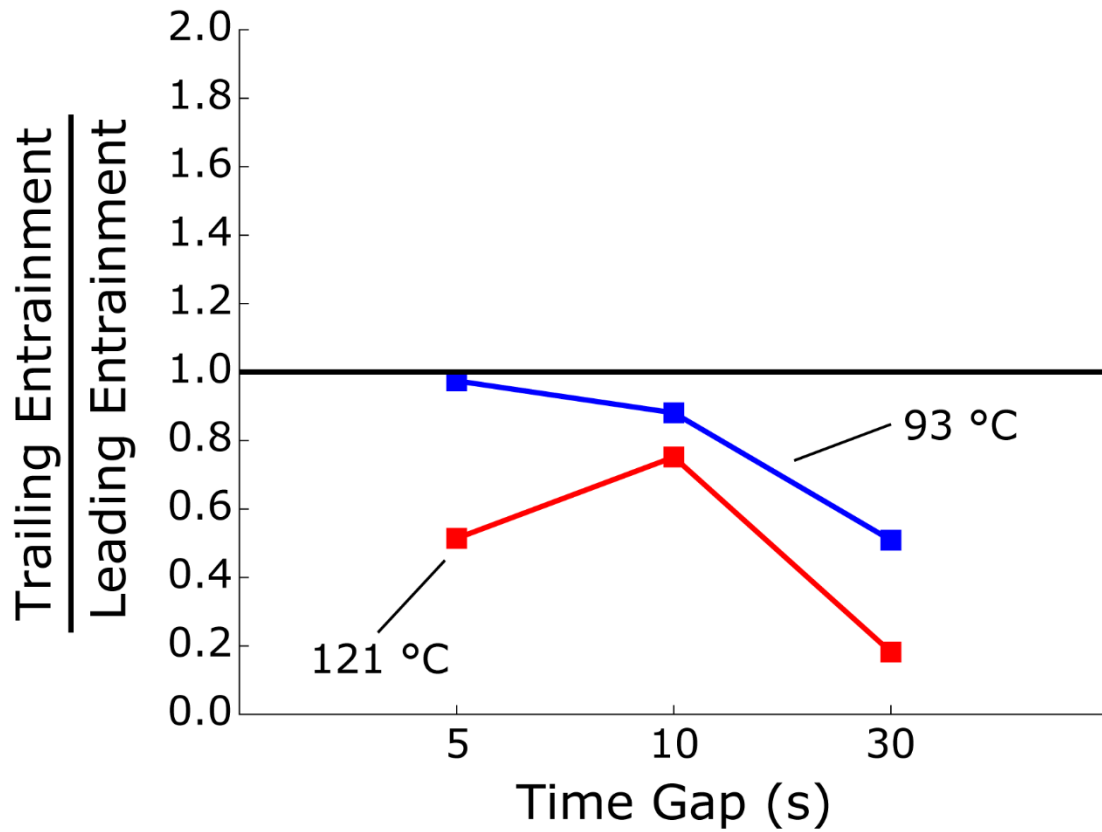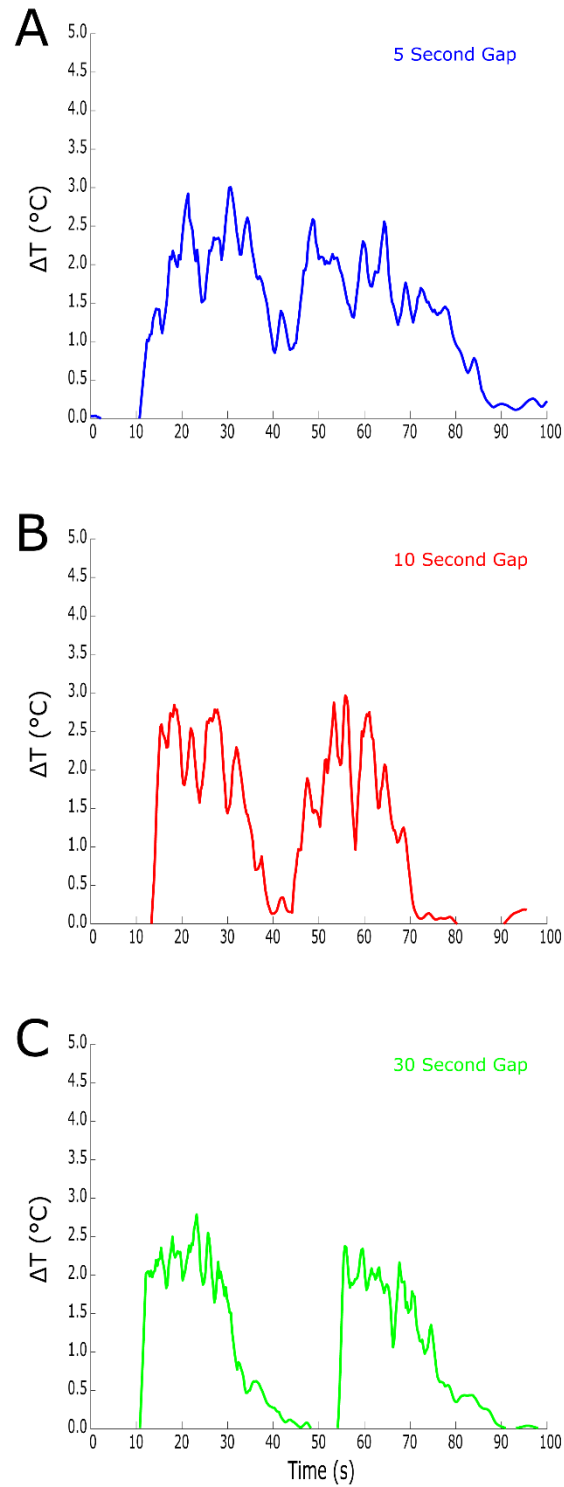
Fig. 8. A) Head velocity with distance for the 93 °C experiments in air. B) Head velocity with distance for the 121 °C experiments in air.

Fig. 9. Entrainment in the trailing current of the experiments in air relative to entrainment in the leading current. Entrainment was calculated using the equation of Parker et al. (1987).

Fig. 10. Change in temperature from ambient air of the 93 °C experimental currents, recorded at 1 m from input point and 5 cm above the bed. A) 5 second time gap. B) 10 second time gap. C) 30 second time gap.
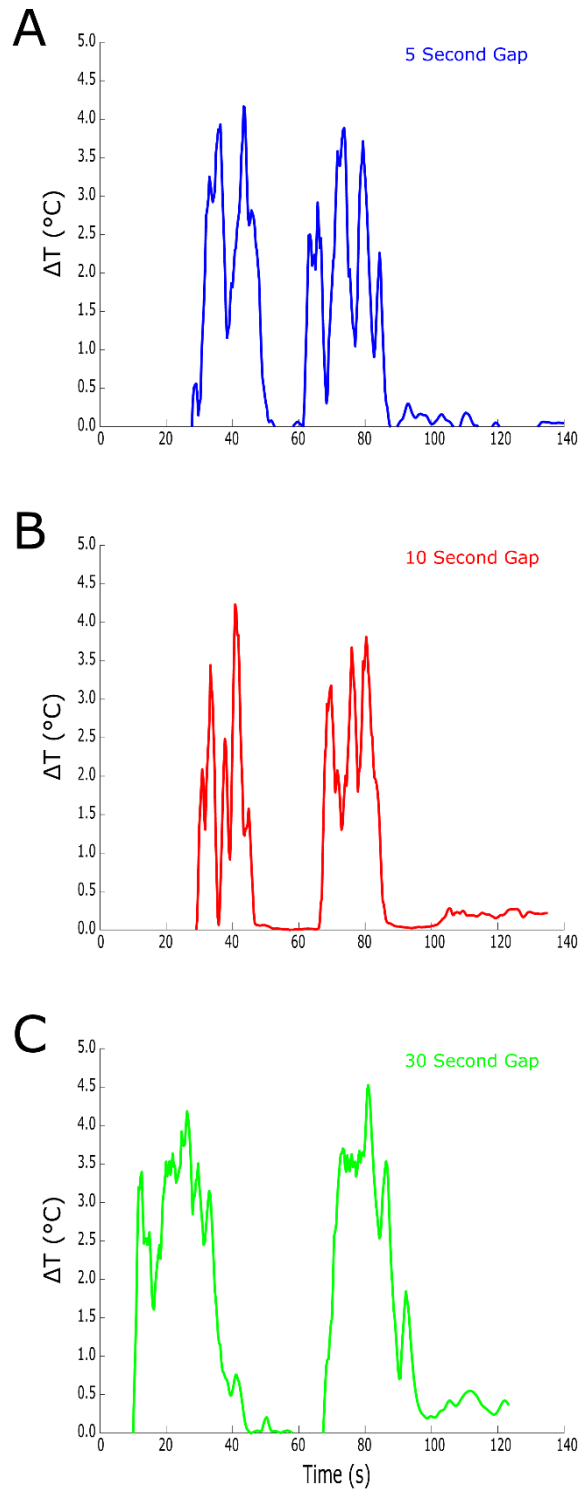
Fig. 11. Change in temperature from ambient air of the 121 °C experimental currents, recorded at 1 m from input point and 5 cm above the bed. A) 5 second time gap. B) 10 second time gap. C) 30 second time gap.
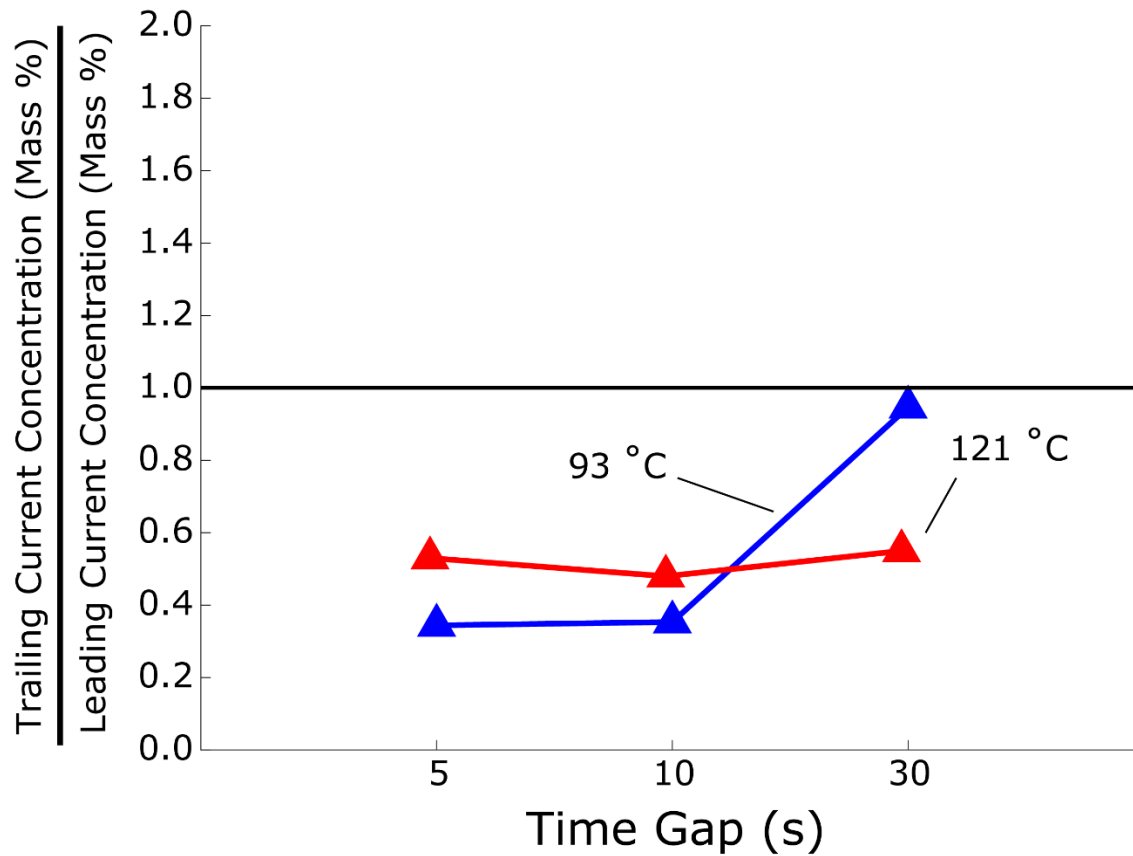
Fig. 12. Mass proxy of the trailing current relative to the mass proxy of the leading current in air for time gaps of 5, 10, and 30 seconds, at both 93 °C and 121 °C. The trailing currents were less dense than the leading currents.
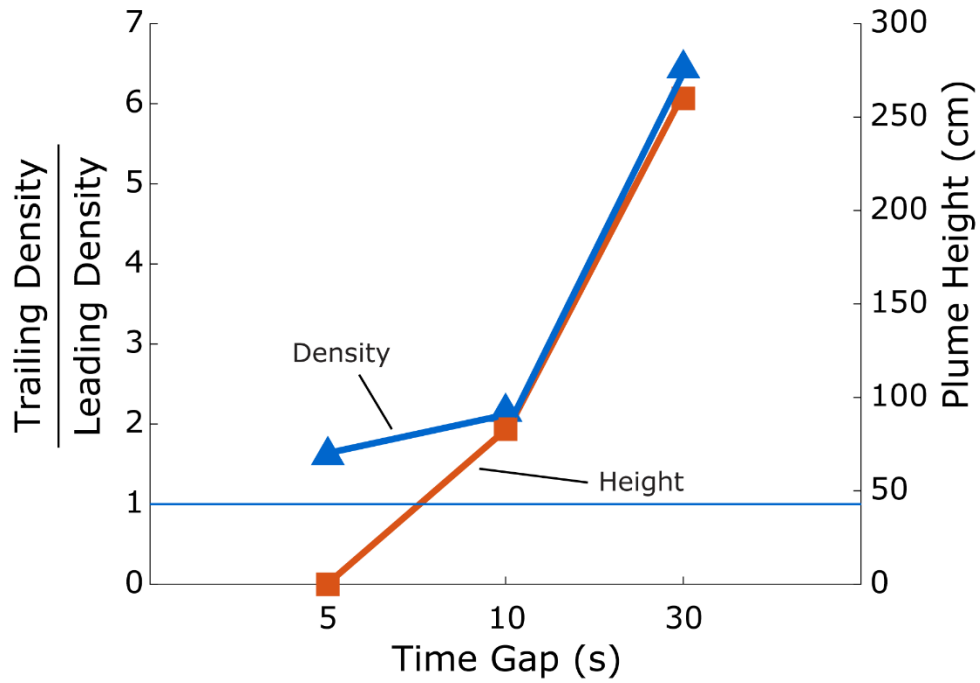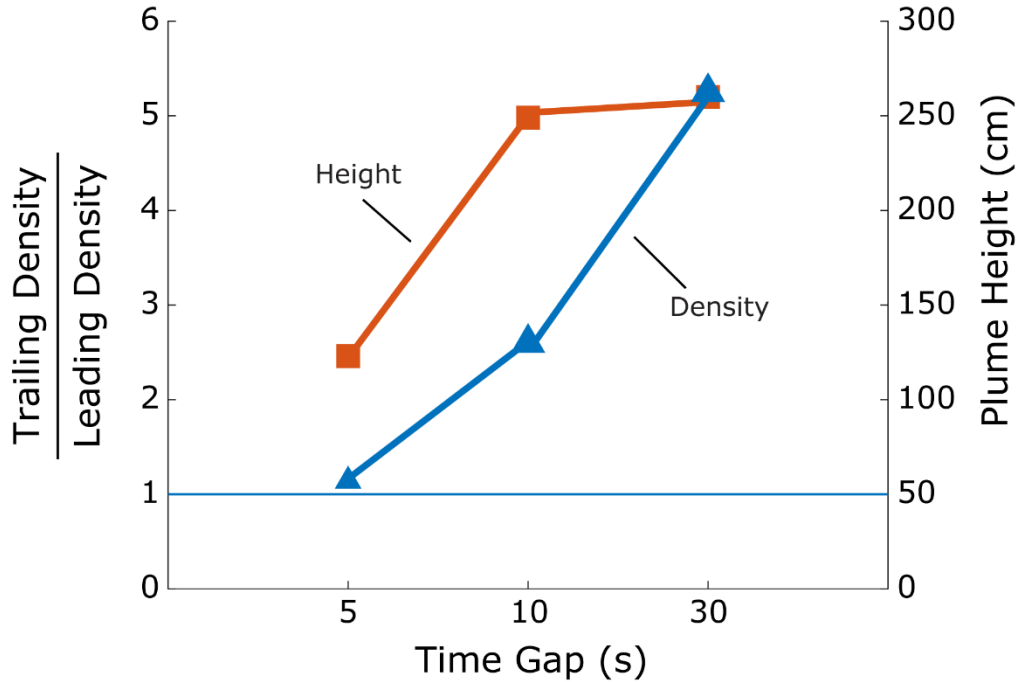
Fig. 13. Height and ratio of plume densities as a function of time gap between currents. Plume density ratio between head of trailing plume to tail of leading plume. A) 93 °C experiments. B) 121 °C experiments.
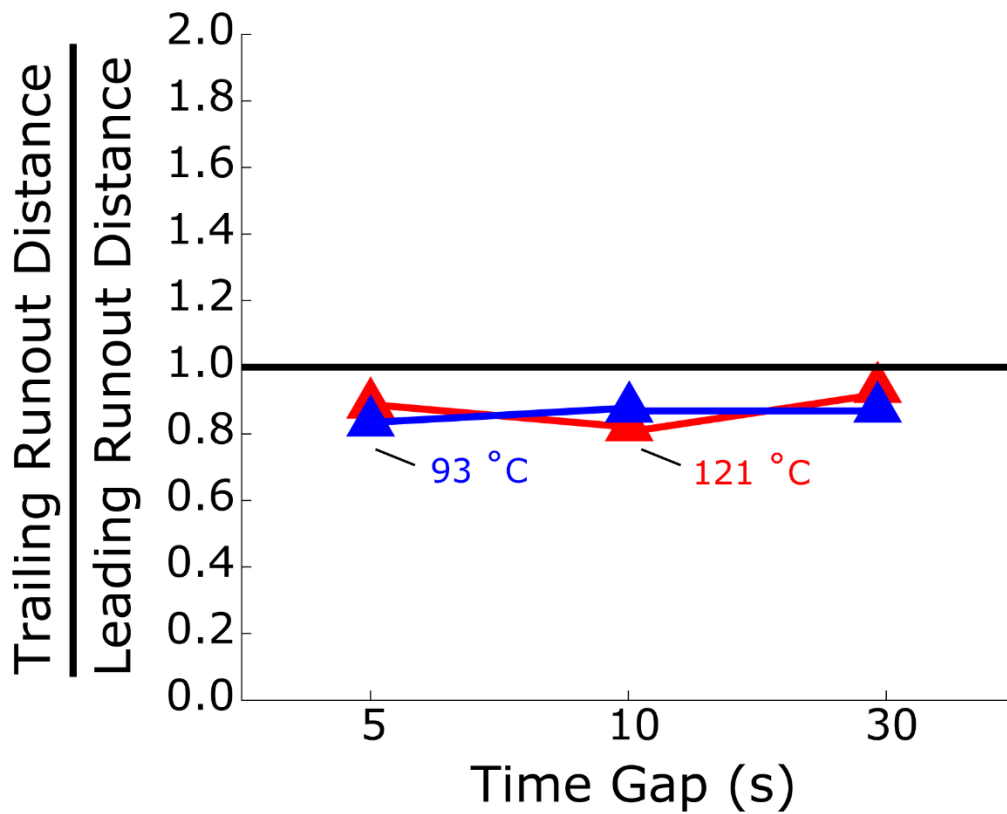
Fig. 14. The runout distance of the trailing current relative to the runout distance of the leading current in air for time gaps of 5, 10, and 30 seconds, at 93 °C and 121 °C. The trailing current did not run out farther than the leading current in all experiments in air.
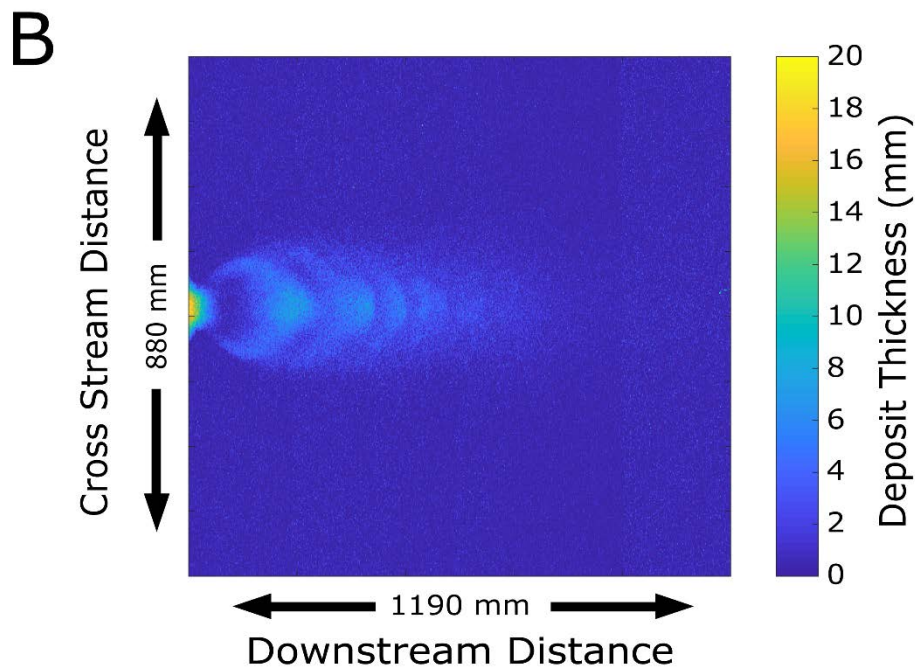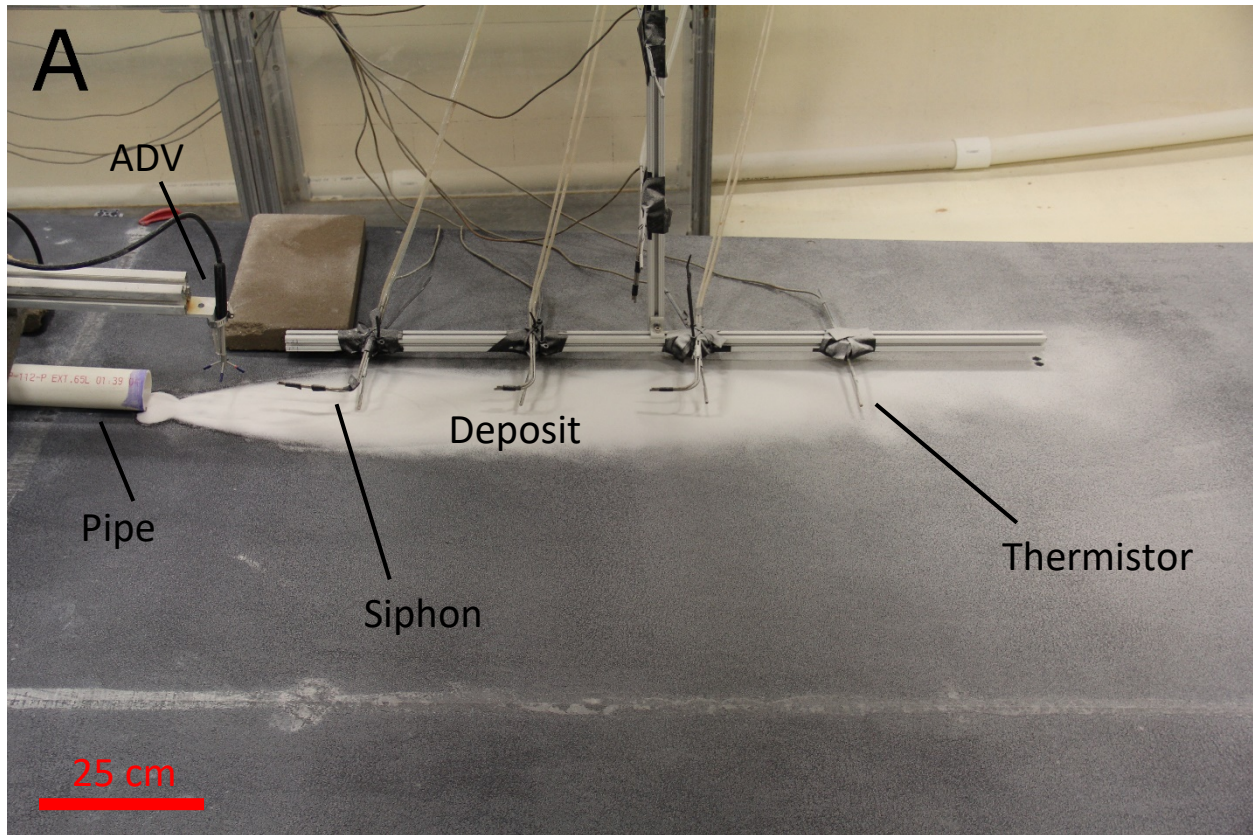
Fig. 15. The deposits of the experiments in water. A) A photograph of the deposit from experiment W3. Current direction is from left to right. Observe the high length/width ratio of the deposits. B) A difference map of a deposit. Ripple forms are visible in the deposit, indicating particle movement by traction. Current direction is from left to right.
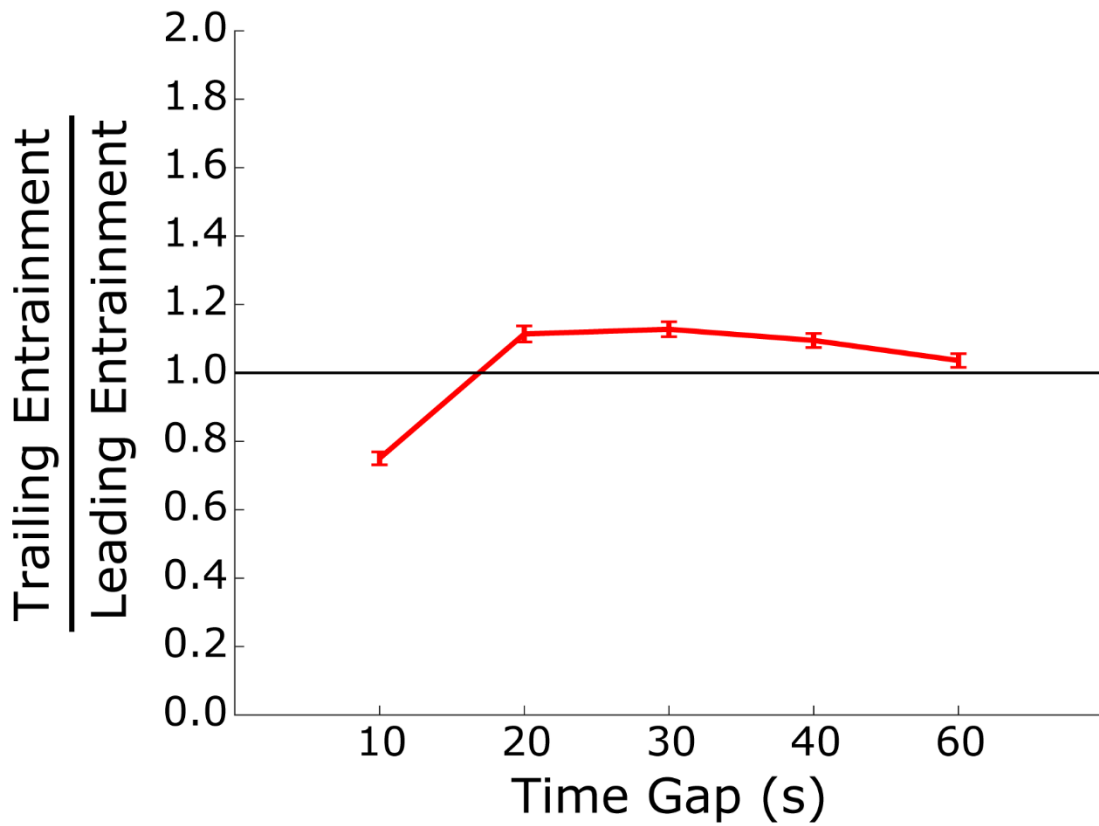
Fig. 16. Entrainment of ambient water by the trailing current relative to the leading current. Entrainment was calculated using the equation of Parker et al. (1987).
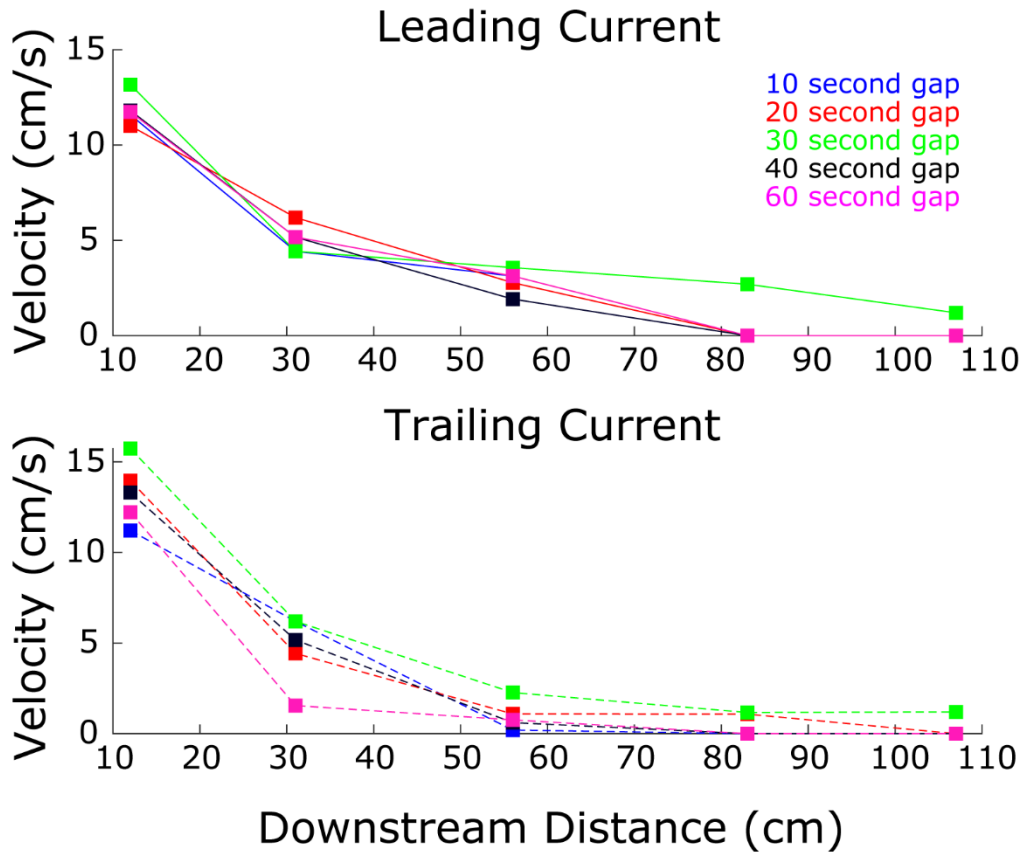
Fig. 17. Head velocity of the lofting currents with distance from the pipe. The head velocity of the currents decrease with distance until they lift off.
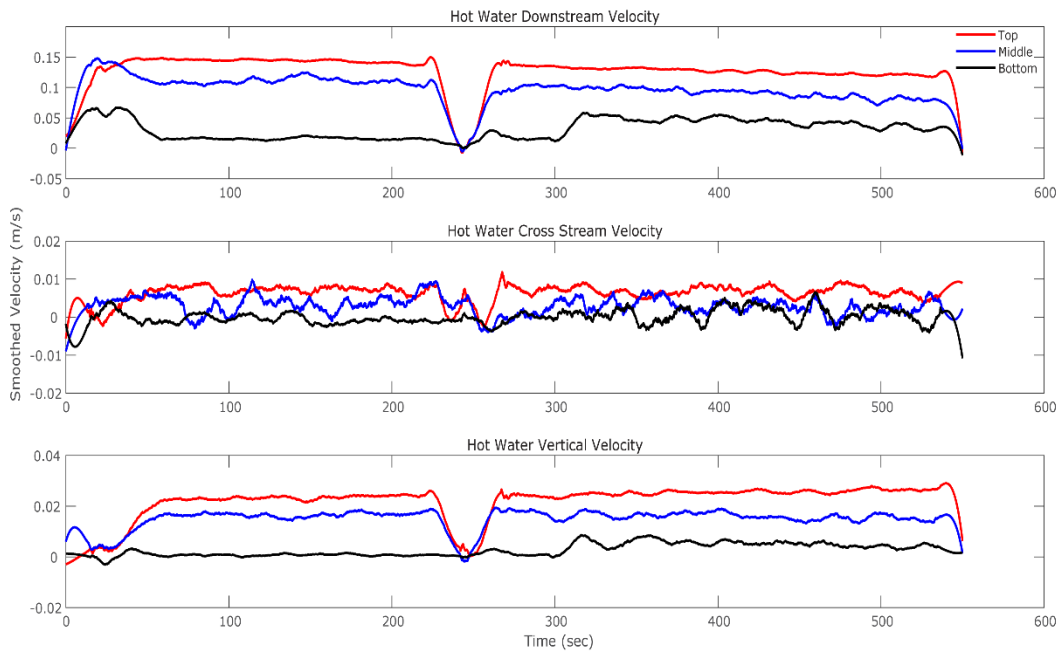
Fig. 18
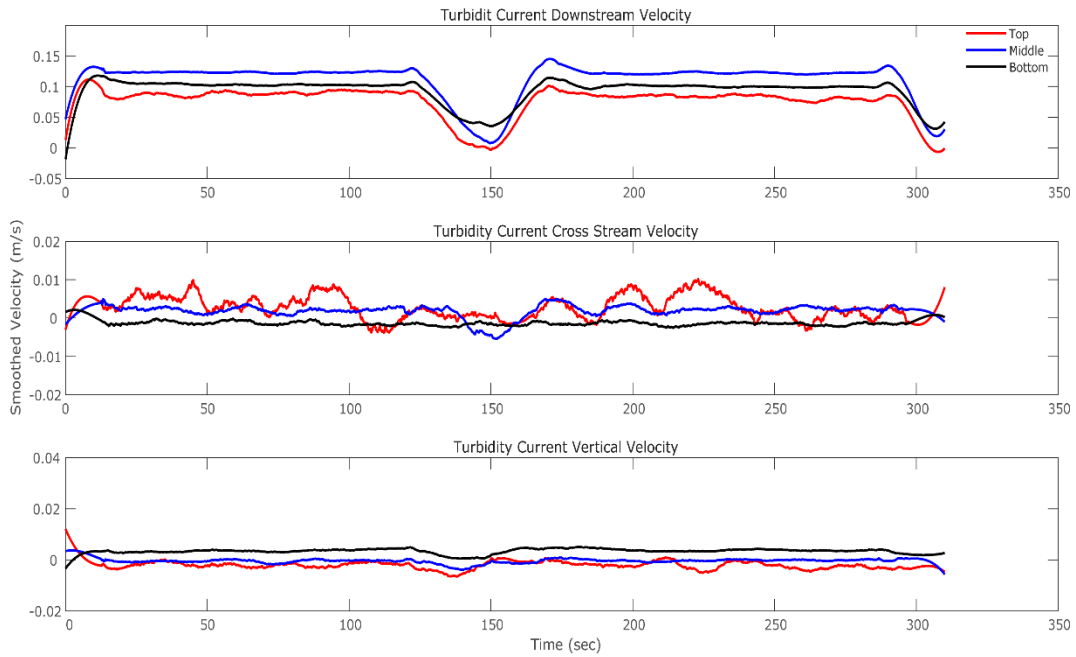
Fig. 19
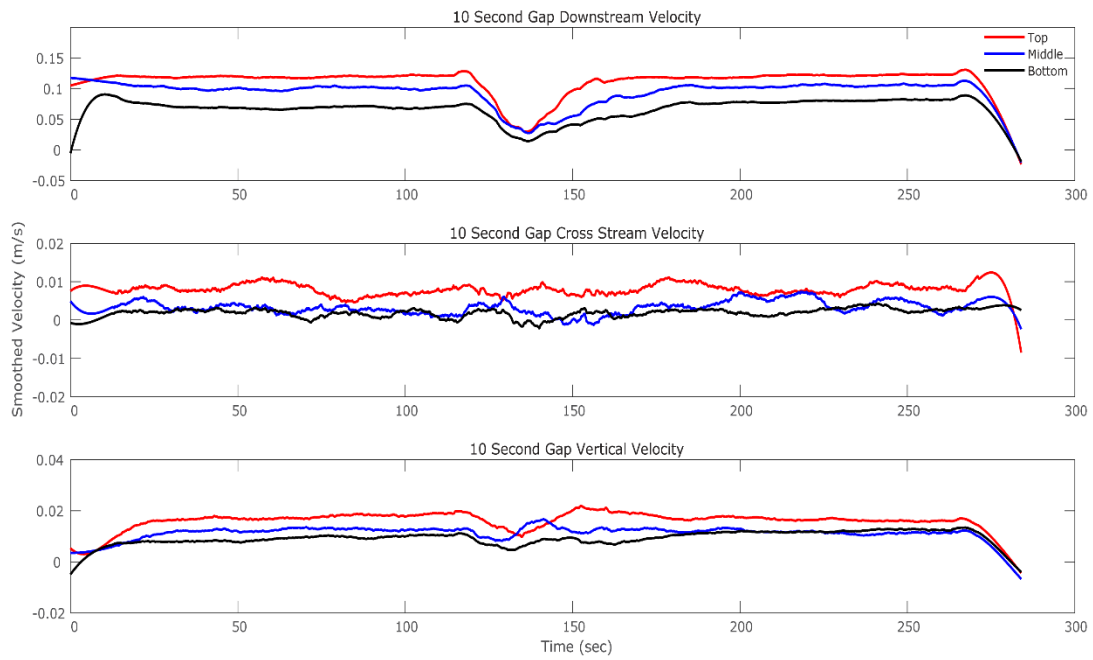
Fig. 20

Fig. 21

Fig. 22

Fig. 23

38
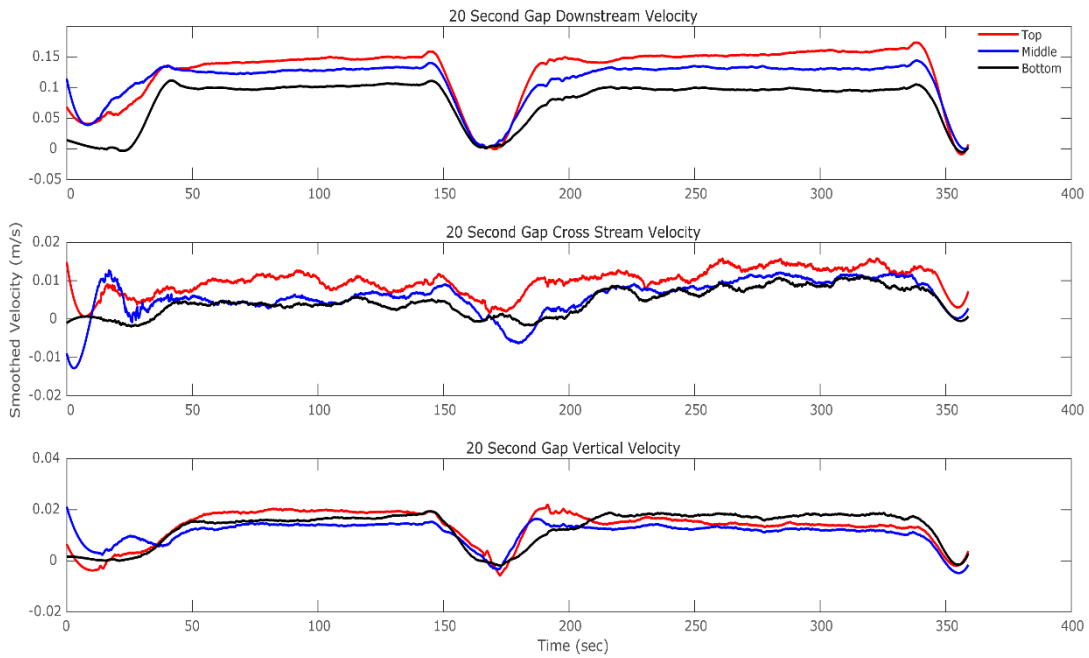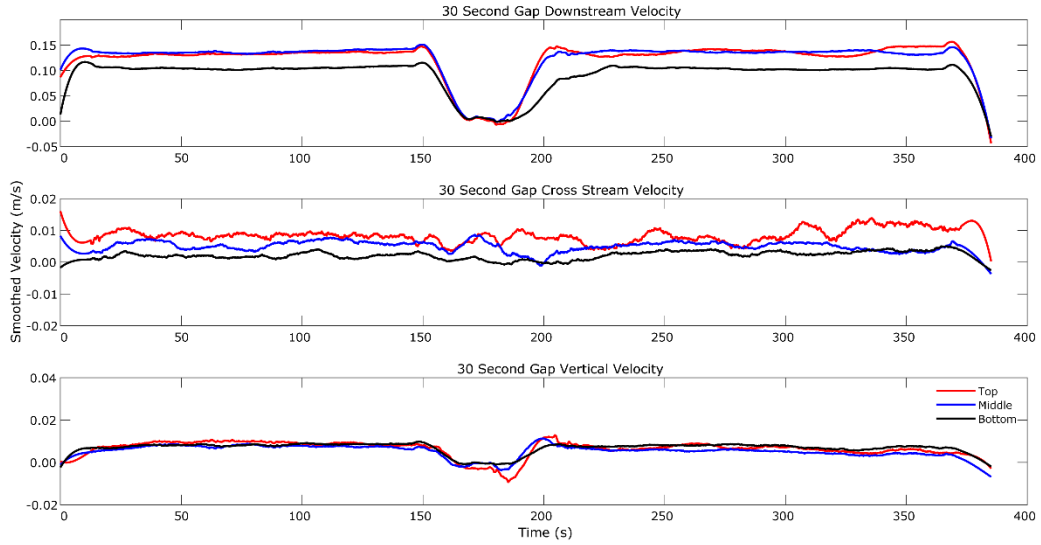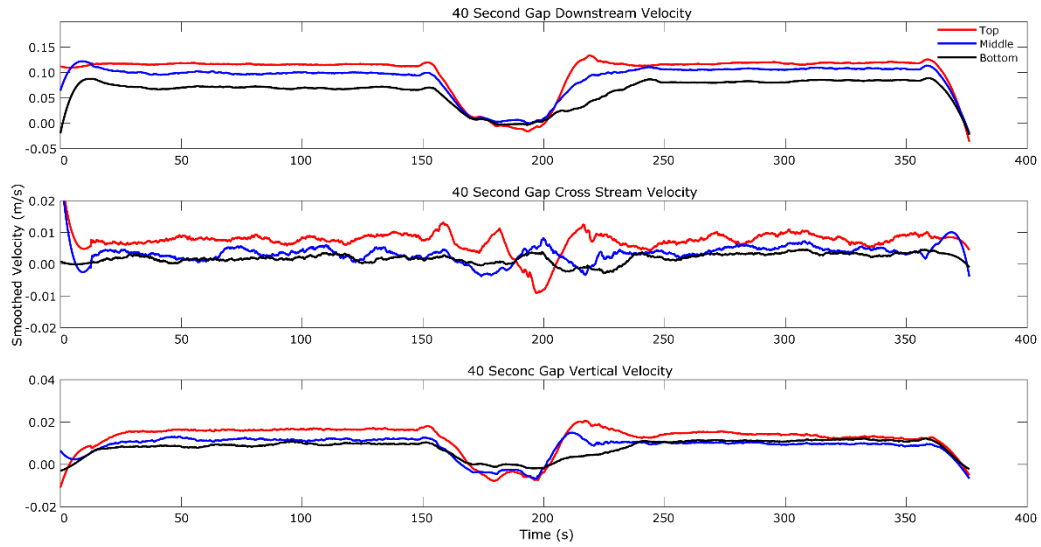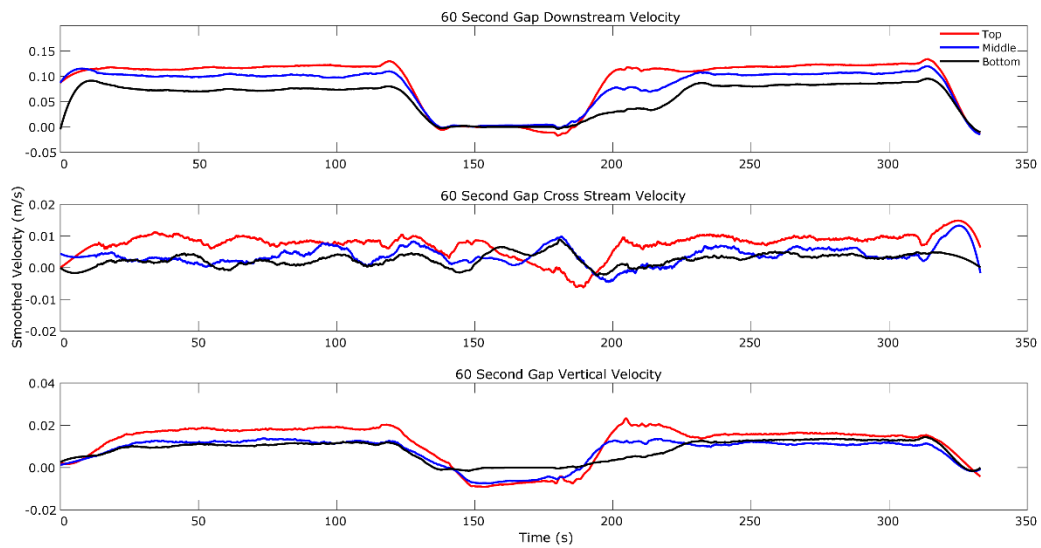
Fig. 24

Fig. 18-24. Velocity v. time for the hot water currents, the turbidity currents, the 10, 20, 30, 40, and 60 second time gap experiments. The top graph for each is the downstream velocity, the middle graph is the cross stream velocity, and the bottom graph is vertical velocity. The red curve in each graph is the velocity at the top of the current. The blue curve is the velocity in the middle, and the black curve is the velocity at the bottom of the current.
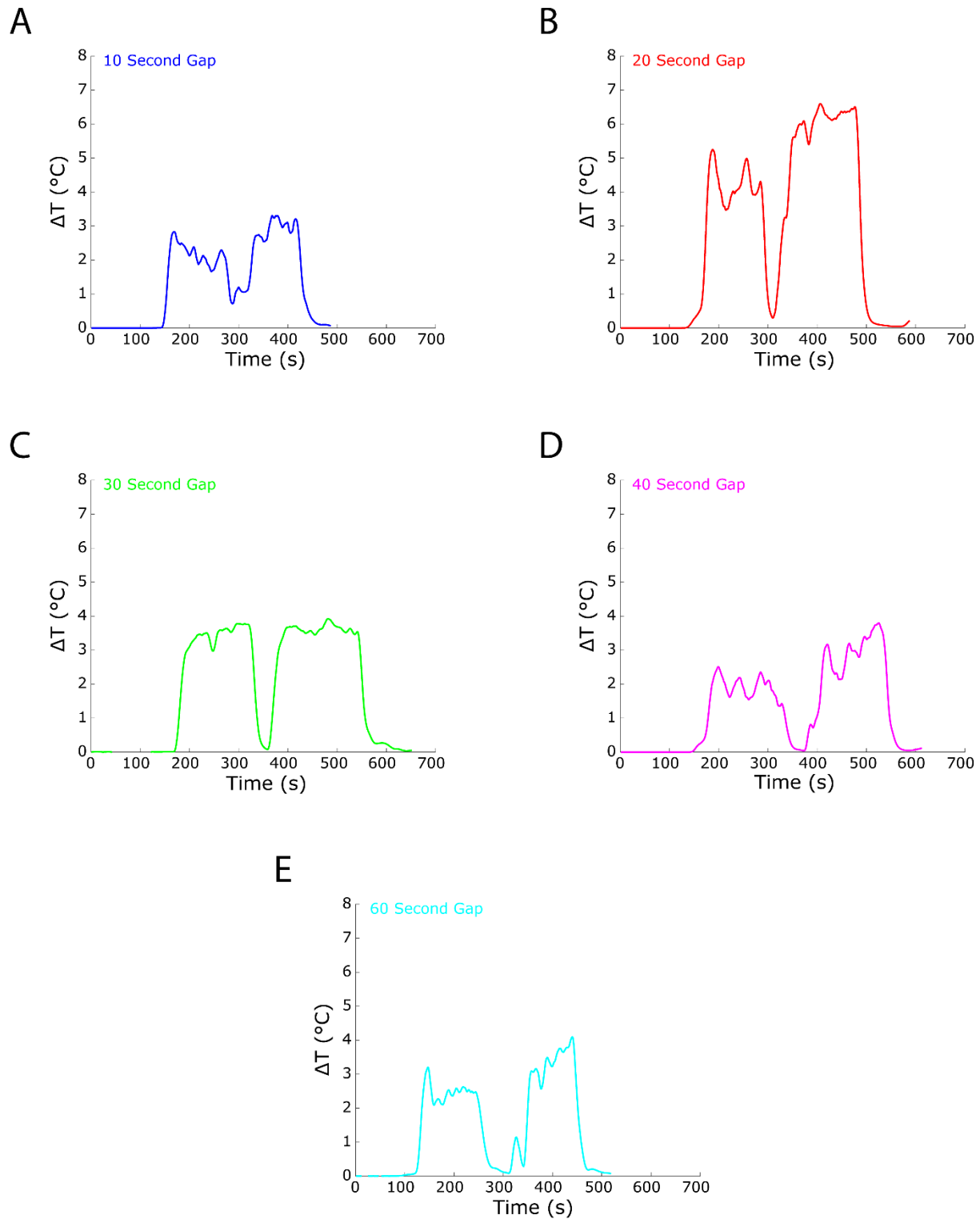
Fig. 25. Change in temperature from ambient water temperature vs time for the heated particle-laden currents, recorded 26 cm from the pipe and 6 cm above the bed. A) 10 second time gap. B) 20 second time gap. C) 30 second time gap. D) 40 second time gap. E) 60 second time gap.
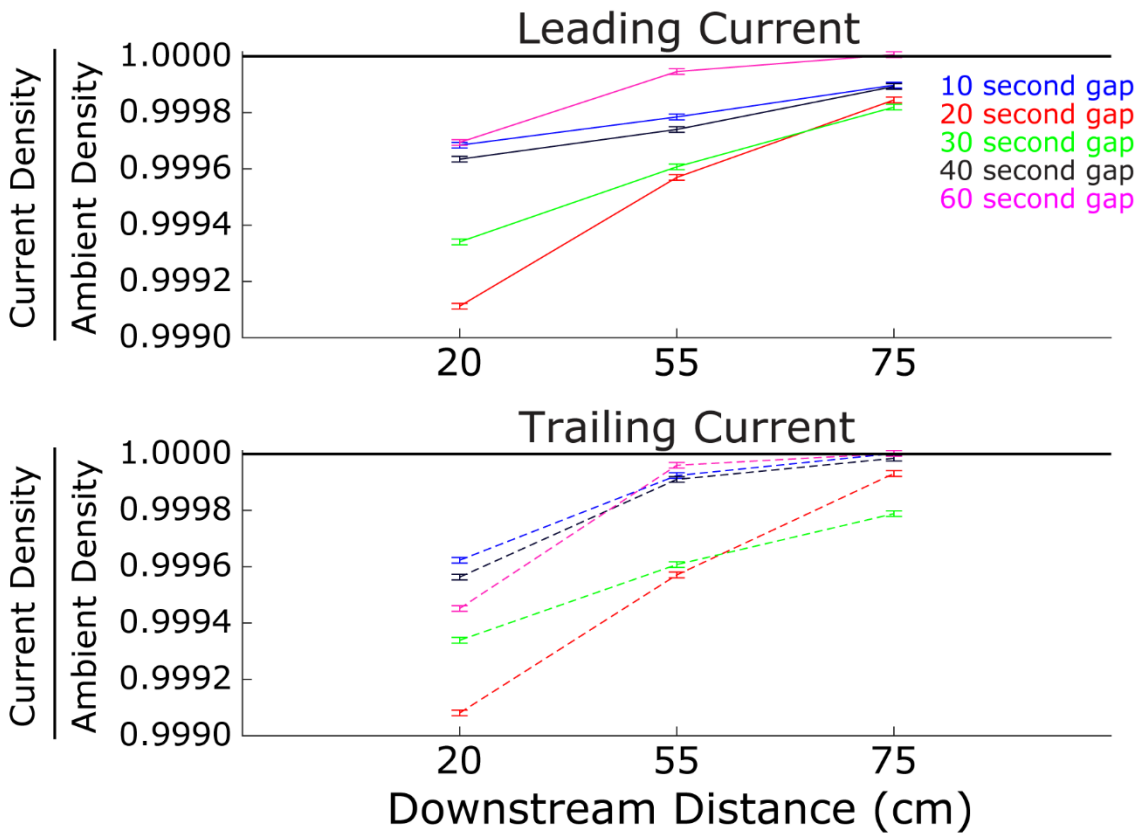
Fig. 26. Density of the current to density of water ratio with distance downstream from the pipe for all lofting experiments in water. The currents begin less dense than the water, but the forward momentum of the current prevents it from lifting off.
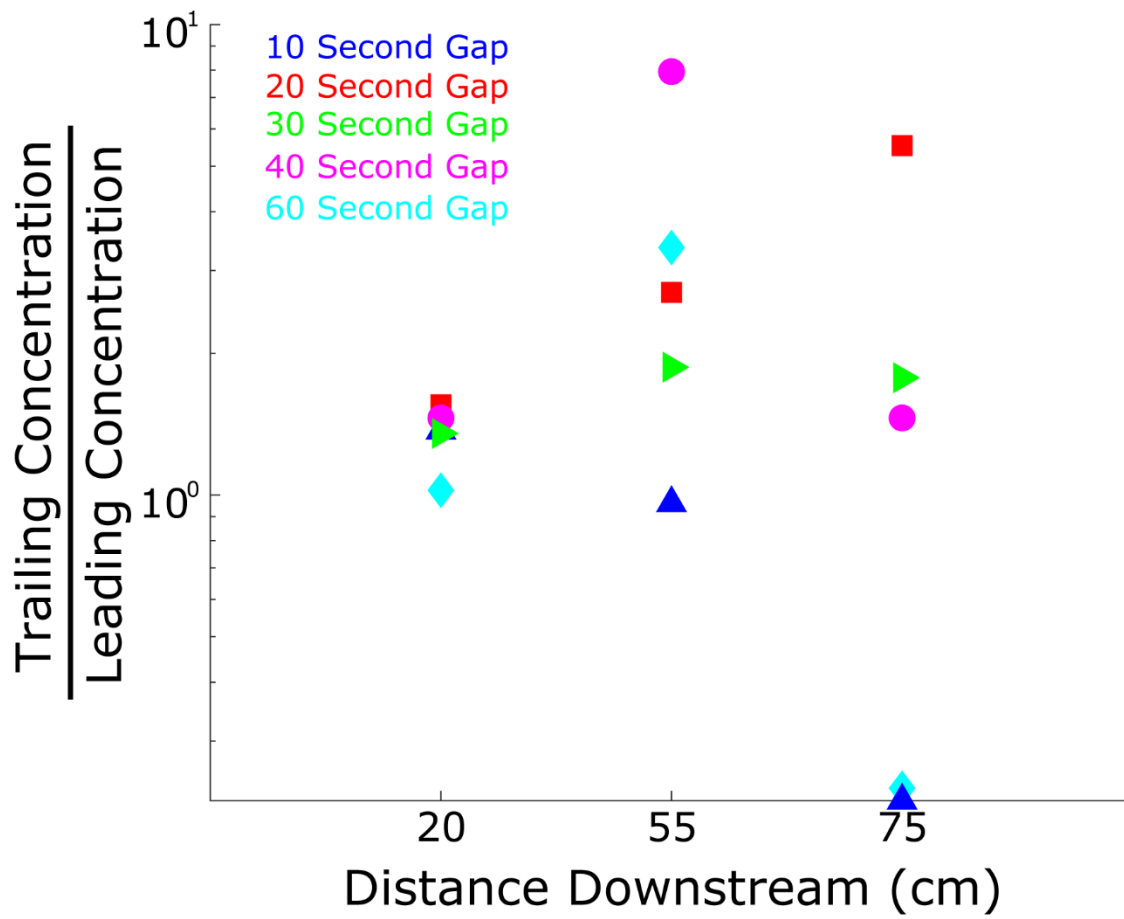
Fig. 27. The trailing current particle concentration relative to the leading current particle concentration in water, at distances from the pipe of 20, 55, and 75 cm.
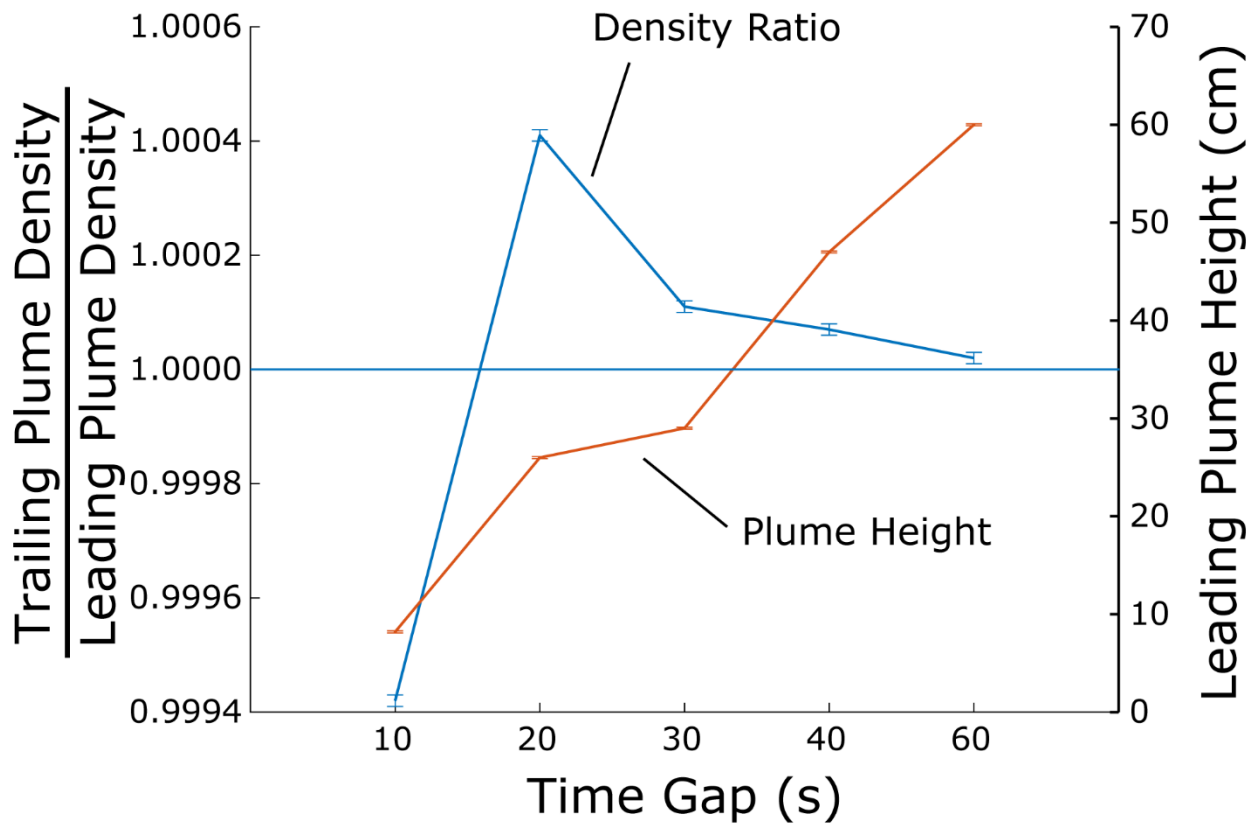
Fig. 28. The left axis is the trailing plume density relative to the leading plume density in water for all time gaps. The trailing plume is less dense than the leading plume after the 10 second time gap, and the same density as the leading plume after the 60 second time gap, allowing the plume to rise. After the 20, 30, and 40 second time gaps, the trailing plume is more dense than the leading plume, and it cannot rise. The right axis is the height above the bed the tail of the leading plume is when the trailing current enters the pool.
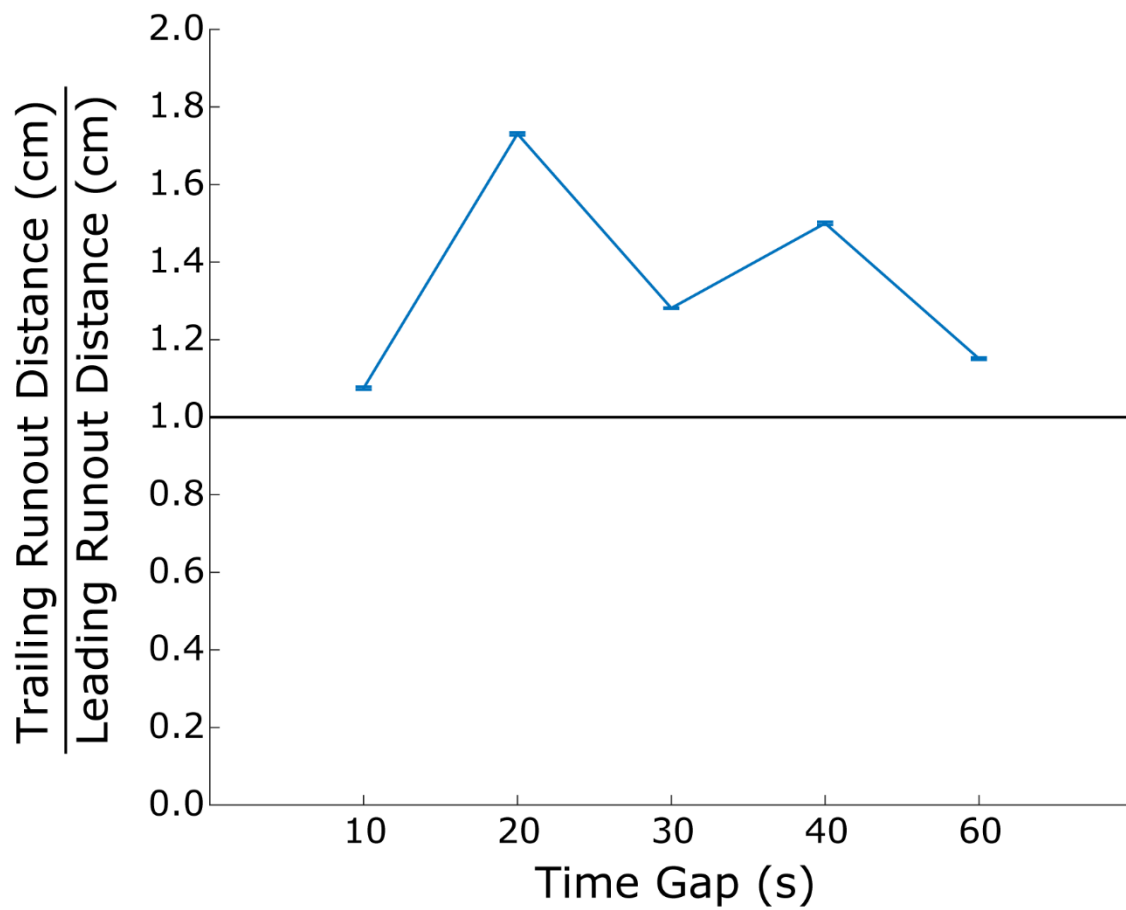
Fig. 29. The runout distance of the trailing current relative to the runout distance of the leading current in water for time gaps of 10, 20, 30, 40, and 60 seconds.

Discussion

Runout distance of density currents depends on sedimentation and entrainment in the current (Branney and Kokelaar, 2002; Bursik and Woods, 1996). Sedimentation can be inferred from the particle concentration in the currents. Because the leading and trailing current both begin flowing with the same particle concentration, any difference in sedimentation is the result of changes occurring in the pool or tank. The trailing and leading currents began with the same particle concentration. In water, because the trailing current had a greater particle concentration downstream than the leading current, sedimentation was less in the trailing currents. In contrast, sedimentation in the air experiments, the particle concentration in the leading currents is greater than the particle concentration in the trailing currents, which means more deposition occurred in the trailing currents.

Entrainment of ambient fluid in the experiments followed opposite patterns. In water, entrainment of ambient water was greater in the trailing currents after the 20, 30, and 40 second time gaps, whereas it was less or the same in the trailing currents after the 10 and 60 second time gaps. Both currents in water entered the pool less dense than the ambient water, but their densities increased with distance. The current density increased with distance because of the entrainment of colder, ambient water. Water heats up slowly because of its high heat capacity and low coefficient of thermal expansion, and thus the volume of the currents did not expand greatly from the entrainment and heating of ambient water, allowing the currents to become denser with distance. In the air experiments, entrainment caused the volume of the currents to expand greatly. Air has a very low heat capacity, and therefore heats up quickly and expands in volume. All of the leading currents in had greater entrainment than the trailing currents.

The results of the experiments in air and water match the known relationship between sedimentation and entrainment in gravity currents. An increase in entrainment corresponds to a decrease in sedimentation (Andrews and Manga, 2012; Bursik and Woods, 1996; Dufek, 2016; Saucedo et al., 2004). Higher velocities and greater currents heights decrease the Ri_B, leading to greater entrainment (Parker et al., 1987). But, higher current velocities lead to higher vertical velocities, keeping sediment in suspension and leading to slower sedimentation. Slower sedimentation sustains the density and momentum of the current, which enables it to travel further than a current in which sedimentation is rapid. In water, higher velocities and less sedimentation in the trailing currents led to a longer runout distances. In air, lower velocities and more sedimentation in the trailing currents led to shorter runout distances.

When the leading current became buoyant and lost sufficient forward momentum, it lifted-off into a rising plume that was then continuously fed by the current. Once the current ceased to flow, the plume was no longer fed from below but kept rising and spreading through the water column. When the trailing current entered the pool, the tail of the leading plume had risen to small distances above the floor after short time gaps, whereas in experiments with long time gaps the tail of the leading plume rose to large distances above the floor. When the trailing current lifted off into a rising plume, a density contrast with the leading plume was created. The trend in density difference between the leading and trailing plumes correlated with height of the leading plume above the floor. We suggest the height-density trend of the leading plume had a major effect on the observed behavior of the trailing current.

In the experiments in water, especially the experiments with 20, 30, and 40 second time gaps, when the head of the trailing plume encountered the tail of the leading plume, it could no longer rise any higher because it was denser than the leading plume. Not being able to rise

created changes in the body of the current below which allowed the trailing current to runout past the point where the leading current lifted off. These changes reflected in the velocity and particle concentration data of the trailing current. In the 10 second time gap experiment, the trailing plume was less dense than the leading plume, and could therefore keep rising, and in the 60 second time gap the plumes had near equal densities, so the trailing plume was not greatly inhibited from rising.

The inhibition of trailing plume rise in the 20, 30, and 40 second time gap experiments corresponds to a change in the velocity structure of the trailing current. The change in velocity structure occurs when the head of the trailing plume flows into the tail of the leading plume. We attribute the change in the structure of the vertical velocity to the inability of the trailing plume to rise initially through the more buoyant leading plume. The effect on the trailing plume is transferred down into the current below and suppresses the vertical velocity for a short period time, allowing the trailing current to runout farther and lift off at a greater distance. The change of the location of the highest vertical velocity in these currents has an effect on the sedimentation and the dynamics of the current. In the trailing currents with high vertical velocity, the downstream velocity is the same as the leading current, and sedimentation and entrainment does not vary from the leading current; the current loses momentum and density and reverses buoyancy after a similar runout distance (Sparks et al., 1993).

When the plume of the trailing current cannot rise, it causes the vertical velocity in the trailing current to decrease, and simultaneously the downstream velocity and the cross stream velocity begin to increase. Deposition of particles from the current decreased, creating a particle "swell" in the trailing current relative to the leading current, which then pushed out farther that the leading current before lifting off (Fig. 30).

In all experiments in air, the trailing currents had the same or shorter runout distances than the leading currents. This result we believe is also related to the plume of the leading current. Because of the lower viscosity of air, the plumes in these experiments rose faster than the plumes in water, and the volume of the plume expanded more than the plumes in water. The estimated particle concentrations of the currents show that deposition rate from the current did not decrease in the trailing current, as occurred in water. Sedimentation in the trailing current increased compared to the leading current. We believe this results from the leading plume rising fast enough to allow the trailing plume to lift off without impediment. There were no effects from the leading plume on the trailing plume that propagated down into the trailing current.

Our experiments show that main factor which can cause an increase in runout distance of the trailing current is the presence of the leading plume. When the leading plume is present and a height above the floor where its density is less than that of the trailing plume, the trailing plume cannot rise. This causes the trailing current to runout farther to a distance where its plume can rise uninhibited. When the leading plume is not present at all, or at a height where it is more dense than the trailing plume, the trailing plume rises without impact and the runout distance of the trailing current does not increase.

Implications for natural PDCs

The runout distances of PDCs in nature vary greatly, depending on many variables, including mass flux, current velocity, current density, temperature, topography, substrate, and duration that the current was fed by the volcano (Branney and Kokelaar, 2002; Druitt, 1998; Dufek and Bergantz, 2007; Nield and Woods, 2004; Wilson et al., 1995). Two nearly-identical currents with similar mass fluxes might be expected to have similar runout distances (Sulpizio et al., 2007). Our results show, however, that the leading current can impact the trailing current,

causing a change in the runout distance of the trailing current. Importantly, in some of our experiments, the leading plume inhibited the rise of the trailing plume, which in turn changed the velocity structure and increased the velocity at the top of the current. This decreased sedimentation, leading to a longer runout distance.

If a leading PDC has any effect on the dynamics trailing current, the magnitude of that effect is dependent on the rise time of the leading current plume. If the leading plume has not risen high enough, then the trailing current and leading current function as a single current, and the trailing current is not effected by the leading current in such a way that drastically changes its behavior. If the leading plume has risen too high, then when the trailing plume reaches that same height, the leading plume is dispersed enough so as to be ineffective on modifying the trailing current. For a leading current to have an evident effect on the behavior of a similar trailing current, the time spacing between the currents has to be on the same order as that of the rise rate of the leading coignimbrite column. In nature, buoyant coignimbrite plumes have rise times of about 100-200 seconds (Sparks et al., 1986; Woods, 2010; Woods and Caulfield, 1992; Woods and Kienle, 1994). During the April 1990 eruption of Mt. Redoubt, Alaska, for example, the buoyant coignimbrite column rose to a height of 12 km within 2-3 minutes (Woods and Kienle, 1994). This equates to an average rise rate of about 67 m/s, which is on the same order of the rise rate of the coignimbrite plume created by the lateral blast of Mt. St. Helens on May 18, 1980 (Sparks et al., 1986).

While not commonly observed, eruptions that produce multiple, closely spaced PDCs can and do occur, and the interaction between currents may cause changes in the trailing current which lead to it flowing over a greater distance. Of the known eruptions with closely spaced PDCs, a few are spaced within the 2-3 minute timeframe necessary for the leading current to

affect the trailing current. The 1994 and 2010 eruptions of Merapi generated multiple PDCs within seconds of each other and flowed down the same valley (Jenkins et al., 2013). Also, eruptions at Etna in 1999 and Colima in 2015 generated multiple PDCs within a period of 2-3 minutes (Behncke et al., 2003; Capra et al., 2018; Zobin, 2018). The dome collapse eruption at Soufrière Hills on Montserrat on June 25 1997, produced three sequential PDCs that were closely spaced in time, the first two of which occurred with 3 minutes of each other (S.C. Loughlin et al., 2002). This eruption provides a potential example where interaction between currents may have occurred. The first current flowed down the steep-walled Mosquito Ghaut on the flank of the volcano, travelling a total of 4.7 km in 310 seconds at an average velocity of 15 m/s. The second current was generated 165 seconds after the first current, and also flowed down Mosquito Ghaut. This current travelled 4.7 km in 233 seconds at an average velocity of 20.2 m/s, and then slowed down but continued flowing for another 2 km. The second current reached the runout distance of the first current 88 seconds after the first one stopped flowing. If a plume was produced by the first current, it would have still been rising when the second current reached 4.7 km, and provided the conditions necessary for the trailing current to run out to a greater distance. The second current did continue flowing to 6.8 km, although its average velocity was much higher than the first current's, but the conditions were right for the first current to impact the second.
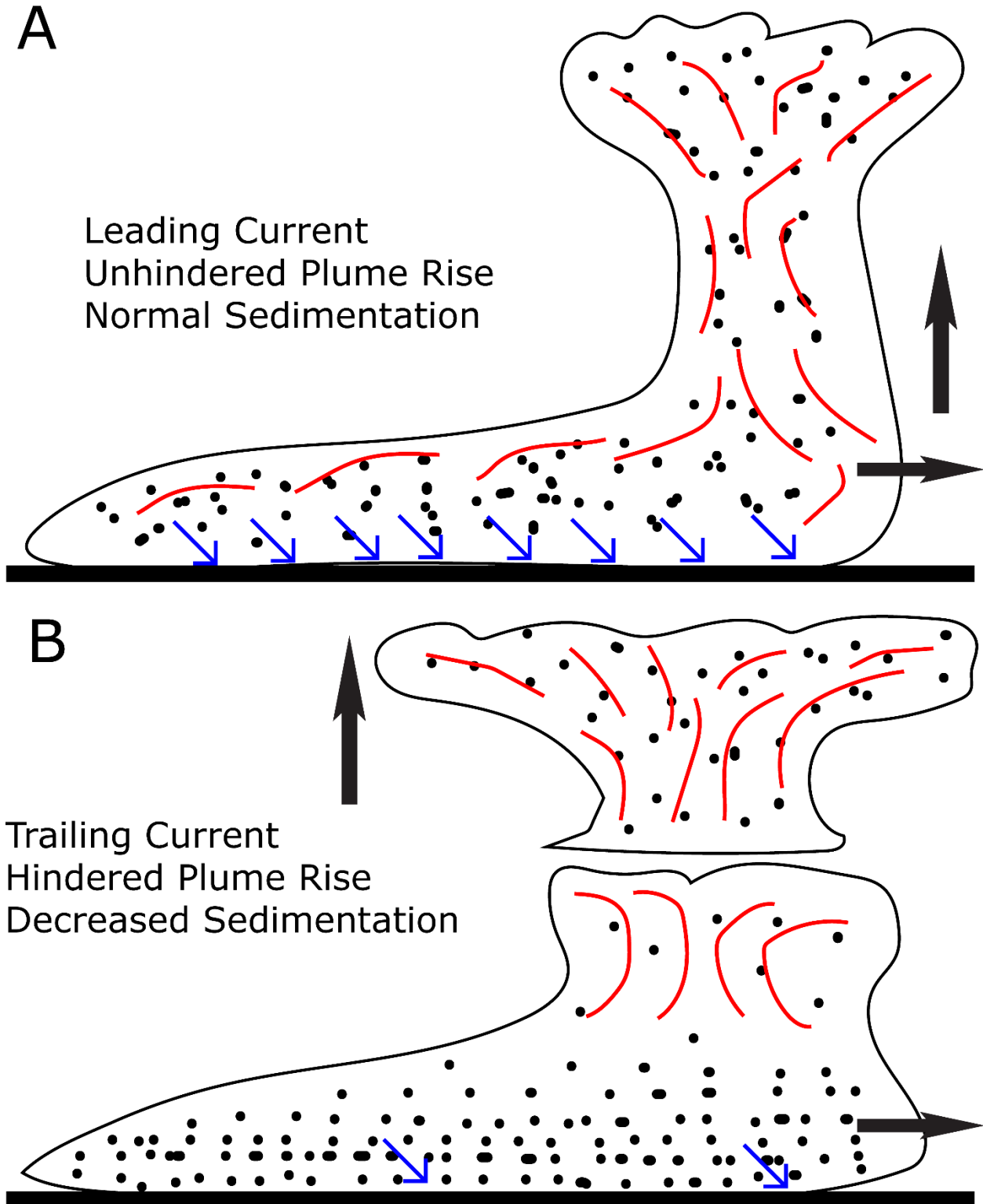
Fig. 30. A) Model for the leading current with uninhibited plume rise. B) Model for the trailing current where plume rise is inhibited by the leading plume. The current cannot rise and therefore has to continue flowing downstream.

51

Conclusions

Multiple pyroclastic density currents can occur during the same during the same eruption at time intervals that make it possible for one current to flow into another current in front of it. If the currents have a similar volume, mass flux, and velocity, then the leading current can have an impact on the trailing current. The leading current flows through the ambient atmosphere around the volcano, but modifies the ambient surroundings which the trailing current then flows into. When the trailing current flows into the modified surroundings, the dynamics and behavior of the current may also change. The experimental methods used to examine the interaction between a leading current and trailing current showed that, under certain circumstances, the behavior of the trailing current changed and its runout distance increased relative to the runout distance of the leading current.

The scale of the increase in runout distance is dependent on the size of the time gap between the leading and trailing current and rise rate of the leading current plume. The leading current reverses buoyancy and lifts off into a rising plume and rises through the ambient fluid. The size of the time gap between it and the trailing current determines the height in the ambient fluid to which the leading plume rises before the trailing current flows into it. At certain heights, the leading plume inhibits the rise of the trailing plume because it has a lower density than the trailing plume. This causes particles and the momentum of the trailing current to continue flowing downstream instead of up and into the plume, increasing the velocity of the current. The sedimentation rate of particles from the current decreases, allowing the trailing current to runout farther than the leading current. The magnitude of change depends on the rise time of the leading plume, which in natural PDCs is generally 2-3 minutes. Any time gap between currents

greater than this, and the effect on the trailing current will be miniscule to nonexistent, and the runout distance of the trailing current will not increase relative to the leading current.

Appendix

Water Experiments

| Date	Experiment	Concentration (vol %)	Duration (min:sec)	Tank Temp (°C)	Pool Temp (°C)	Time Gap (min:sec)
2/23/2017	1	0.02	17:40	40	18	-
2/28/2017	2	0.02	12:00	40	18	-
3/3/2017	3	0.01	7:52	45	18	-
3/7/2017	4	0.01	9:07	35	18	-
3/9/2017	5	0.01	11:17	40	18	-
3/10/2017	6	0.015	14:56	25	18	-
3/14/2017	7	0.015	17:51	28	18	-
3/15/2017	8	0.015	20:21	28	18	-
3/17/2017	9	0	11:34	28	18	-
3/23/2017	10	0	10:07	28	18	-
3/28/2017	11	0	9:38	29	19	0:20
3/30/2017	12	0.015	7:08	28	20	0:20
4/6/2017	13	0.015	7:20	28	20	0:20
4/11/2017	14	0.015	4:10	28	20	0:10
4/11/2017	15	0.015	5:30	28	20	0:20
4/14/2017	16	0.015	5:35	28	20	0:20
4/25/2017	17	0.015	5:20	28	20	0:20
4/27/2017	18	0.015	5:25	28	20	1:00
5/2/2017	19	0.015	4:40	27	20	0:10
5/4/2017	20	0.015	6:00	28	20	0:40
5/9/2017	21	0.015	6:00	21	21	0:20
5/11/2017	22	0.015	6:20	29	22	0:30
12/6/2017	23	0.015	12:00	28	21	-
12/8/2017	24	0.015	9:15	28	21	-
12/11/2017	25	0.015	6:35	28	21	0:20
1/9/2018	26	0.015	5:37	28	21	0:10
1/11/2018	27	0.015	8:03	21	21	0:20

Table 3. Every experiment performed in water. Many of the experiments were setup experiments, and did not give usable data.
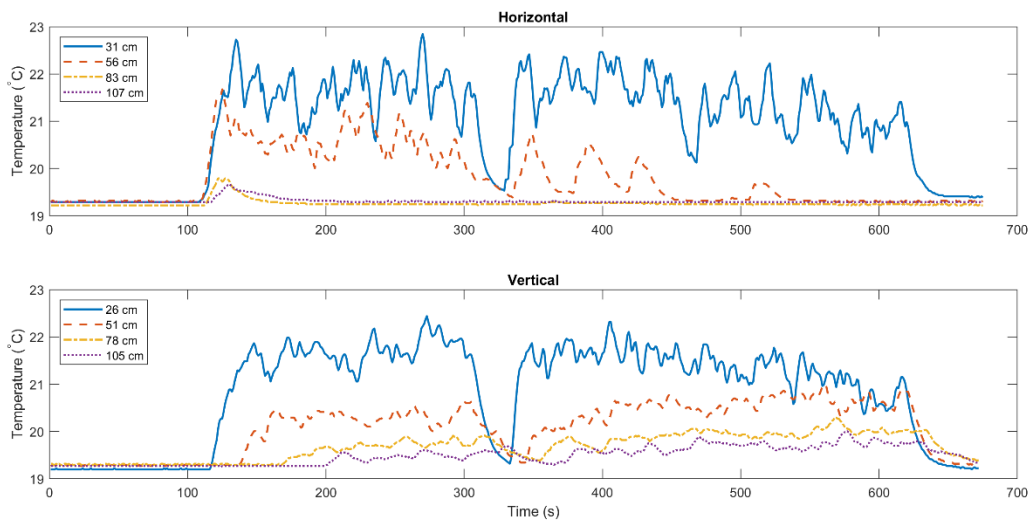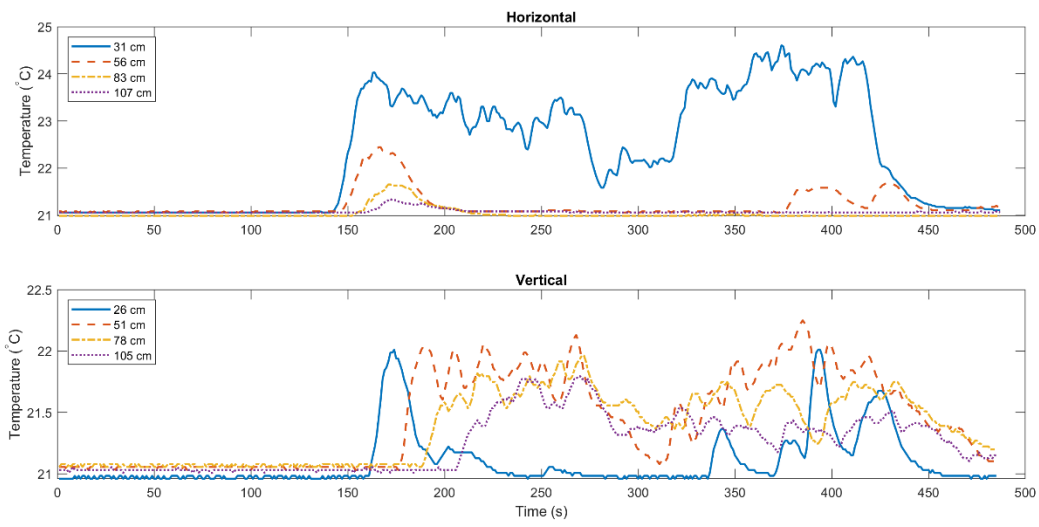
Fig. 31. Temperature data for water experiment 11: hot water with a 20 second time gap. The top graph shows the temperature recorded by the thermistors arranged horizontally along the bed against time. The four thermistors were positions 3 cm above the bed, and 31, 56, 83, and 107 from the pipe. The bottom graph the temperature recorded by the thermistors arranged vertically against time. The four thermistors were position 74 cm from the pipe, and 26, 51, 78, and 105 cm above the bed. The positions of the thermistors are the same for all the following graphs of temperature vs. time in the water experiments.
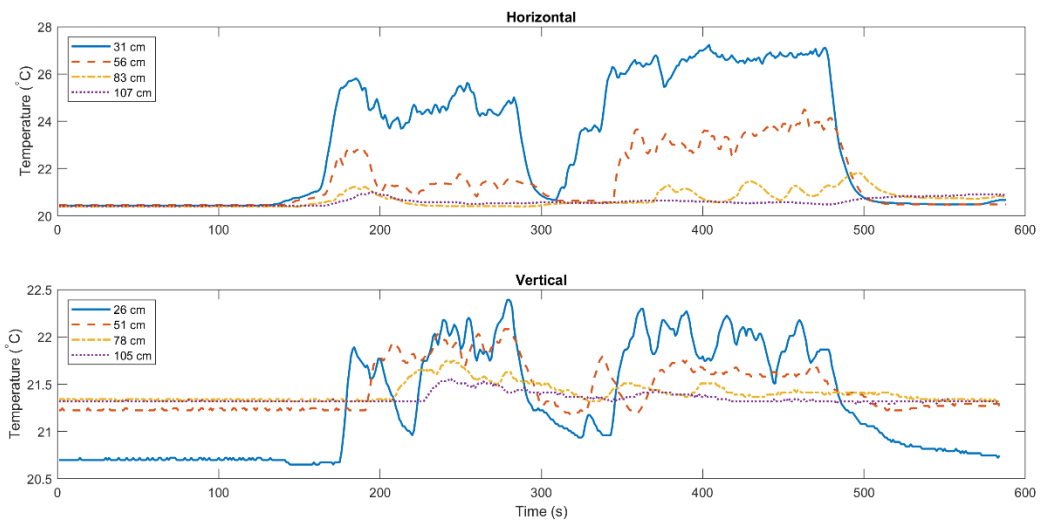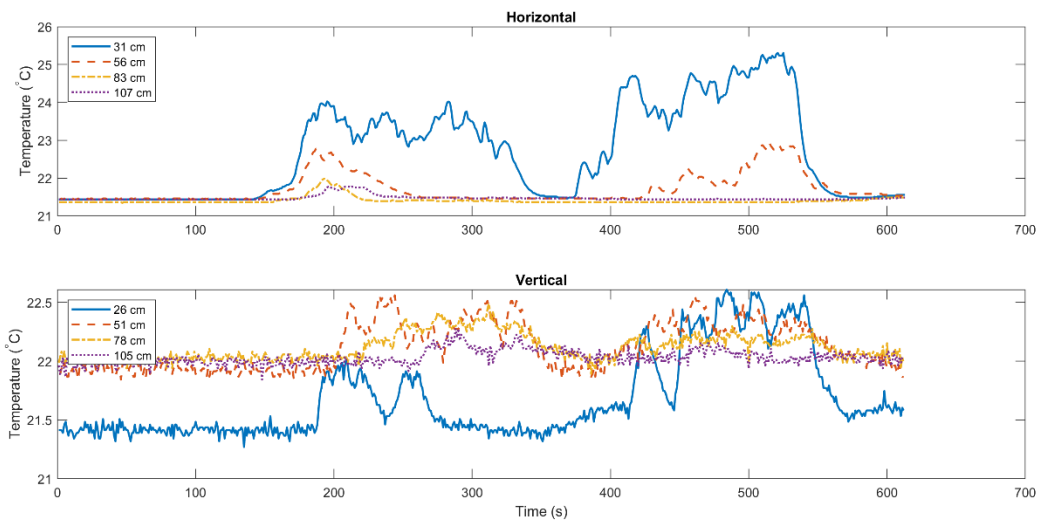
Fig. 32. Temperature data for water experiment 17: lofting current with a 20 second time gap.
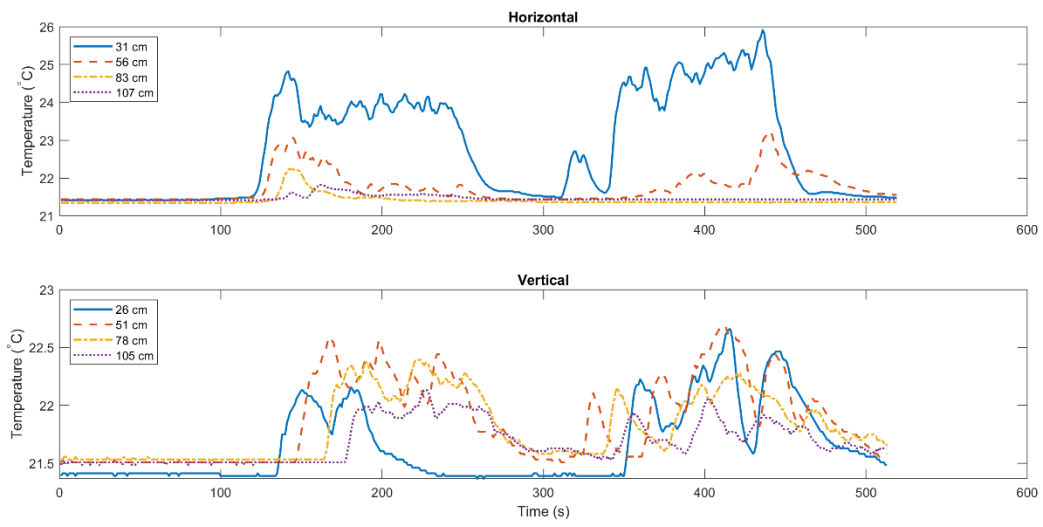
Fig. 33. Temperature data for water experiment 18: lofting current with a 60 second time gap.

Fig. 34. Temperature data for water experiment 19: lofting current with a 10 second time gap.

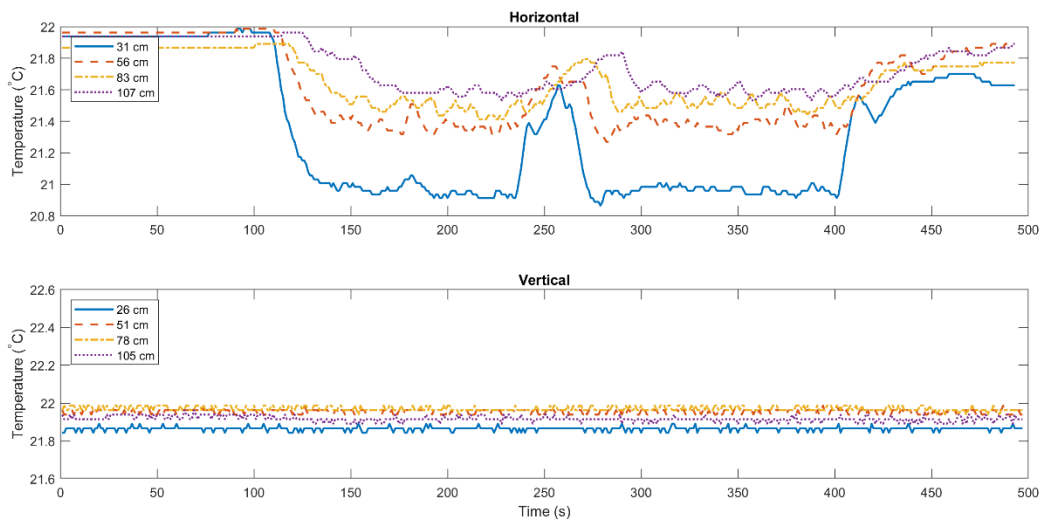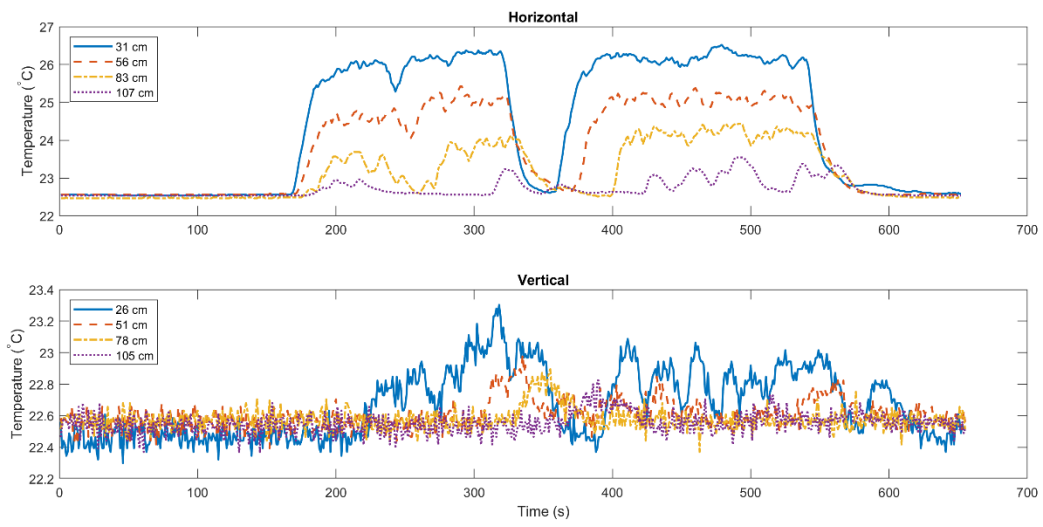**Fig. 35.** Temperature data for water experiment 20: lofting current with a 40 second time gap.

Fig. 36. Temperature data for water experiment 21: turbidity current with a 20 second time gap.

Fig. 37. Temperature data for water experiment 22: lofting current with a 30 second time gap.

Lead							
X	Z	Sed+Paper (g)	Paper (g)	Sediment (g)	Water (g)	Sediment+Water (g)	Concentration (Mass %)
20	6	0.9195	0.4621	0.4574	162.29	162.75	0.2810
54	6	0.5964	0.4501	0.1463	191.89	192.04	0.0762
76	6	0.487	0.4663	0.0207	188.71	188.73	0.0110
74	17	0.5059	0.4638	0.0421	162.3	162.34	0.0259
Trail							
X	Z	Sed+Paper (g)	Paper (g)	Sediment (g)	Water (g)	Sediment+Water (g)	Concentration (Mass %)
20	6	1.1698	0.4776	0.6922	157.65	158.34	0.4372
54	6	0.8615	0.4539	0.4076	197.89	198.30	0.2055
76	6	0.5691	0.4545	0.1146	188.22	188.33	0.0608
74	17	0.5904	0.4598	0.1306	135.62	135.75	0.0962

Table 4. Particle concentration data calculated from siphon data for experiment 17. X is downstream distance from the pipe, Z is vertical distance above the bed. The table shows mass of the sediment plus filter paper, mass of the paper alone, mass of the sediment alone, mass of the water collected by the siphon, and the concentration of the current at the specific siphon in mass %. The same calculations are the repeated for all the following experiments.

Lead							
X	Z	Sed+Paper (g)	Paper (g)	Sediment (g)	Water (g)	Sediment+Water (g)	Concentration (Mass %)
20	6	0.8159	0.4627	0.3532	158.46	158.81	0.2224
54	6	0.4905	0.4538	0.0367	182.53	182.57	0.0201
76	6	0.4728	0.4651	0.0077	184.5	184.51	0.0042
74	17	0.4807	0.4614	0.0193	133.16	133.18	0.0145
Trail							
X	Z	Sed+Paper (g)	Paper (g)	Sediment (g)	Water (g)	Sediment+Water (g)	Concentration (Mass %)
20	6	0.8735	0.4683	0.4052	177.51	177.92	0.2277
54	6	0.599	0.4605	0.1385	204.93	205.07	0.0675
76	6	0.4512	0.4493	0.0019	192.88	192.88	0.0010
74	17	0.4899	0.4478	0.0421	135.76	135.80	0.0310

Table 5. Particle concentration data calculated from siphon data for experiment 18.

Lead							
X	Z	Sed+Paper (g)	Paper (g)	Sediment (g)	Water (g)	Sediment+Water (g)	Concentration (Mass %)
20	6	0.7291	0.4515	0.2776	155.83	156.11	0.1778
54	6	0.5117	0.4653	0.0464	178.76	178.81	0.0259
76	6	0.4674	0.4567	0.0107	183.27	183.28	0.0058
74	17	0.4576	0.4456	0.012	127.02	127.03	0.0094
Trail							
X	Z	Sed+Paper (g)	Paper (g)	Sediment (g)	Water (g)	Sediment+Water (g)	Concentration (Mass %)
20	6	0.7952	0.4532	0.342	139.94	140.28	0.2438
54	6	0.5118	0.4634	0.0484	194.72	194.77	0.0249
76	6	0.4478	0.4454	0.0024	186.89	186.89	0.0013
74	17	0.4738	0.4453	0.0285	128.66	128.69	0.0221

Table 6. Particle concentration data calculated from siphon data for experiment 19.

Lead							
X	Z	Sed+Paper (g)	Paper (g)	Sediment (g)	Water (g)	Sediment+Water (g)	Concentration (Mass %)
20	6	0.7642	0.4658	0.2984	167.6	167.90	0.1777
54	6	0.4773	0.4623	0.015	173.59	173.61	0.0086
76	6	0.4565	0.4522	0.0043	179.01	179.01	0.0024
74	17	0.4624	0.4584	0.004	131.67	131.67	0.0030
Trail							
X	Z	Sed+Paper (g)	Paper (g)	Sediment (g)	Water (g)	Sediment+Water (g)	Concentration (Mass %)
20	6	0.8391	0.4565	0.3826	147.27	147.65	0.2591
54	6	0.5917	0.4568	0.1349	197.31	197.44	0.0683
76	6	0.4627	0.4562	0.0065	185.16	185.17	0.0035
74	17	0.4639	0.4566	0.0073	127.24	127.25	0.0057

Table 7. Particle concentration data calculated from siphon data for experiment 20.

Lead							
X	Z	Sed+Paper (g)	Paper (g)	Sediment (g)	Water (g)	Sediment+Water (g)	Concentration (Mass %)
20	6	0.7163	0.4634	0.2529	150.84	151.09	0.1674
54	6	0.6961	0.4533	0.2428	216.49	216.73	0.1120
76	6	0.6059	0.4528	0.1531	185.54	185.69	0.0824
74	17	0.5353	0.4618	0.0735	131.31	131.38	0.0559
Trail							
X	Z	Sed+Paper (g)	Paper (g)	Sediment (g)	Water (g)	Sediment+Water (g)	Concentration (Mass %)
20	6	0.7754	0.4591	0.3163	139.48	139.80	0.2263
54	6	0.8453	0.4504	0.3949	188.2	188.59	0.2094
76	6	0.7283	0.4587	0.2696	184.05	184.32	0.1463
74	17	0.5197	0.4518	0.0679	126.62	126.69	0.0536

Table 8. Particle concentration data calculated from siphon data for experiment 22.
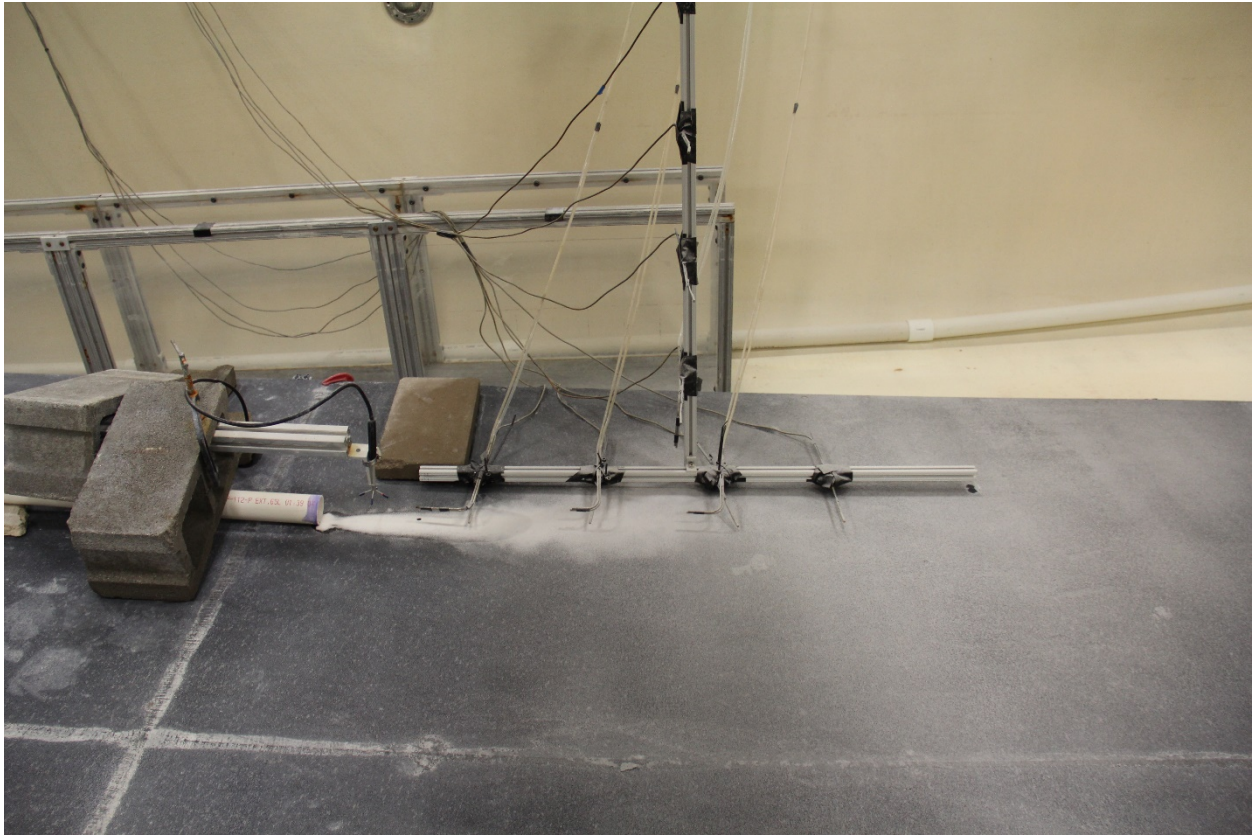
Fig. 38. Photograph of deposit for experiment 17. The current deposit is on the left close the pipe. The length/width ratio is large. The particles deposited on the right are the fall from the lofting plume. This is the case for all the lofting experiments.
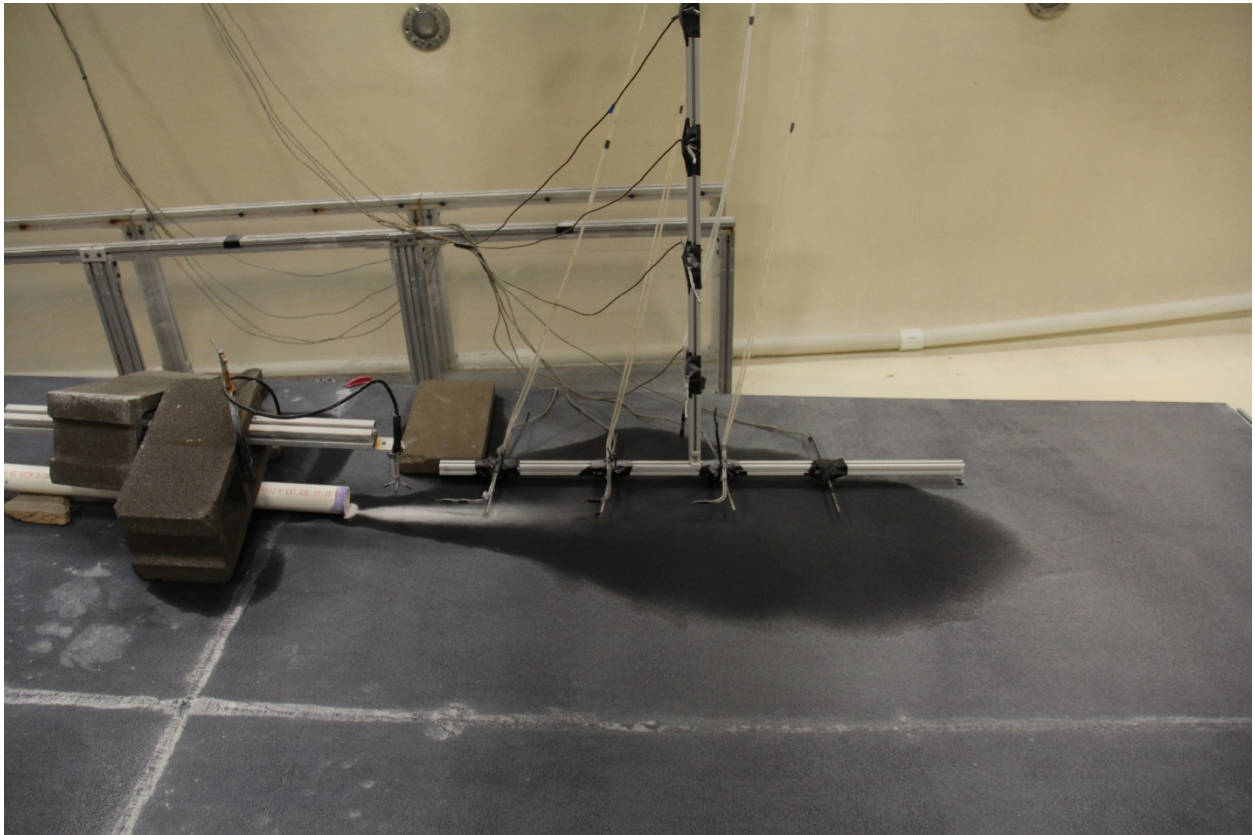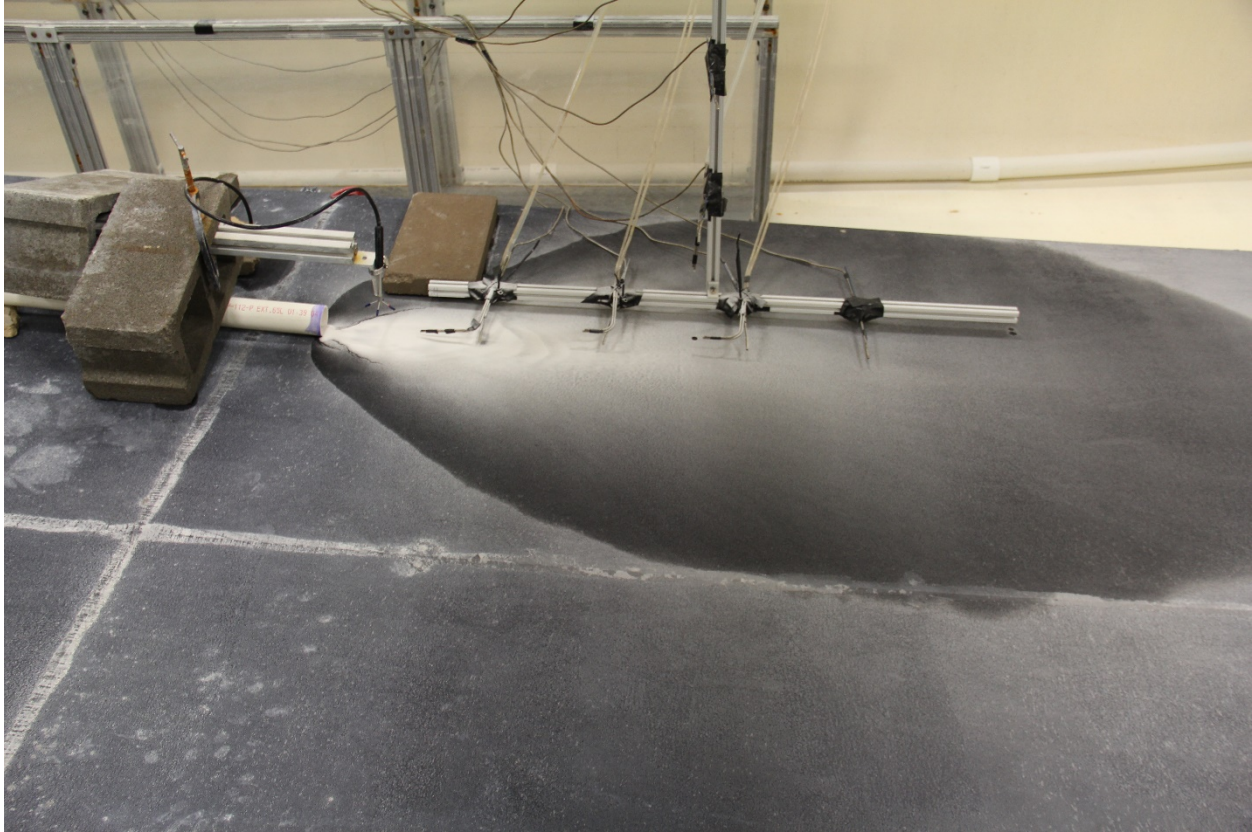
Fig. 39. Photograph of deposit for experiment 18.

Fig. 40. Photograph of deposit for experiment 19.

Fig. 41. Photograph of deposit for experiment 20.

Fig. 42. Photograph of deposit for experiment 21. This is the deposit from the turbidity current. The length/width ratio is smaller than the lofting currents because the current spreads out and does not rise. There is also not any particle fall deposit at the end of the bed.

**Fig. 43.** Photograph of deposit for experiment 22.

| Experiment	Date	Time	Temperature (F)		Initial Mass (g)	Dead Mass (g)	Current Mass (g)	Time In	Time Out	Belt (cm)	Velocity (cm/s)	Time Gap	Feed Duration (s)	Current Rate (g/s)
20170105_01	1/5/2017	1:09 PM	200		1000.8	925.2	75.6	12:10 PM	1:09 PM	100	3.25	Continuous	30.77	2.46
20170105_02	1/5/2017	1:38 PM	200		497.8	467.3	30.5	1:09 PM	1:38 PM	100	3.25	Continuous	30.77	0.99
20170105_03	1/5/2017	2:01 PM	-		502.5	479.4	23.1	2:01 PM	-	100	3.25	Continuous	30.77	0.75
20170109_01	1/9/2017	11:45 AM	250		500.7	-	-	11:16 AM	11:45 AM	100	3.25	Continuous	30.77	-
20170109_02	1/9/2017	12:20 PM	250		499.7	456.7	43	11:23 AM	12:20 PM	100	3.25	Continuous	30.77	1.40
20170109_03	1/9/2017	1:26 PM	250		500.8	467.2	33.6	11:54 AM	1:26 PM	100	3.25	Continuous	30.77	1.09
20170109_04	1/9/2017	2:26 PM	250	Current 1	500	463.25	36.75	1:46 PM	2:26 PM	30	1	30_30_30	30.00	0.61
				Current 2	500	463.25	36.75			30	1			
20170109_05	1/9/2017	3:03 PM	250	Current 1	500.1	461.25	38.85	2:26 PM	3:03 PM	30	1	30_60_30	30.00	0.65
				Current 2	500.1	462.45	37.55			30	1			
20170110_01	1/10/2017	12:00 PM	250	Current 1	500	462.45	37.55	10:33 AM	12:00 PM	30	1	30_10_30	30.00	0.63
				Current 2	500	472.55	27.45			30	1			
20170110_02	1/10/2017	12:46 PM	250	Current 1	500	472.55	27.45	12:00 PM	12:46 PM	30	1	30_10_30	30.00	0.46
				Current 2	500	472.55	27.45			30	1			
20170110_03	1/10/2017	1:38 PM	250	Current 2	1000	918	82	12:46 PM	1:38 PM	60	1	Continuous	60.00	1.37
20170110_04	1/10/2017	2:17 PM	200	Current 1	500	478.9	21.1	1:38 PM	2:17 PM	30	1	30_30_30	30.00	0.35
				Current 2	500	478.9	21.1			30	1			
20170110_05	1/10/2017	2:50 PM	200	Current 1	500	467.05	32.95	2:17 PM	2:50 PM	30	1	30_10_30	30.00	0.55
				Current 2	500	467.05	32.95			30	1			
20170110_06	1/10/2017	3:20 PM	200	Current 1	500	461.1	38.9	2:50 PM	3:20 PM	30	1	30_5_30	30.00	0.65
				Current 2	500	461.1	38.9			30	1			
20170112_01	1/12/2017	10:15 AM	200	Current 1	500	466.15	33.85	9:45 AM	10:15 AM	30	1	30_5_30	30.00	0.56
				Current 2	500	466.15	33.85			30	1			
20170112_02	1/12/2017	10:40 AM	-	Current 1	500	478.3	21.7	-	-	30	1	30_5_30	30.00	0.36
				Current 2	500	478.3	21.7			30	1			
20170112_03	1/12/2017	11:05 AM	-	Current 1	500	479.95	20.05	-	-	30	1	30_10_30	30.00	0.33
				Current 2	500	479.95	20.05			30	1			
20170112_04	1/12/2017	11:56 AM	-	Current 1	500	472.75	27.25	-	-	30	1	30_30_30	30.00	0.45
				Current 2	500	472.75	27.25			30	1			
20170112_05	1/12/2017	12:10 PM	-		1000	962.5	37.5	-	-	60	1	Continuous	60.00	0.62
20170113_01	1/13/2017	10:33 AM	250	Current 1	500.1	468.3	31.8	9:55 AM	10:33 AM	30	1	30_5_30	30.00	0.53
				Current 2	500.1	468.3	31.8			30	1			
20170113_02	1/13/2017	11:05 AM	200	Current 1	500	470.7	29.4	10:33 AM	11:05 AM	30	1	30_5_30	30.00	0.49
				Current 2	500	470.7	29.3			30	1			
20170113_03	1/13/2017	11:50 AM	200	Current 1	500	473.55	26.45	11:05 AM	11:50 AM	30	1	30_10_30	30.00	0.44
				Current 2	500	473.55	26.45			30	1			

Table 9. Every experiment performed in air. Many of the experiments were setup experiments, and did not give usable data.
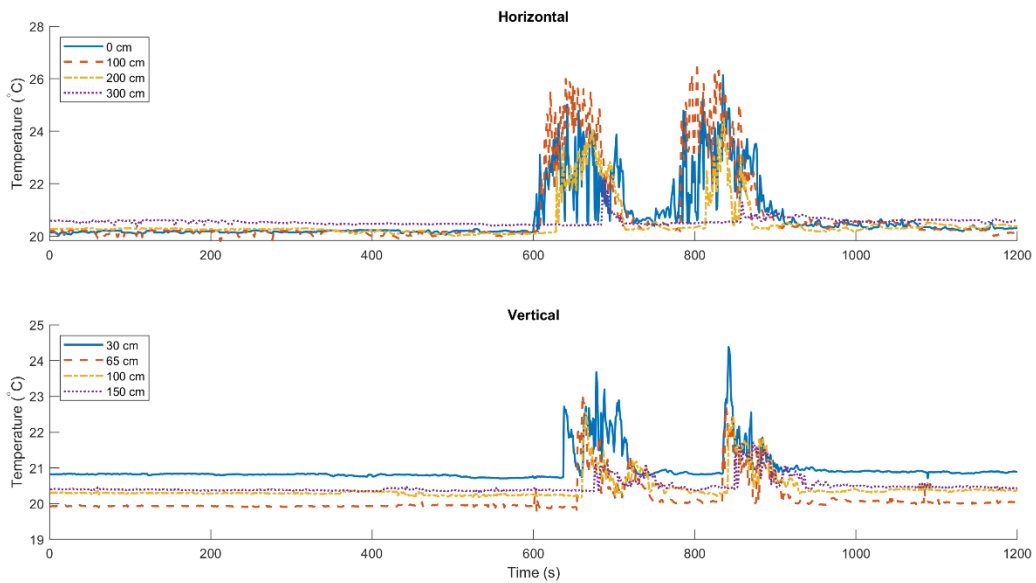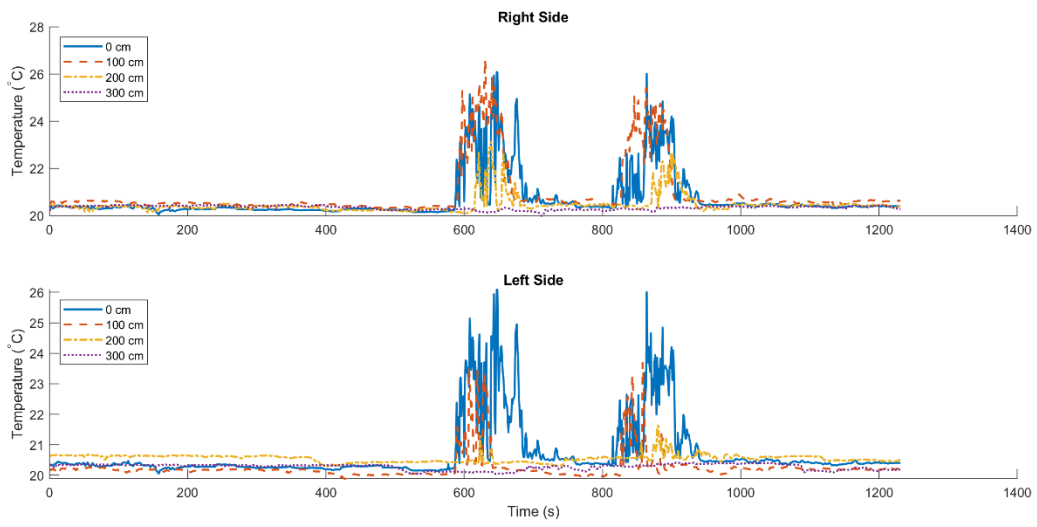
Fig. 44. Temperature data against time recorded by thermocouples for air experiment 20170109_04. The top graph is the temperature recorded by thermocouples positioned horizontally downstream from the chute. The positions are in the chute, and 100, 200, and 300 cm downstream, all at 5 cm above the floor. The bottom graph is the temperature recorded by thermocouples positioned vertically. All thermocouples are positioned 250 cm downstream, at heights of 30, 65, 100, and 150 cm above the bed. All positions are the same for the following graphs.
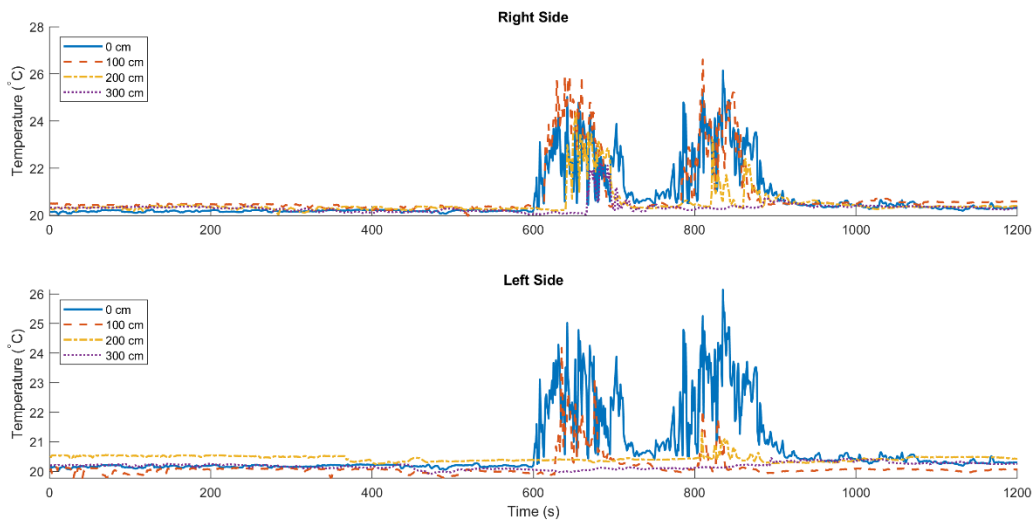
Fig. 45. Temperature data against time recorded by thermocouples for air experiment 20170109_04. The top graph is the temperature recorded by thermocouples positioned horizontally downstream from the chute, 50 cm to the right of the centerline. The bottom graph is the temperature recorded by thermocouples positioned 50 cm to the left of the centerline. The downstream positions are 100, 200, and 300 cm from the chute. All positions are the same for the following graphs.
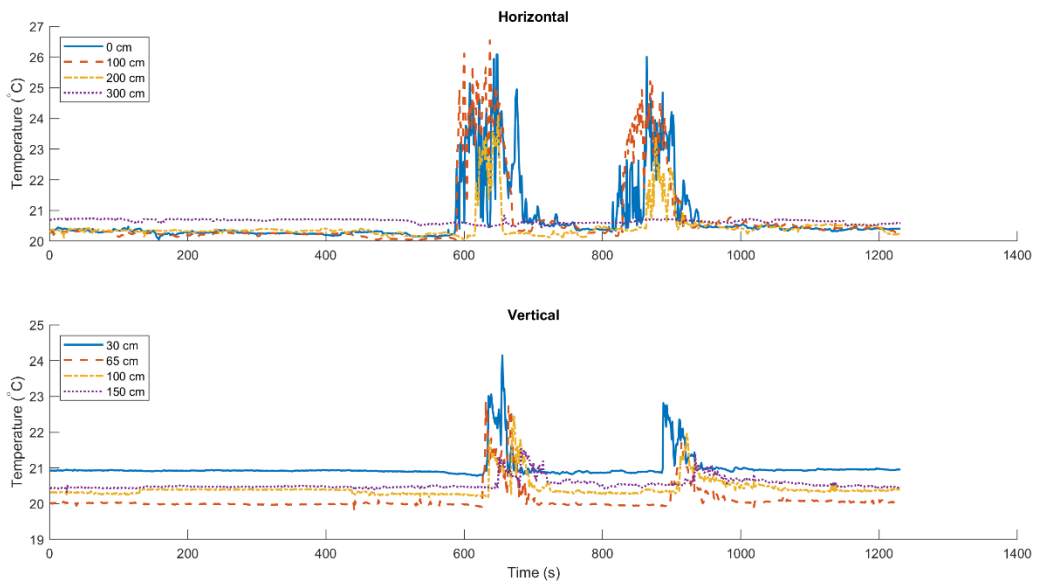
Fig. 46. Temperature data against time recorded by centerline thermocouples for air experiment 20170109_05.
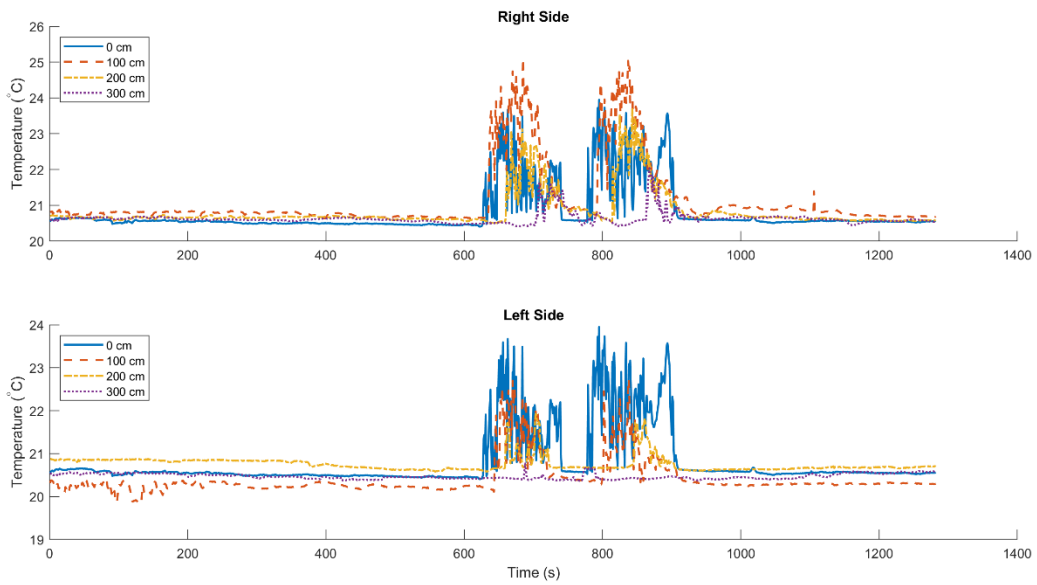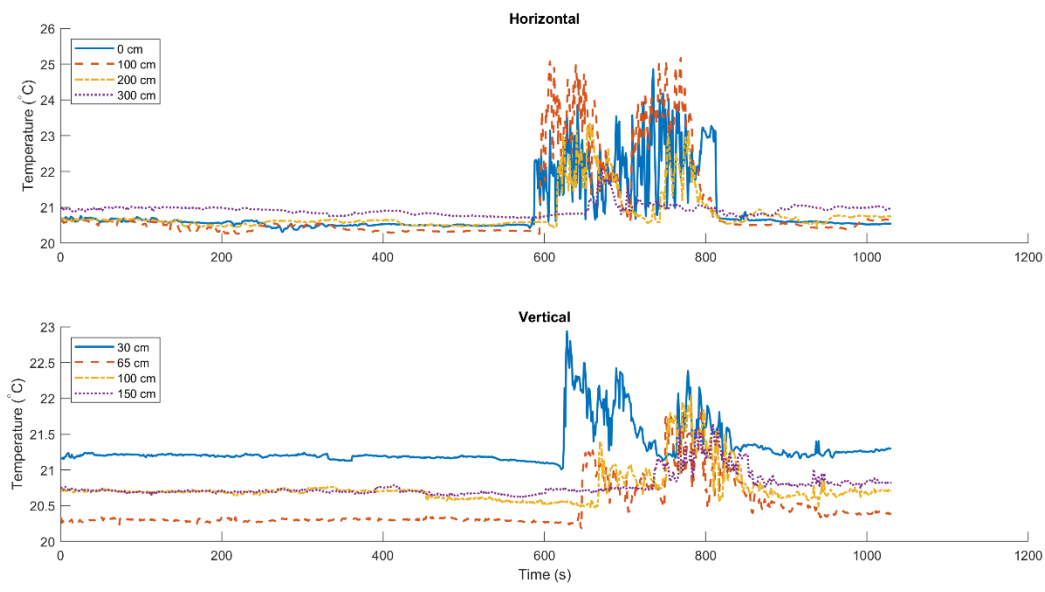
Fig. 47. Temperature data against time recorded by offset thermocouples for air experiment 20170109_05.
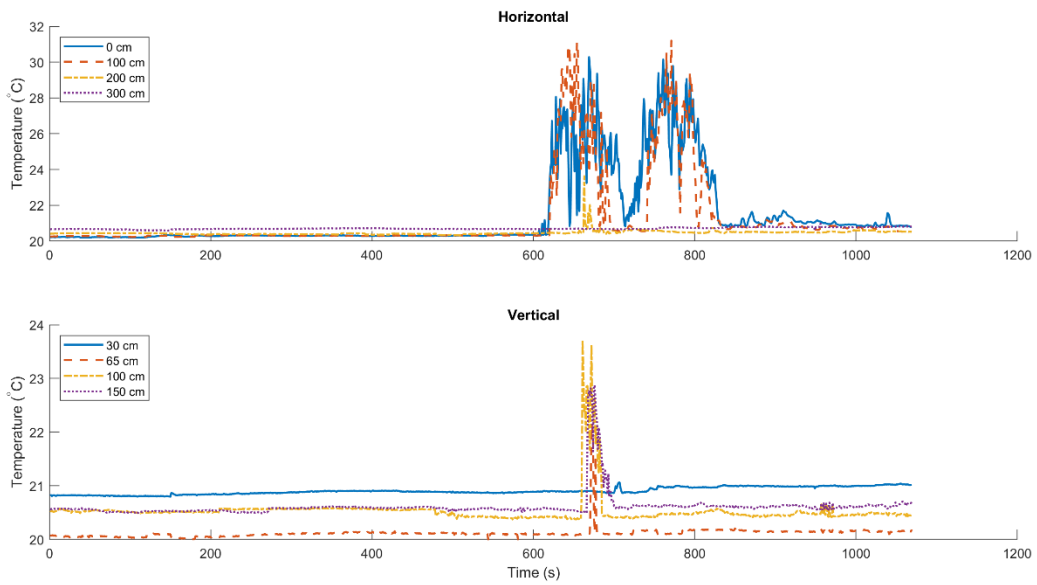
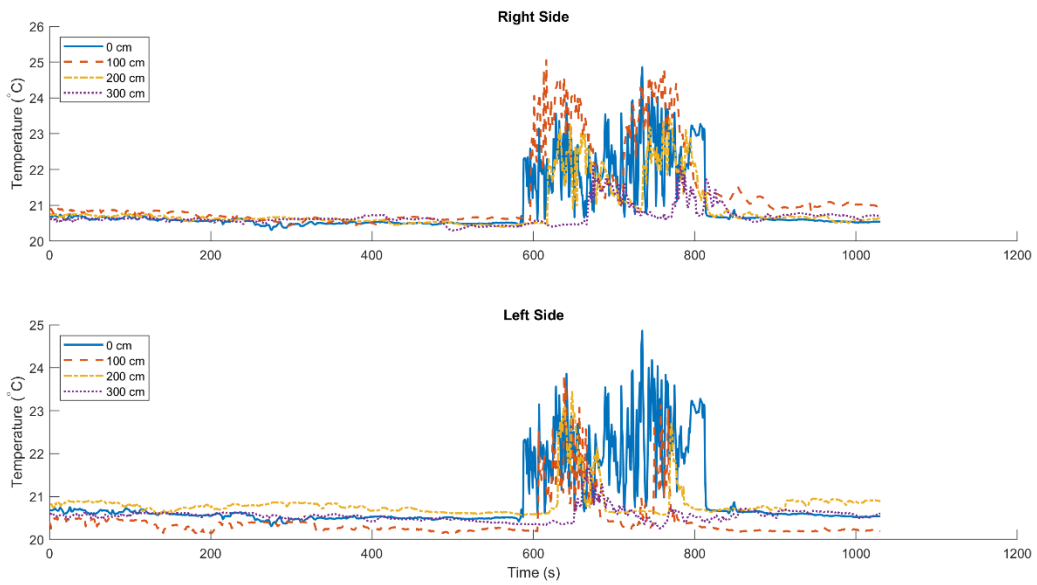**Fig. 48.** Temperature data against time recorded by centerline thermocouples for air experiment 20170110_01.
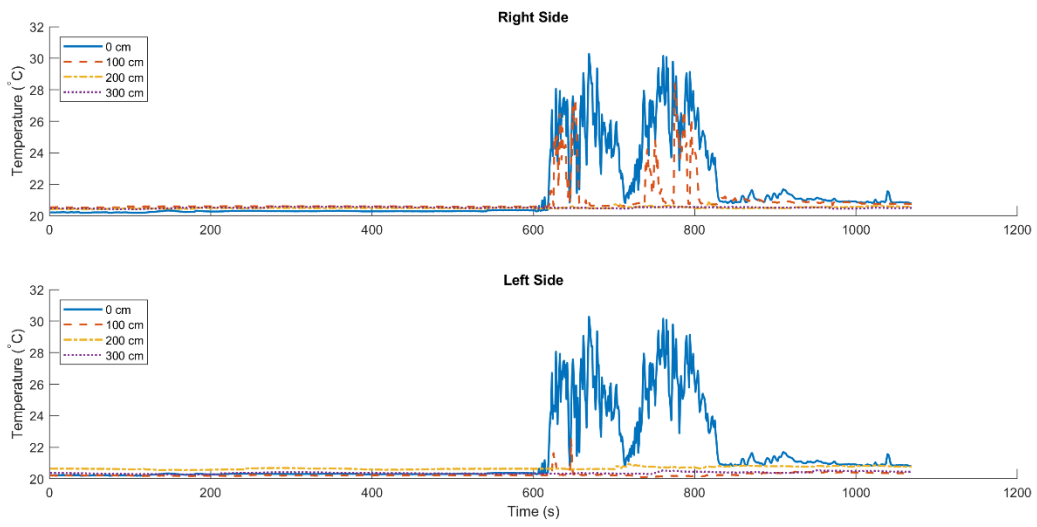
Fig. 49. Temperature data against time recorded by offset thermocouples for air experiment 20170110_01.
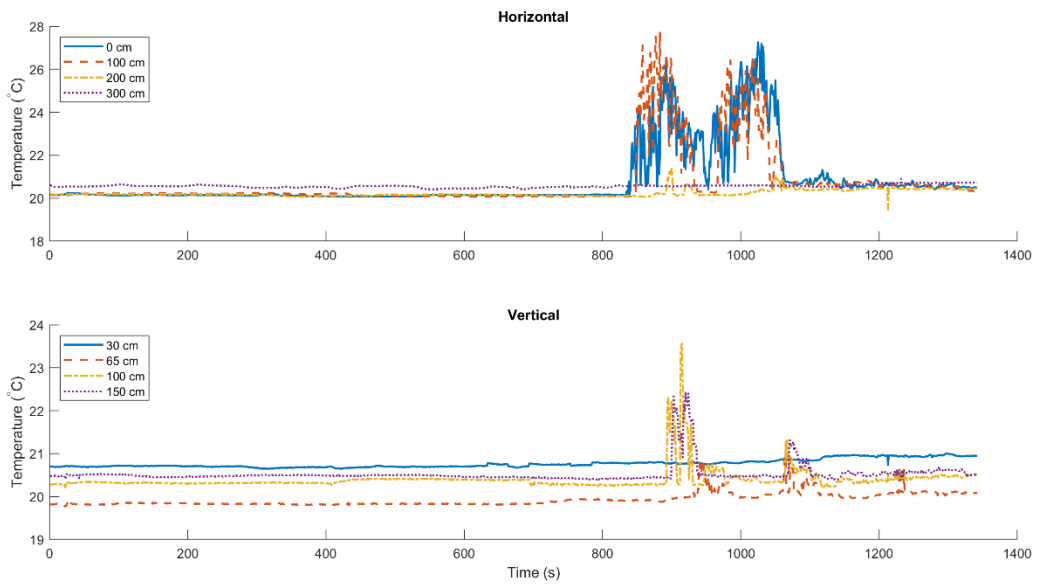
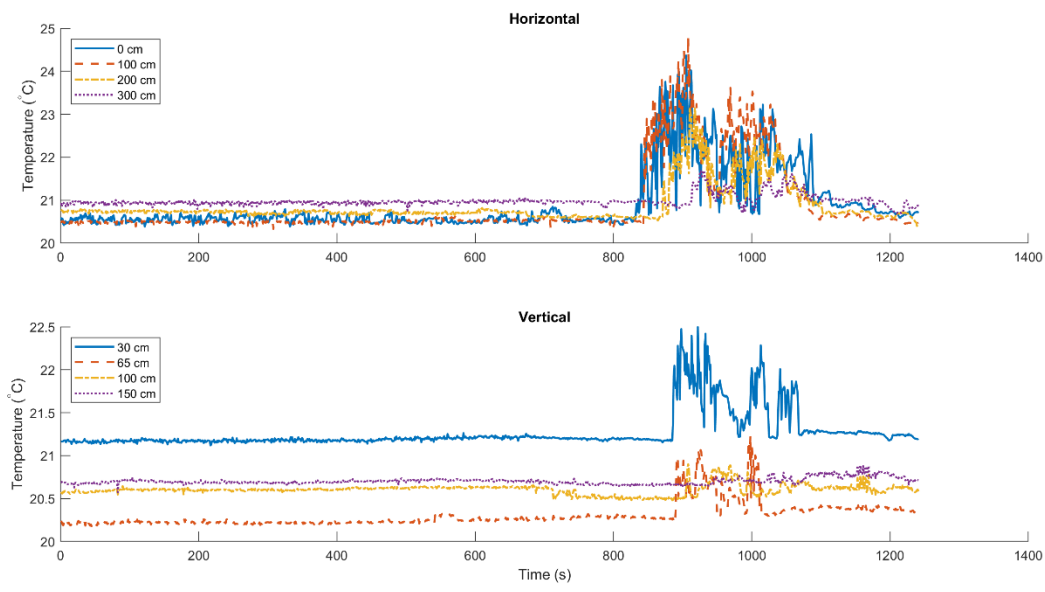**Fig. 50.** Temperature data against time recorded by centerline thermocouples for air experiment 20170110_02.
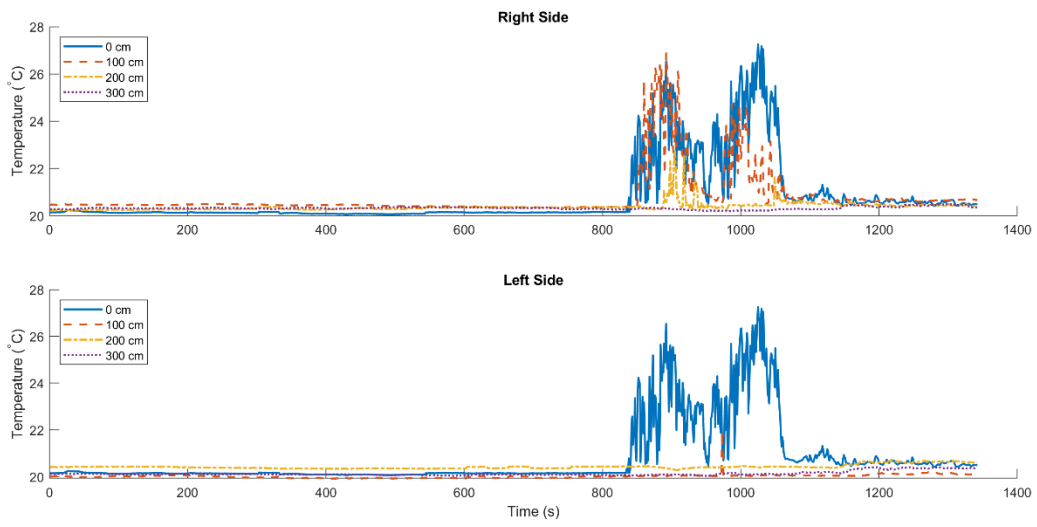
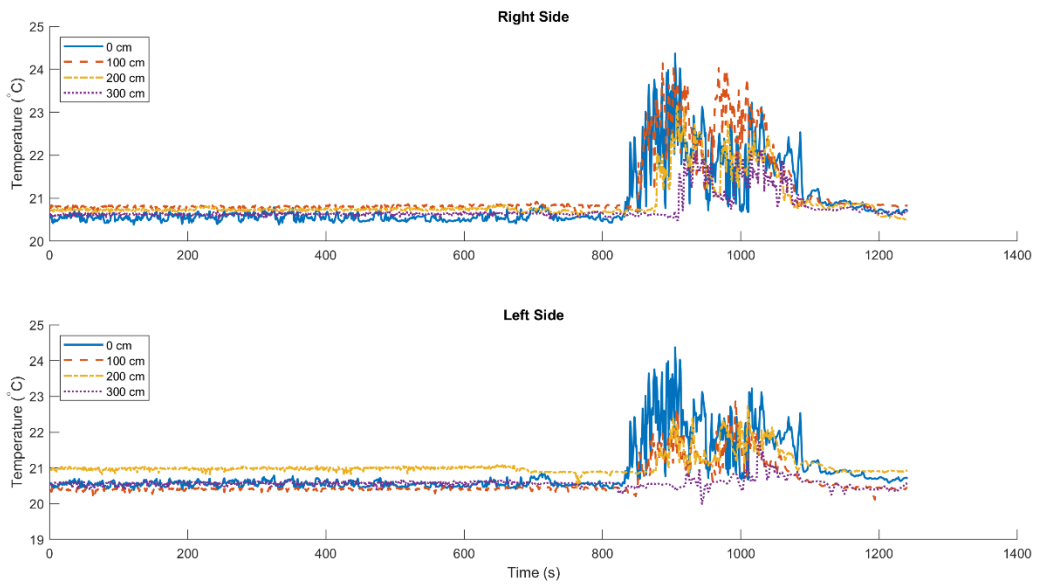**Fig. 51.** Temperature data against time recorded by offset thermocouples for air experiment 20170110_02.
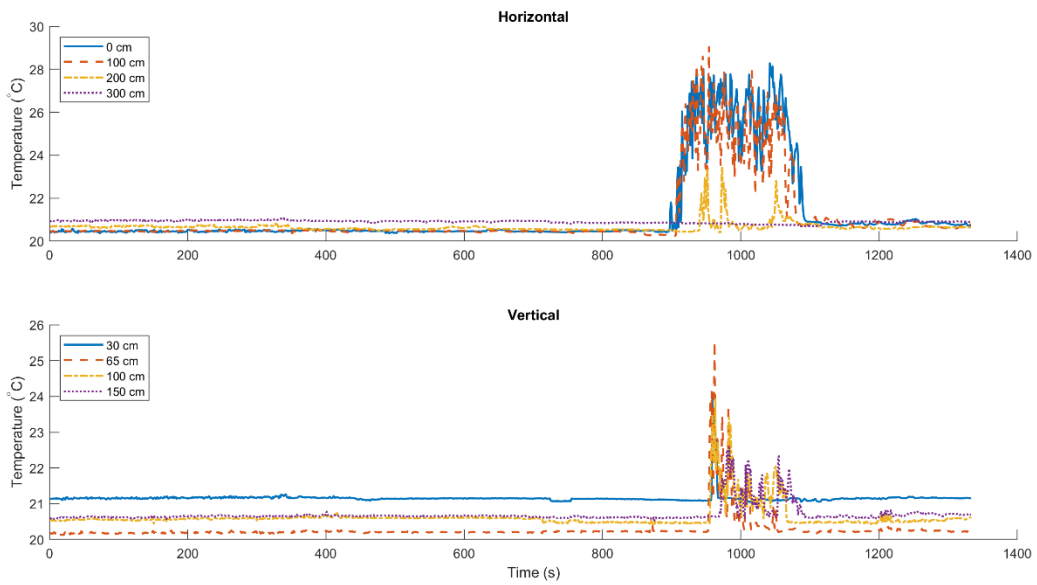
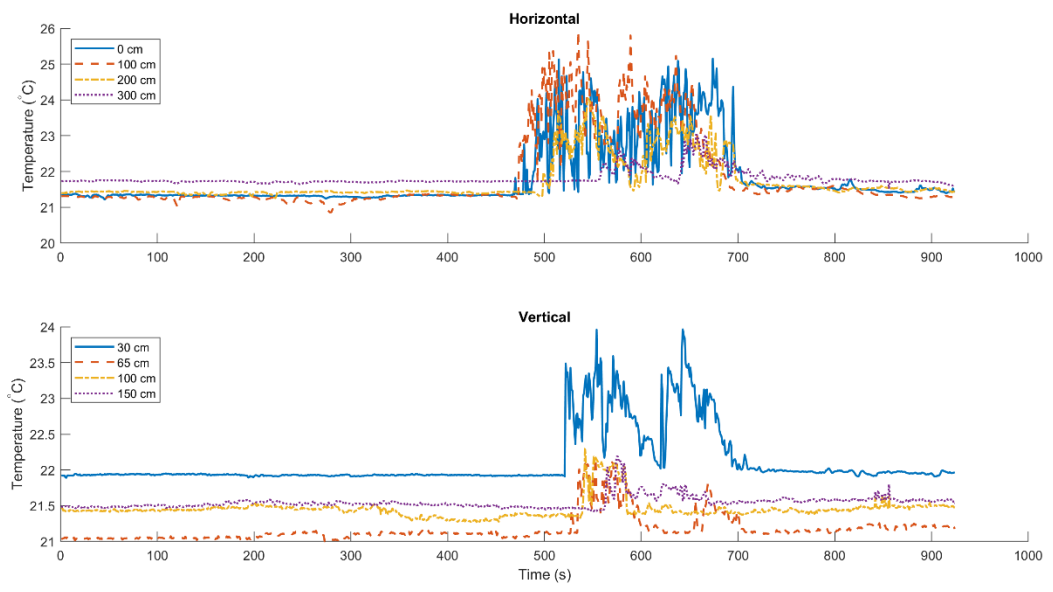**Fig. 52.** Temperature data against time recorded by centerline thermocouples for air experiment 20170110_03.
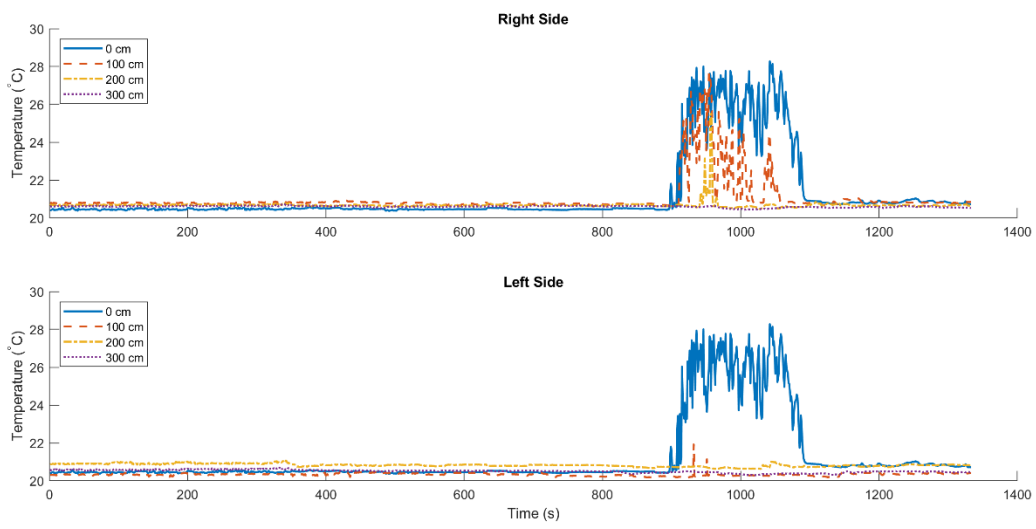
Fig. 53. Temperature data against time recorded by offset thermocouples for air experiment 20170110_03.
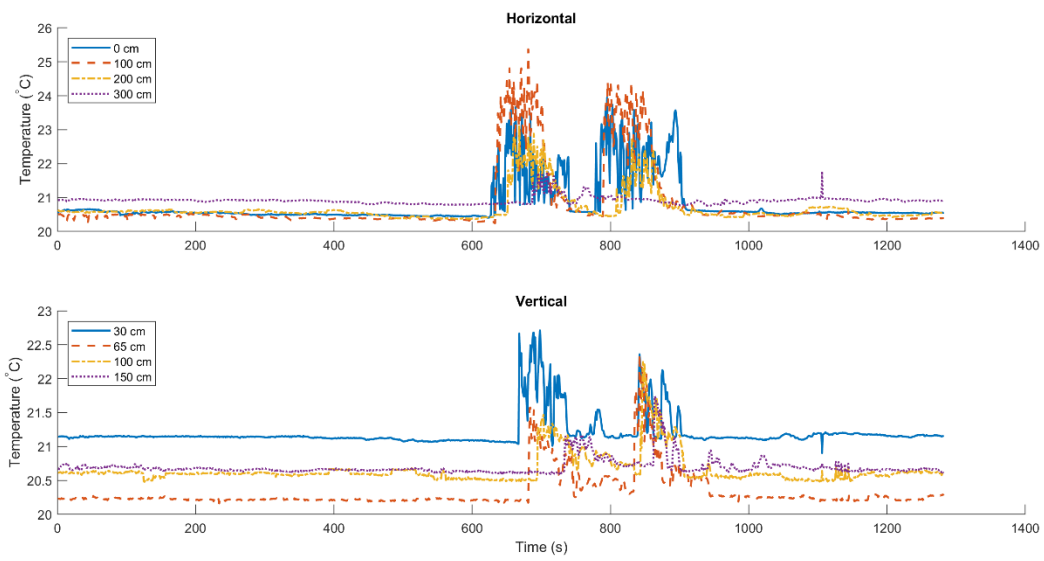
Fig. 54. Temperature data against time recorded by centerline thermocouples for air experiment 20170110_04.

Fig. 55. Temperature data against time recorded by offset thermocouples for air experiment 20170110_04.

Fig. 56. Temperature data against time recorded by centerline thermocouples for air experiment 20170110_05.

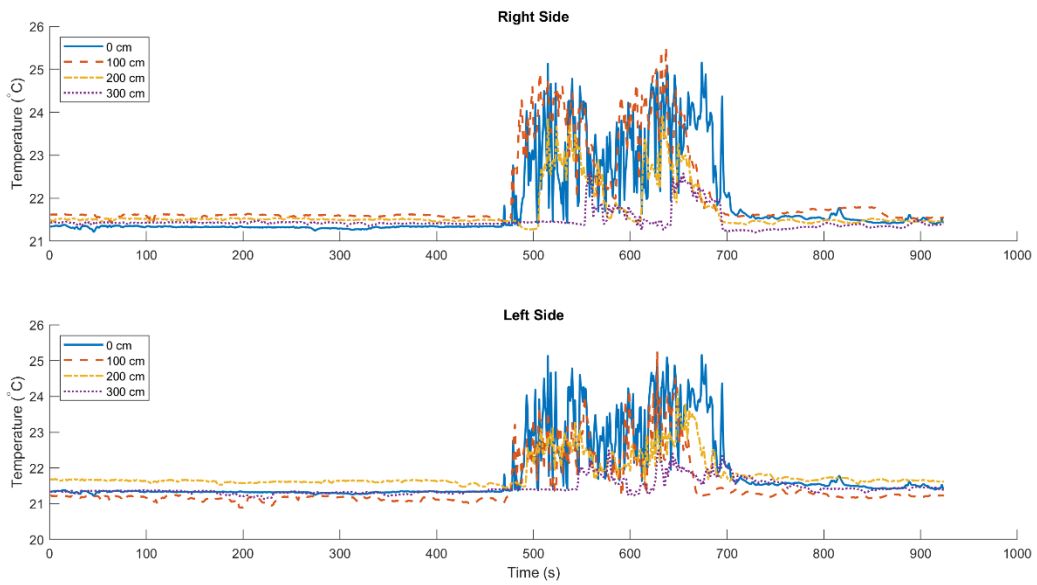**Fig. 57.** Temperature data against time recorded by offset thermocouples for air experiment 20170110_05.

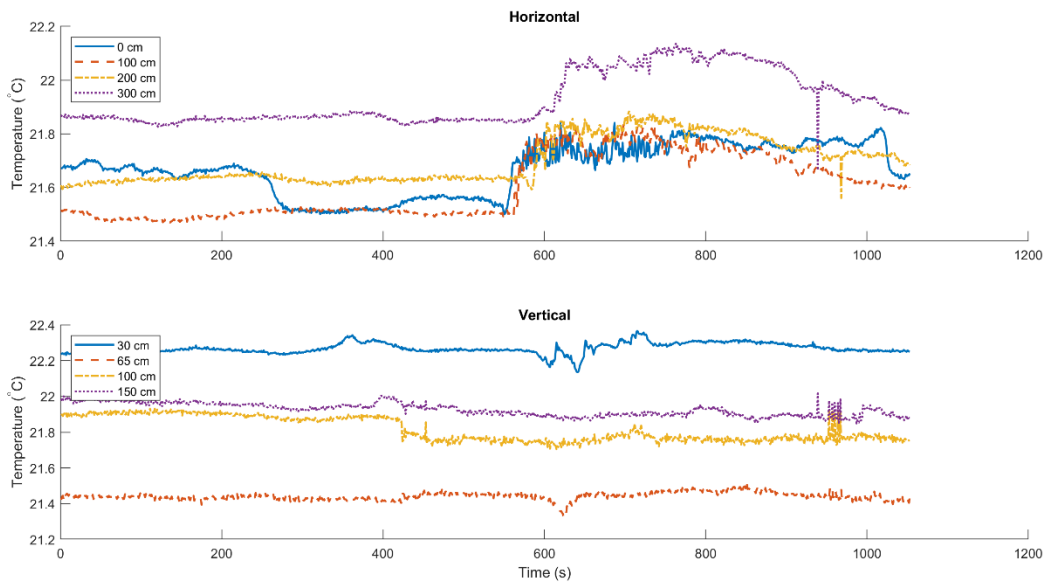**Fig. 58.** Temperature data against time recorded by centerline thermocouples for air experiment 20170110_06.

Fig. 59. Temperature data against time recorded by offset thermocouples for air experiment 20170110_06.

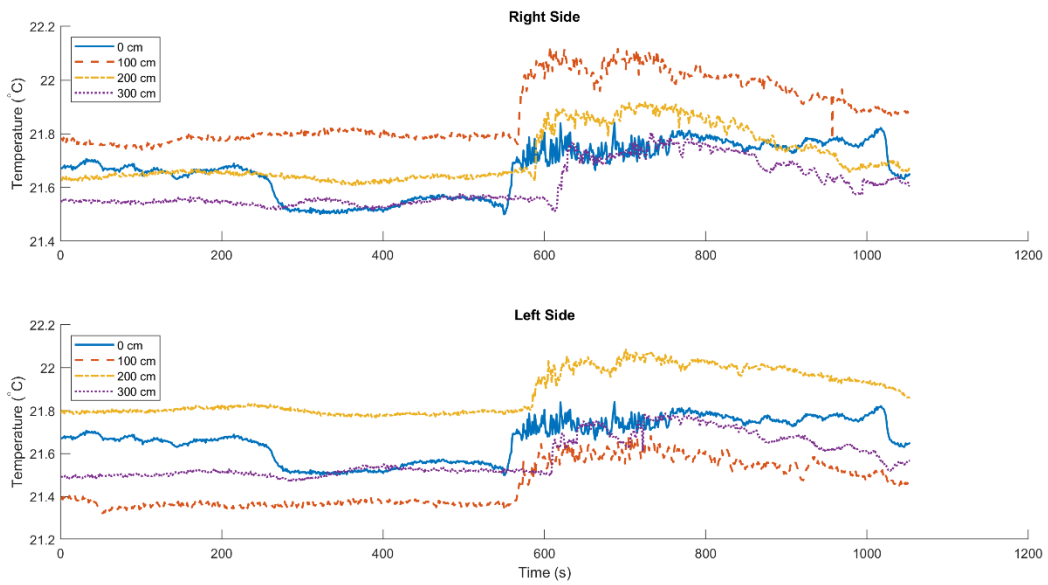**Fig. 60.** Temperature data against time recorded by centerline thermocouples for air experiment 20170112_01.

Fig. 61. Temperature data against time recorded by offset thermocouples for air experiment 20170112_01.

Fig. 62. Temperature data against time recorded by centerline thermocouples for air experiment 20170112_02.

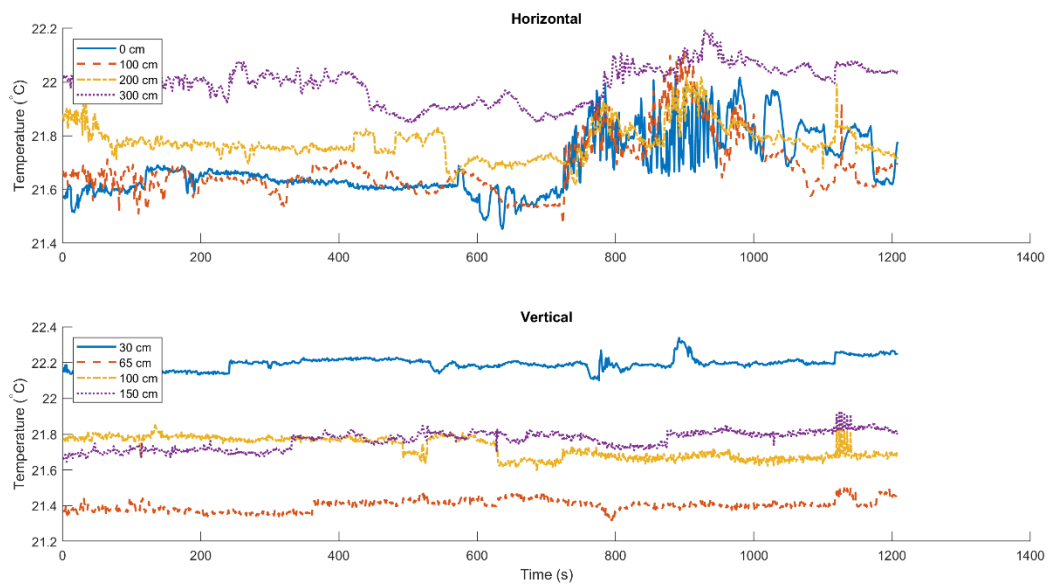**Fig. 63.** Temperature data against time recorded by offset thermocouples for air experiment 20170112_02.

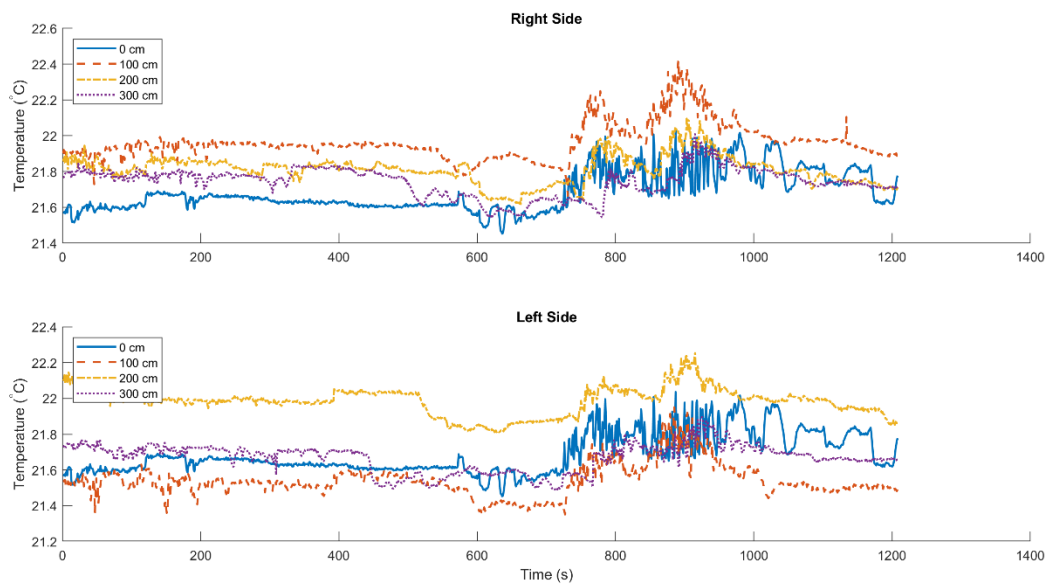**Fig. 64.** Temperature data against time recorded by centerline thermocouples for air experiment 20170112_03.

Fig. 65. Temperature data against time recorded by offset thermocouples for air experiment 20170112_03.

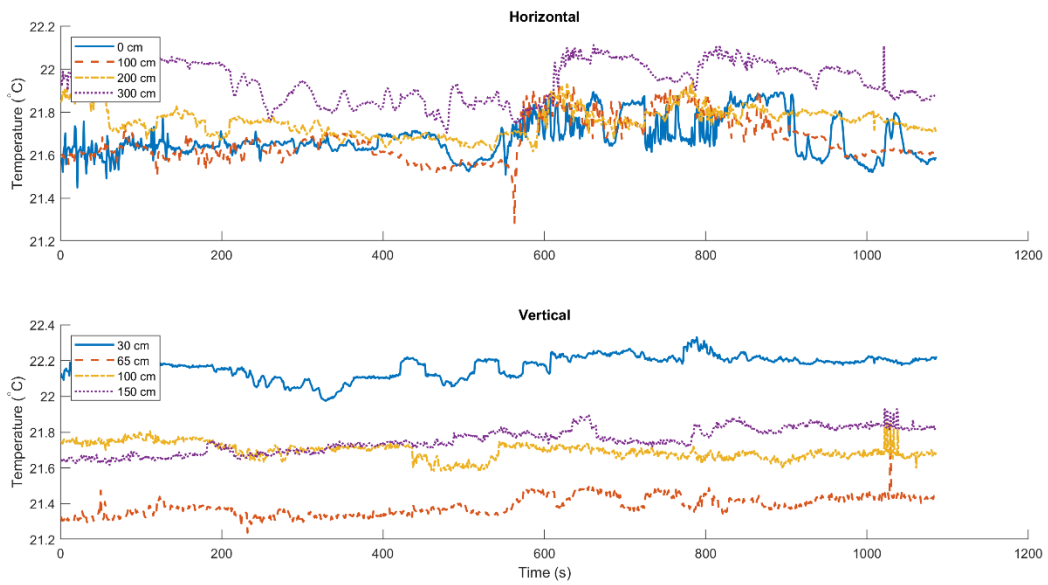**Fig. 66.** Temperature data against time recorded by centerline thermocouples for air experiment 20170112_04.

Fig. 67. Temperature data against time recorded by offset thermocouples for air experiment 20170112_04.

Fig. 68. Temperature data against time recorded by centerline thermocouples for air experiment 20170112_05.

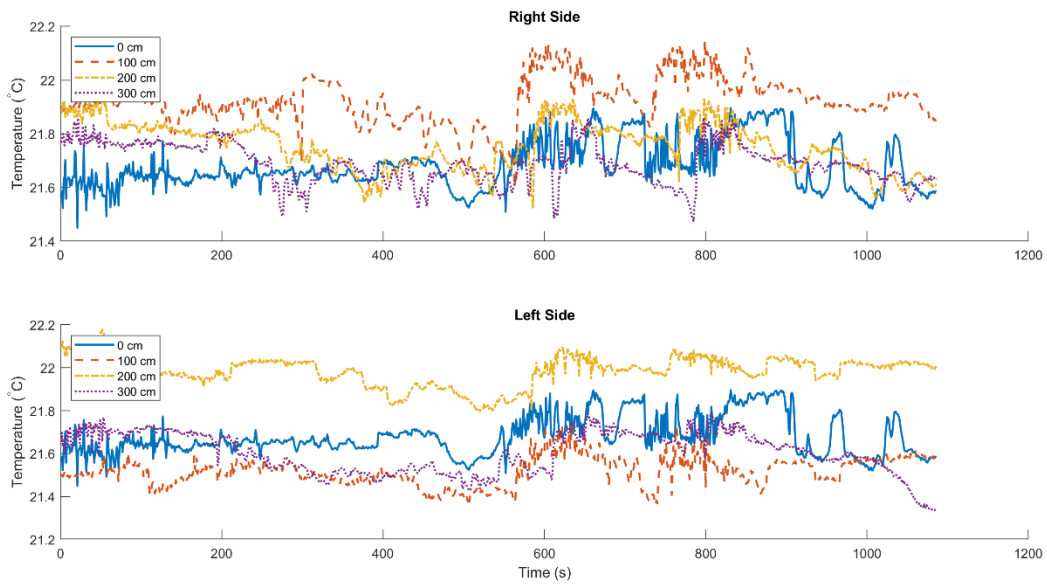**Fig. 69.** Temperature data against time recorded by offset thermocouples for air experiment 20170112_05.

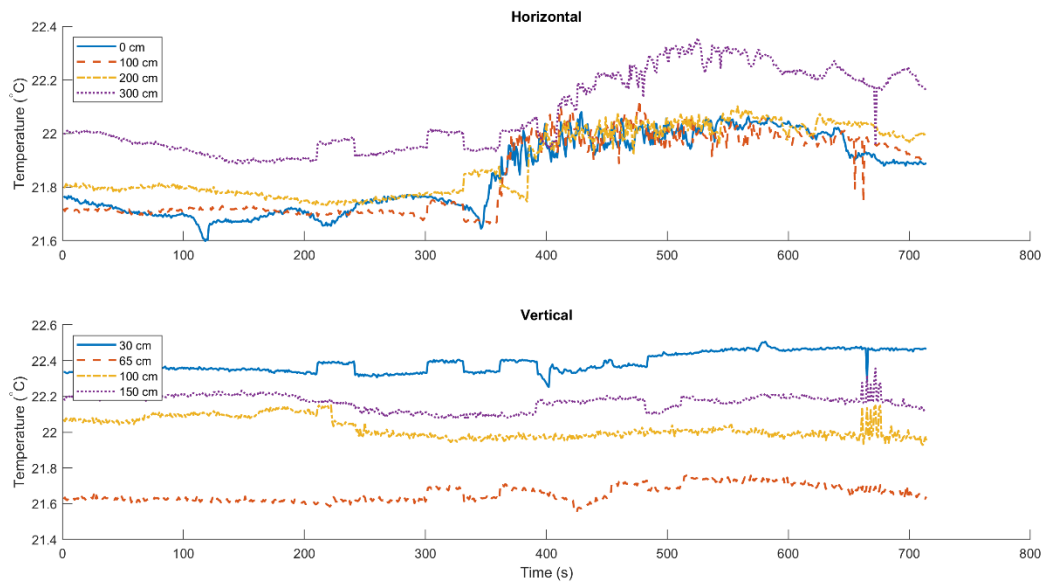**Fig. 70.** Temperature data against time recorded by centerline thermocouples for air experiment 20170113_01.

Fig. 71. Temperature data against time recorded by offset thermocouples for air experiment 20170113_01.
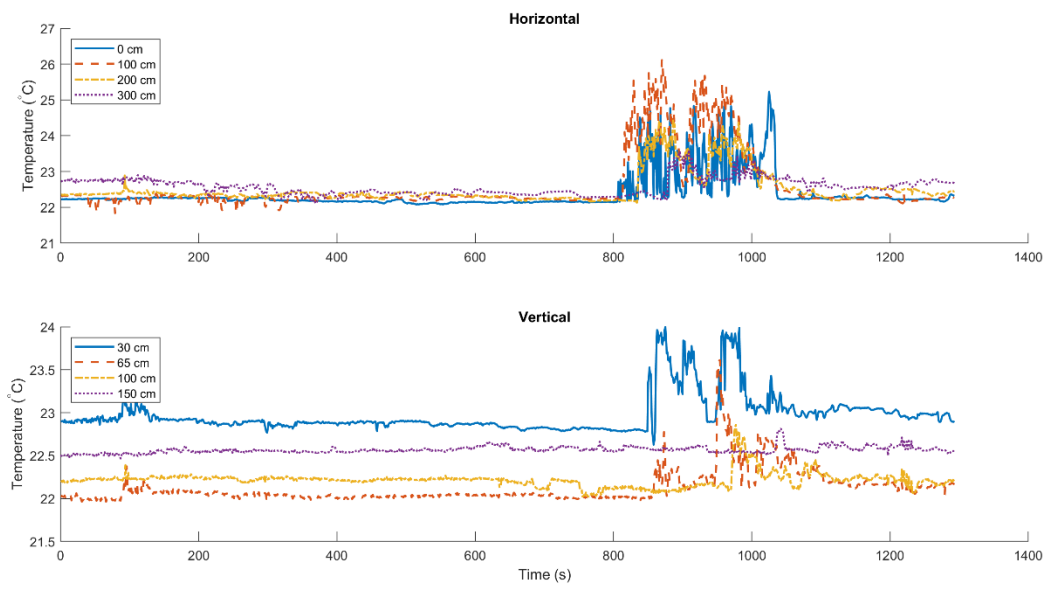
Fig. 72. Temperature data against time recorded by centerline thermocouples for air experiment 20170113_02.
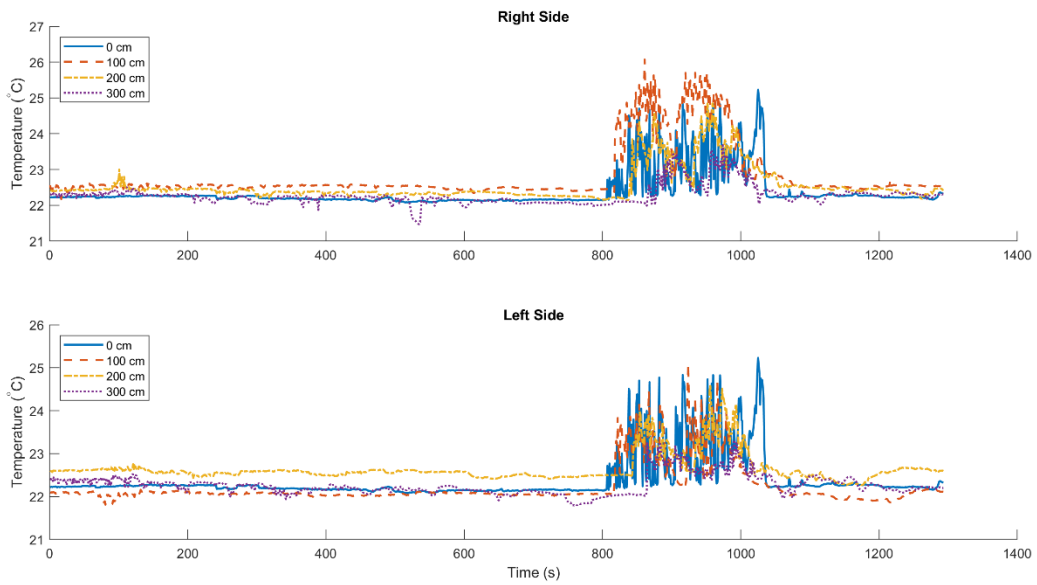
Fig. 73. Temperature data against time recorded by offset thermocouples for air experiment 20170113_02.
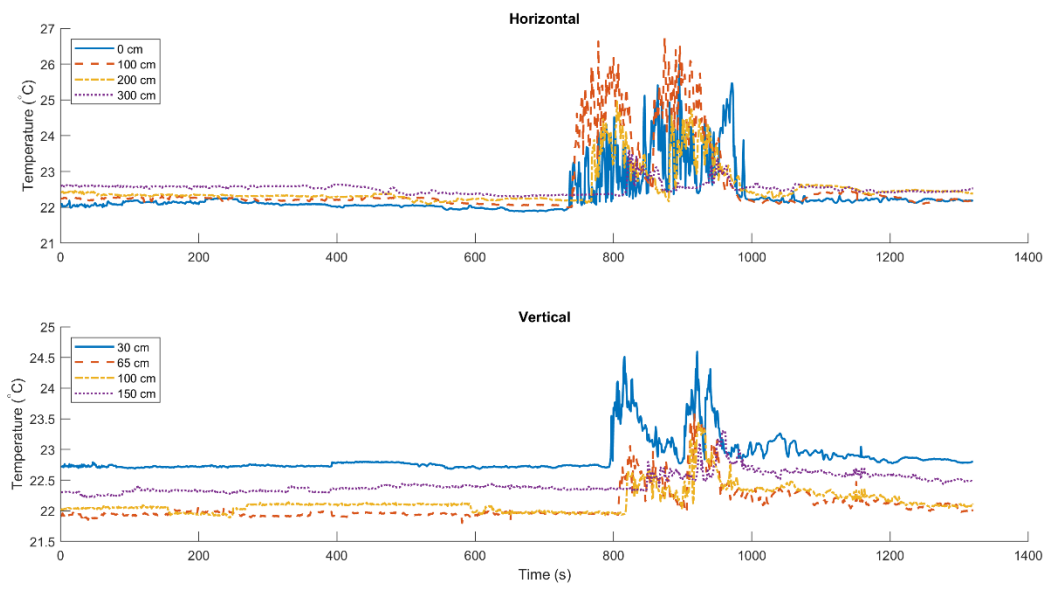
Fig. 74. Temperature data against time recorded by centerline thermocouples for air experiment 20170113_03.

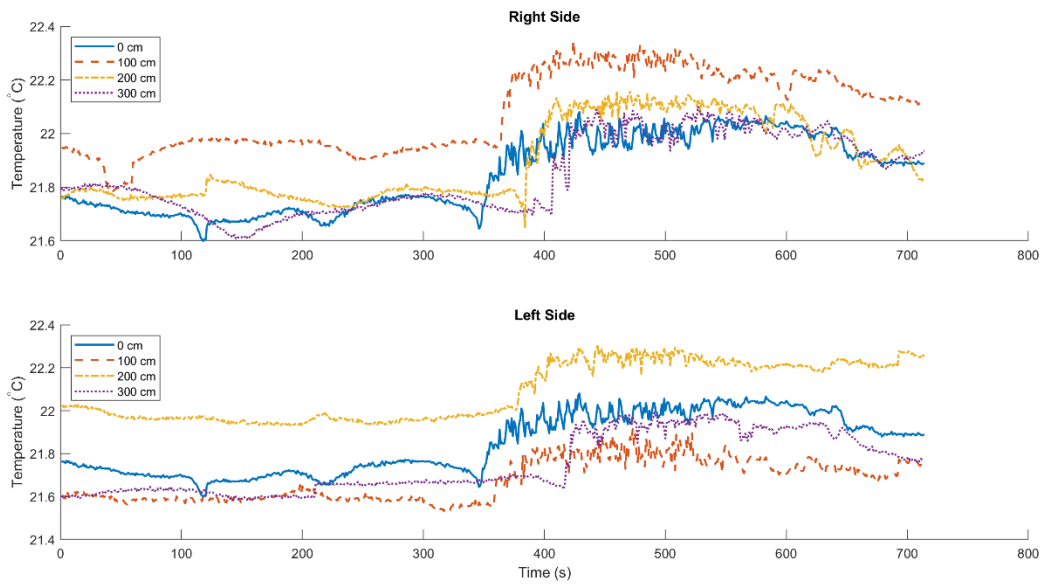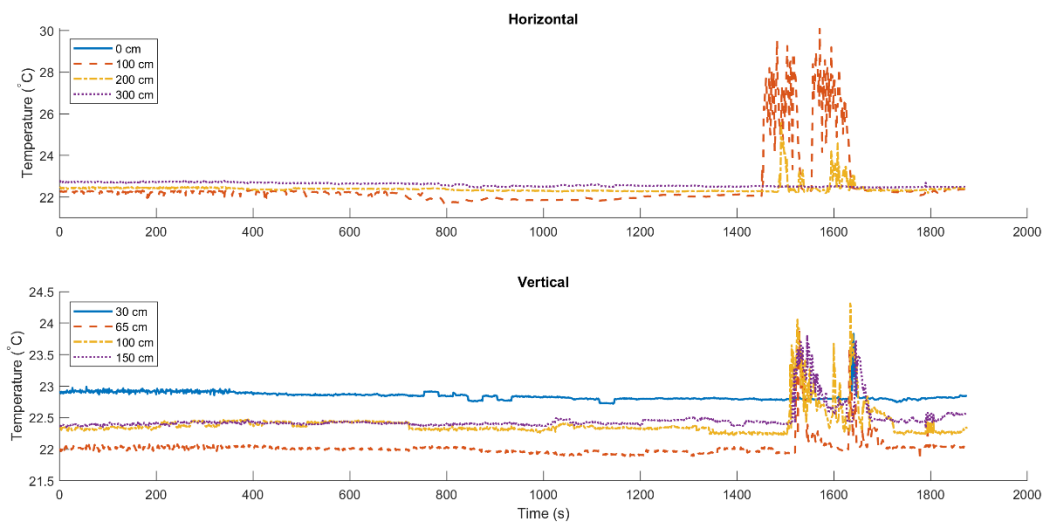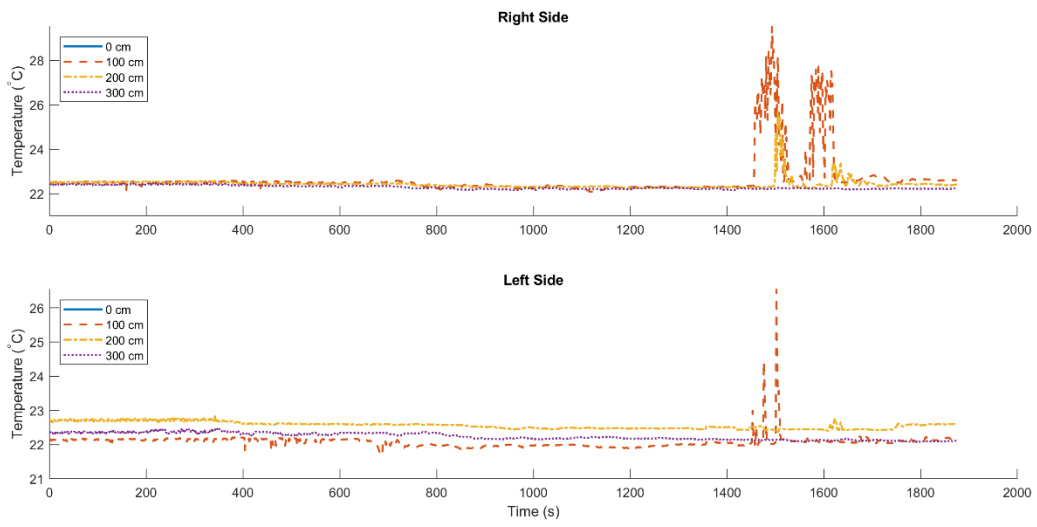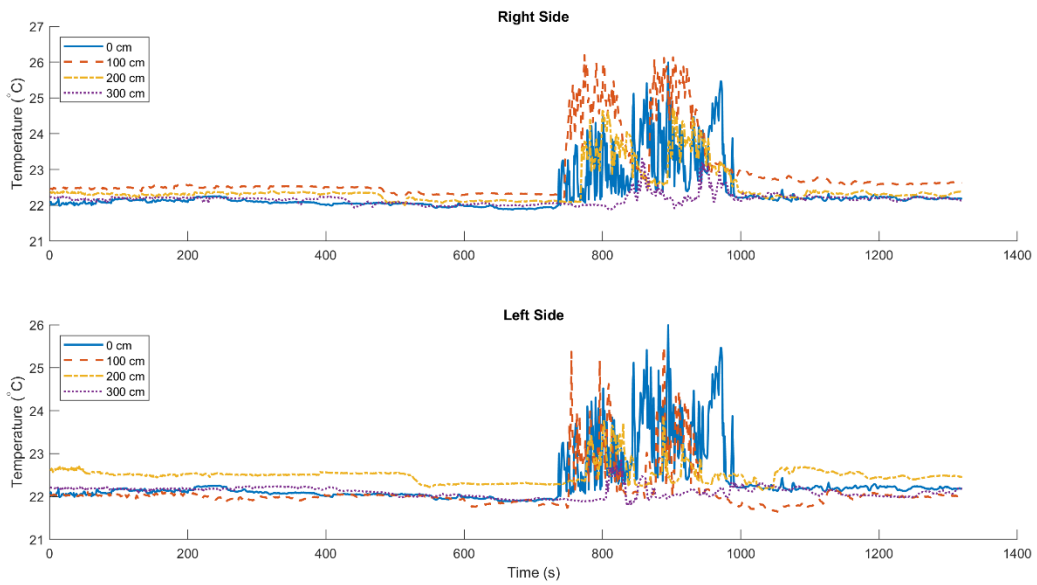**Fig. 75.** Temperature data against time recorded by offset thermocouples for air experiment 20170113_03.

Replication data will be made available via the Texas Data Repository

(https://dataverse.tdl.org/), a platform for publishing and archiving datasets created by faculty,

students, and staff at the University of Texas at Austin, and the Texas Advanced Computing

Center (https://www.tacc.utexas.edu/), a facility of the University of Texas at Austin that designs

and deploys advanced computing technologies

Bibliography

Andrews, B.J., 2014. Dispersal and air entrainment in unconfined dilute pyroclastic density currents. Bull. Volcanol. 76, 1–14. https://doi.org/10.1007/s00445-014-0852-4

Andrews, B.J., Manga, M., 2012. Experimental study of turbulence, sedimentation, and coignimbrite mass partitioning in dilute pyroclastic density currents. J. Volcanol. Geotherm. Res. 225–226, 30–44. https://doi.org/10.1016/j.jvolgeores.2012.02.011

Andrews, B.J., Manga, M., 2011. Effects of topography on pyroclastic density current runout and formation of coignimbrites. Geology 39, 1099–1102. https://doi.org/10.1130/G32226.1

Baxter, P.J., Boyle, R., Cole, P., Neri, A., Spence, R., Zuccaro, G., 2005. The impacts of pyroclastic surges on buildings at the eruption of the Soufrière Hills volcano, Montserrat. Bull. Volcanol. 67, 292–313. https://doi.org/10.1007/s00445-004-0365-7

Baxter, P.J., Jenkins, S., Seswandhana, R., Komorowski, J.C., Dunn, K., Purser, D., Voight, B., Shelley, I., 2017. Human survival in volcanic eruptions: Thermal injuries in pyroclastic surges, their causes, prognosis and emergency management. Burns 43, 1051–1069. https://doi.org/10.1016/j.burns.2017.01.025

Behncke, B., 2009. Hazards from pyroclastic density currents at Mt. Etna (Italy). J. Volcanol. Geotherm. Res. 180, 148–160. https://doi.org/10.1016/j.jvolgeores.2008.09.021

Behncke, B., Neri, M., Carniel, R., 2003. An exceptional case of endogenous lava dome growth spawning pyroclastic avalanches: The 1999 Bocca Nuova eruption of Mt. Etna (Italy). J. Volcanol. Geotherm. Res. 124, 115–128. https://doi.org/10.1016/S0377-0273(03)00072-6

Benage, M.C., Dufek, J., Mothes, P.A., 2016. Quantifying entrainment in pyroclastic density currents from the Tungurahua eruption, Ecuador: Integrating field proxies with numerical simulations. Geophys. Res. Lett. 43, 6932–6941. https://doi.org/10.1002/2016GL069527

Bonnecaze, R., Hallworth, M., Huppert, H., Lister, J., 1995. Axisymmetric particle-driven gravity currents. J. Fluid Mech. 294, 93–121.

Bonnecaze, R., Huppert, H., Lister, J., 1993. Particle-driven gravity currents. J. Fluid Mech. 250, 339–369.

Bourdier, J.L., Abdurachman, E., 2001. Decoupling of small-volume pyroclastic flows and related hazards at Merapi volcano, Indonesia. Bull. Volcanol. 63, 309–325. https://doi.org/10.1007/s004450100133

Branney, M.J., Kokelaar, P., 2002. Pyroclastic density currents and the sedimentation of ignimbrites, Geological Society Memoir No. 27. https://doi.org/10.1086/427850

Breard, E.C.P., Lube, G., 2017. Inside pyroclastic density currents – uncovering the enigmatic flow structure and transport behaviour in large-scale experiments. Earth Planet. Sci. Lett. 458, 22–36. https://doi.org/10.1016/j.epsl.2016.10.016

Breard, E.C.P., Lube, G., Jones, J.R., Dufek, J., Cronin, S.J., Valentine, G.A., Moebis, A., 2016. Coupling of turbulent and non-turbulent flow regimes within pyroclastic density currents.

Nat. Geosci. 9, 767–771. https://doi.org/10.1038/ngeo2794

Burgisser, A., Bergantz, G.W., 2002. Reconciling pyroclastic flow and surge: The multiphase physics of pyroclastic density currents. Earth Planet. Sci. Lett. 202, 405–418. https://doi.org/10.1016/S0012-821X(02)00789-6

Bursik, M.I., Woods, A.W., 1996. The dynamics and thermodynamics of large ash flows. Bull. Volcanol. 58, 175–193. https://doi.org/10.1007/s004450050134

Calder, E.S., Sparks, R.S.J., Woods, A.W., 1997. Dynamics of co-ignimbrite plumes generated from pyroclastic flows of Mount St. Helens (7 August 1980). Bull. Volcanol. 58, 432–440. https://doi.org/10.1007/s004450050151

Capra, L., Sulpizio, R., Márquez-Ramirez, V.H., Coviello, V., Doronzo, D.M., Arambula-Mendoza, R., Cruz, S., 2018. The anatomy of a pyroclastic density current: the 10 July 2015 event at Volcán de Colima (Mexico). Bull. Volcanol. 80. https://doi.org/10.1007/s00445-018-1206-4

Choux, C., Druitt, T., Thomas, N., 2004. Stratification and particle segregation in flowing polydisperse suspensions, with applications to the transport and sedimentation of pyroclastic density currents. J. Volcanol. Geotherm. Res. 138, 223–241. https://doi.org/10.1016/j.jvolgeores.2004.07.004

Choux, C.M., Druitt, T.H., 2002. Analogue study of particle segregation in pyroclastic density currents, with implications for the emplacement mechanisms of large ignimbrites. Sedimentology 49, 907–928. https://doi.org/10.1046/j.1365-3091.2002.00481.x

Dellino, P., Büttner, R., Dioguardi, F., Doronzo, D.M., La Volpe, L., Mele, D., Sonder, I., Sulpizio, R., Zimanowski, B., 2010. Experimental evidence links volcanic particle characteristics to pyroclastic flow hazard. Earth Planet. Sci. Lett. 295, 314–320. https://doi.org/10.1016/j.epsl.2010.04.022

Dellino, P., Dioguardi, F., Mele, D., D'Addabbo, M., Zimanowski, B., Büttner, R., Doronzo, D.M., Sonder, I., Sulpizio, R., Dürig, T., La Volpe, L., 2014. Volcanic jets, plumes, and collapsing fountains: Evidence from large-scale experiments, with particular emphasis on the entrainment rate. Bull. Volcanol. 76, 1–18. https://doi.org/10.1007/s00445-014-0834-6

Dellino, P., Dioguardi, F., Zimanowski, B., Büttner, R., Mele, D., La Volpe, L., Sulpizio, R., Doronzo, D.M., Sonder, I., Bonasia, R., Calvari, S., Marotta, E., 2010. Conduit flow experiments help constraining the regime of explosive eruptions. J. Geophys. Res. Solid Earth 115, 1–17. https://doi.org/10.1016/S0377-0273(02)00471-7

Denlinger, R.P., 1987. A model for generation of ash clouds by pyroclastic flows, with application to the 1980 eruptions at Mount St. Helens, Washington. J. Geophys. Res. 92, 10284. https://doi.org/10.1029/JB092iB10p10284

Druitt, T.H., 1998. Pyroclastic density currents. Geol. Soc. London, Spec. Publ. 145, 145–182. https://doi.org/10.1144/GSL.SP.1996.145.01.08

Dufek, J., 2016. The Fluid Mechanics of Pyroclastic Density Currents. Annu. Rev. Fluid Mech. 48, 459–485. https://doi.org/10.1146/annurev-fluid-122414-034252

Dufek, J., Bergantz, G.W., 2007. Dynamics and deposits generated by the Kos Plateau Tuff eruption: Controls of basal particle loss on pyroclastic flow transport. Geochemistry, Geophys. Geosystems 8. https://doi.org/10.1029/2007GC001741

Ellison, T.H., Turner, J.S., 1959. Turbulent entrainment in stratified flows. J. Fluid Mech. 6, 423–448. https://doi.org/10.1017/S0022112059000738

Fisher, R.., 1979. Models for pyroclastic surges nd pyroclastic flows. Plateau 6, 305–318. https://doi.org/10.1016/0377-0273(79)90008-8

Geyer, W.R., Smith, J.D., 1987. Shear instability in a highly stratified estuary. J. Phys. Oceanogr. https://doi.org/10.1175/1520-0485(1987)017<1668:SIIAHS>2.0.CO;2

Gorshkov, G.S., 1959. Gigantic eruption of the volcano bezymianny. Bull. Volcanol. 20, 77–109. https://doi.org/10.1007/BF02596572

Gorshkov, G.S., Dubik, Y.M., 1970. Gigantic directed blast at Shiveluch volcano (Kamchatka). Bull. Volcanol. 34, 261–288. https://doi.org/10.1007/BF02597790

Hákonardóttir, K.M., Hogg, A.J., Batey, J., Woods, A.W., 2003. Flying avalanches. Geophys. Res. Lett. 30, n/a-n/a. https://doi.org/10.1029/2003GL018172

Hall, M.L., Steele, A.L., Mothes, P.A., Ruiz, M.C., 2013. Pyroclastic density currents (PDC) of the 16-17 august 2006 eruptions of tungurahua volcano, ecuador: Geophysical registry and characteristics. J. Volcanol. Geotherm. Res. 265, 78–93. https://doi.org/10.1016/j.jvolgeores.2013.08.011

Hallworth, M.A., Phillips, J.C., Huppert, H.E., Sparks, R.S.J., 1993. Entrainment in turbulent gravity currents. Nature 362, 829–831.

Hazen, A., 1904. On Sedimentation. Trans. Am. Soc. Civ. Eng. 8, 45–71.

Hoblitt, R.P., 2000. Was the 18 May 1980 lateral blast at Mt St Helens the product of two explosions? Philos. Trans. R. Soc. London Ser. a-Mathematical Phys. Eng. Sci. 358, 1639–1661. https://doi.org/10.1098/rsta.2000.0608

Hogg, A.J., Huppert, H.E., Hallworth, M.A., 1999. Reversing buoyancy of particle-driven gravity currents. Phys. Fluids 11, 2891–2900. https://doi.org/10.1063/1.870147

Hogg, A.J., Ungarish, M., Huppert, H.E., 2000. Particle-driven gravity currents: Asymptotic and box model solutions. Eur. J. Mech. B/Fluids 19, 139–165. https://doi.org/10.1016/S0997-7546(00)00102-3

Huppert, H.E., Turner, J.S., Carey, S.N., Sparks, R.S.J., Hallworth, M.A., 1986. A laboratory simulation of pyroclastic flows down slopes. J. Volcanol. Geotherm. Res. 30, 179–199.

Iguchi, M., Ishihara, K., Surono, Hendrasto, M., 2011. Learn from 2010 Eruptions at Merapi and Sinabung Volcanoes in Indonesia. Annu. Disas. Prev. Res. Inst., Kyoto Univ 185–194.

Jenkins, S., Komorowski, J.C., Baxter, P.J., Spence, R., Picquout, A., Lavigne, F., Surono, 2013. The Merapi 2010 eruption: An interdisciplinary impact assessment methodology for studying pyroclastic density current dynamics. J. Volcanol. Geotherm. Res. 261, 316–329. https://doi.org/10.1016/j.jvolgeores.2013.02.012

Kelfoun, K., Legros, F., Gourgaud, A., 2000. A statistical study of trees damaged by the 22 November 1994 eruption of Merapi volcano (Java, Indonesia): Relationships between ash-cloud surges and block-and-ash flows. J. Volcanol. Geotherm. Res. 100, 379–393. https://doi.org/10.1016/S0377-0273(00)00147-5

Kleiser, L., Zang, T.A., 1991. Numerical simulation of transition in wall-bounded shear flows. Annu. Rev. Fluid Mech. 23, 495–537.

Komorowski, J.C., Jenkins, S., Baxter, P.J., Picquout, A., Lavigne, F., Charbonnier, S., Gertisser, R., Preece, K., Cholik, N., Budi-Santoso, A., Surono, 2013. Paroxysmal dome explosion during the Merapi 2010 eruption: Processes and facies relationships of associated high-energy pyroclastic density currents. J. Volcanol. Geotherm. Res. 261, 260–294. https://doi.org/10.1016/j.jvolgeores.2013.01.007

Lipman, P.W., Mullineaux, D.R., 1980. The 1980 eruptions of Mount St. Helens, Washington. Washington, DC, USA.

Loughlin, S.C., Baxter, P.J., Aspinall, W.P., Darroux, B., Harford, C.L., Miller, a D., 2002. Eyewitness accounts of the 25 June 1997 pyroclastic flows and surges at Soufriere Hills Volcano, Montserrat, and implications for disaster mitigation. Geol. Soc. London, Mem. 21, 211–230. https://doi.org/10.1144/GSL.MEM.2002.021.01.10

Loughlin, S.C., Calder, E.S., Clarke, A., Cole, P.D., Luckett, R., Mangan, M.T., Pyle, D.M., Sparks, R.S.J., Voight, B., Watts, R.B., 2002. Pyroclastic flows and surges generated by the 25 June 1997 dome collapse, Soufriere Hills Volcano, Montserrat. Geol. Soc. London, Mem. 21, 191–209. https://doi.org/10.1144/GSL.MEM.2002.021.01.09

Macias, J.L., Espindola, J.M., Bursik, M., Sheridan, M.F., 1998. Development Of Lithic-Breccias In the 1982 Pyroclastic Flow Deposits Of El Chichon Volcano, Mexico. J. Volcanol. Geotherm. Res. 83, 173–196.

Nairn, I.A., Self, S., 1978. Explosive eruptions and pyroclastic avalanches from Nguaruhoe in February 1975. J. Volcanol. Geotherm. Res. 3, 39–60.

Nield, S.E., Woods, A.W., 2004. Effects of flow density on the dynamics of dilute pyroclastic density currents. J. Volcanol. Geotherm. Res. 132, 269–281. https://doi.org/10.1016/S0377-0273(03)00314-7

Parker, G., Fukushima, Y., Pantin, H.M., 1986. Self-accelerating turbidity currents. J. Fluid Mech. 171, 145. https://doi.org/10.1017/S0022112086001404

Parker, G., Garcia, M., Fukushima, Y., Yu, W., 1987. Experiments on turbidity currents over an erodible bed. J. Hydraul. Res. 25, 123–147. https://doi.org/10.1080/00221688709499292

Rouse, H., 1937. Modern conceptions of fluid turbulence. Trans. Am. Soc. Civ. Eng. 102, 463–505.

Saucedo, R., Macías, J.L., Bursik, M., 2004. Pyroclastic flow deposits of the 1991 eruption of Volcán de Colima, Mexico. Bull. Volcanol. 66, 291–306. https://doi.org/10.1007/s00445-003-0311-0

Saucedo, R., Macías, J.L., Bursik, M.I., Mora, J.C., Gavilanes, J.C., Cortes, A., 2002.

Emplacement of pyroclastic flows during the 1998-1999 eruption of Volcán de Colima, México. J. Volcanol. Geotherm. Res. 117, 129–153. https://doi.org/10.1016/S0377-0273(02)00241-X

Sher, D., Woods, A.W., 2017. Mixing in continuous gravity currents. J. Fluid Mech. 818, R41–R415. https://doi.org/10.1017/jfm.2017.168

Smith, R., 2015. Hydraulic Flow, in: North, G.R., Pyle, J., Zhang, F. (Eds.), Encyclopedia of Atmospheric Sciences. Elsevier, Amsterdam, Netherlands, pp. 332–333. https://doi.org/10.1038/098087a0

Sparks, R.S.J., 1986. The dimensions and dynamics of volcanic eruption columns. Bull. Volcanol. 48, 3–15. https://doi.org/10.1007/BF01073509

Sparks, R.S.J., 1978. Gas release rates from pyroclastic flows: a assessment of the role of fluidisation in their emplacement. Bull. Volcanol. 41, 1–9. https://doi.org/10.1007/BF02597679

Sparks, R.S.J., 1976. Grain size variations in ignimbrites and implications for the transport of pyroclastic flows. Sedimentology 23, 147–188. https://doi.org/10.1111/j.1365-3091.1976.tb00045.x

Sparks, R.S.J., Bonnecaze, R.T., Huppert, H.E., Lister, J.R., Hallworth, M.A., Mader, H., Phillips, J., 1993. Sediment-laden gravity currents with reversing buoyancy. Earth Planet. Sci. Lett. 114, 243–257. https://doi.org/10.1016/0012-821X(93)90028-8

Sparks, R.S.J., Bursik, M.I., Carey, S.N., Gilbert, J.S., Glaze, L.S., Sigurdsson, H., Woods, A.W., 1997. Volcanic Plumes. John Wiley & Sons Ltd., West Sussex, UK.

Sparks, R.S.J., Moore, J.G., Rice, C.J., 1986. The initial giant umbrella cloud of the May 18th, 1980 explosive eruption of Mount St. Helens. J. vol 28, 257–274.

Sparks, R.S.J., Walker, G.P.L., 1977. The significance of vitric-enriched air-fall ashes associated with crystal-enriched ignimbrites. J. Volcanol. Geotherm. Res. 2, 329–341.

Sulpizio, R., Dellino, P., Doronzo, D.M., Sarocchi, D., 2014. Pyroclastic density currents: State of the art and perspectives. J. Volcanol. Geotherm. Res. 283, 36–65. https://doi.org/10.1016/j.jvolgeores.2014.06.014

Sulpizio, R., Mele, D., Dellino, P., La Volpe, L., 2007. Deposits and physical properties of pyroclastic density currents during complex Subplinian eruptions: The AD 472 (Pollena) eruption of Somma-Vesuvius, Italy. Sedimentology 54, 607–635. https://doi.org/10.1111/j.1365-3091.2006.00852.x

Turner, J.S., 1986. Turbulent entrainment: the development of the entrainment assumption, and its application to geophysical flows. J. Fluid Mech. 173, 431–471.

Valentine, G.A., 1987. Stratified flow in pyroclastic surges. Bull. Volcanol. 49, 616–630. https://doi.org/10.1007/BF01079967

Walker, G.P.L., 1980. The Taupo Pumice: Product of the most powerful known (ultraplinian) eruption? J. Volcanol. Geotherm. Res. 8, 69–94.

Wilson, C.J.N., 1984. The role of fluidization in the emplacement of pyroclastic flows, 2: Experimental results and their interpretation. J. Volcanol. Geotherm. Res. 20, 55–84.

Wilson, C.J.N., Houghton, B.F., Kampt, P.J.J., Mc Williamst, M.O., 1995. An exceptionally widespread ignimbrite with implications for pyroclastic flow emplacement. Nature 378, 605–607. https://doi.org/10.1038/378605a0

Woods, A.W., 2010. Turbulent Plumes in Nature. Annu. Rev. Fluid Mech. 42, 391–412. https://doi.org/10.1146/annurev-fluid-121108-145430

Woods, A.W., Bursik, M.I., 1994. A laboratory study of ash flows. J. Geophys. Res. 99, 4375–4394. https://doi.org/10.1029/93JB02224

Woods, A.W., Bursik, M.I., Kurbatov, A. V., 1998. The interaction of ash flows with ridges. Bull. Volcanol. 60, 38–51. https://doi.org/10.1007/s004450050215

Woods, A.W., Caulfield, C.P., 1992. A Laboratory Sudy of Explosive Volcanic Eruptions. J. Geophys. Res. 97, 6699–6712.

Woods, A.W., Kienle, J., 1994. The dynamics and thermodynamics of volcanic clouds: Theory and observations from the april 15 and april 21, 1990 eruptions of redoubt volcano, Alaska. J. Volcanol. Geotherm. Res. 62, 273–299. https://doi.org/10.1016/0377-0273(94)90037-X

Woods, A.W., Wohletz, K., 1991. Dimensions and dynamics of co-ignimbrite eruption columns. Nature 350, 225–227. https://doi.org/10.1038/350225a0

Zagarola, M. V., Smith, A.J., 1998. Mean Flow Scaling of Turbulent Pipe Flow. J. Fluid Mech. 373, 33–79.

Zobin, V.M., 2018. Development of the 10–11 July 2015 two-stage sequence of multiple emplacements of pyroclastic density currents at Volcán de Colima, México: Insight from associated seismic signals. J. Volcanol. Geotherm. Res. 351, 29–40. https://doi.org/10.1016/j.jvolgeores.2017.12.012

Vita

Sean Bryan O'Donnell was born in Westerville, OH. After graduating from Westerville Central High School in May 2012, he entered Cedarville University in Cedarville, OH, and received his Bachelor of Science in Geology in May 2016. In August 2016, he entered the Jackson School of Geosciences at the University of Texas at Austin, and is currently a Teaching Assistant and Master of Science candidate. His professional interests include physical volcanology, igneous petrology, and experimental fluid mechanics.

Address: s.b.odonnell@att.net

This thesis was typed by the author.